Design and Control Modeling of Novel Electro-magnets Driven Spherical Motion Generators

Li, Xuerong

Publication date:
2019

Document Version
Publisher's PDF, also known as Version of record

Citation for published version (APA):
Li, X. (2019). *Design and Control Modeling of Novel Electro-magnets Driven Spherical Motion Generators*. Aalborg Universitetsforlag.

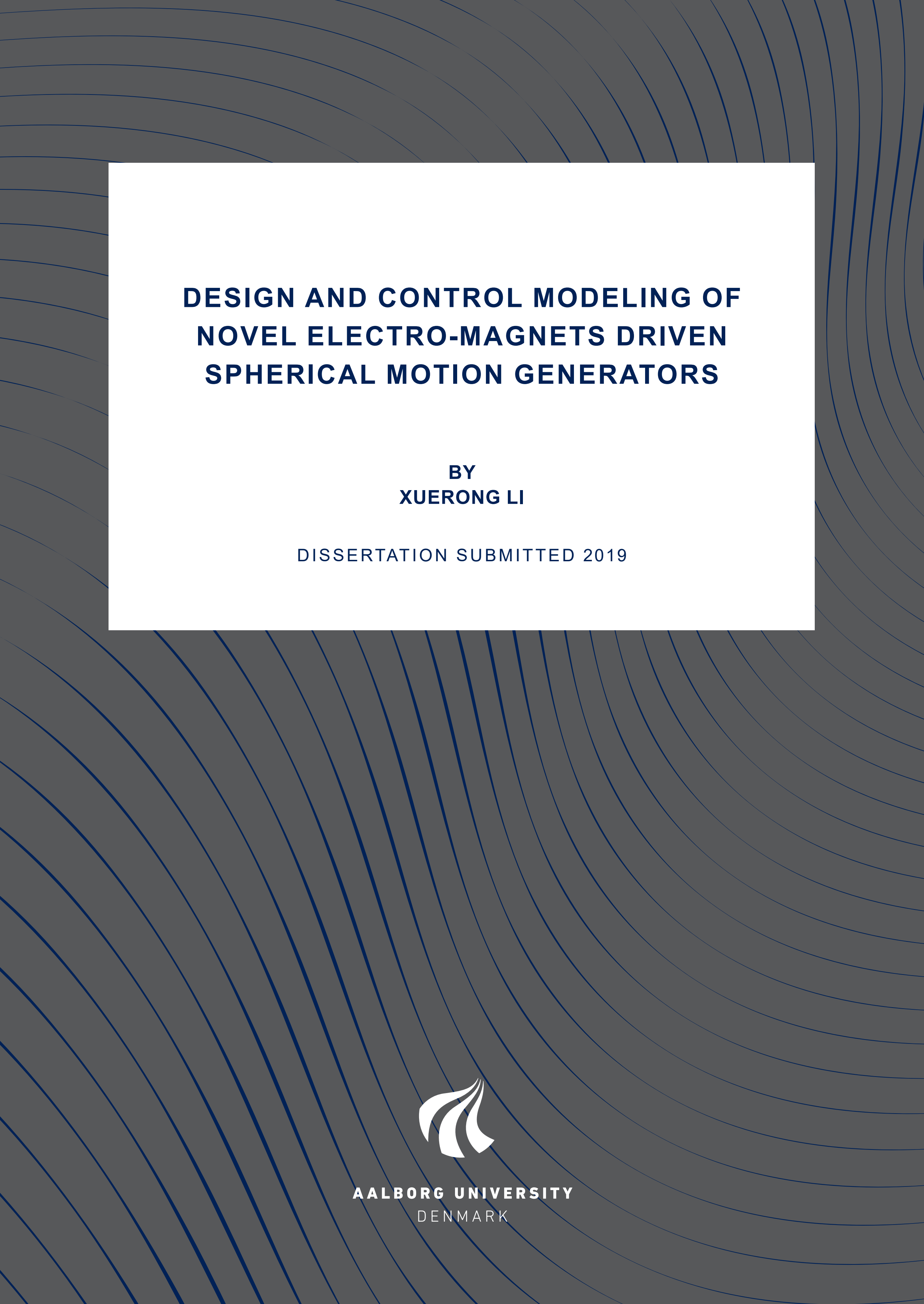

DESIGN AND CONTROL MODELING OF NOVEL ELECTRO-MAGNETS DRIVEN SPHERICAL MOTION GENERATORS

BY
XUERONG LI

DISSERTATION SUBMITTED 2019

AALBORG UNIVERSITY
DENMARK

Design and Control Modeling of Novel Electro-magnets Driven Spherical Motion Generators

Ph.D. Dissertation
by

Xuerong Li
Department of Materials and Production, Aalborg University
Fibigerstræde 16, 9220, Aalborg, Denmark
E-mail: xl@mp.aau.dk

Dissertation submitted September 6, 2019

Dissertation submitted: September 6, 2019

PhD supervisor: Shaoping Bai, Associate Professor
Aalborg University

PhD Co-supervisor: Ole Madsen, Professor
Aalborg University

PhD committee: Kaiyuan Lu, Associate Professor (chairman)
Aalborg University

Jouni Mattila, Dr.Tech.
Tampere University of Technology

Yan Jin, Reader
Queen’s University Belfast

PhD Series: Faculty of Engineering and Science, Aalborg University

Department: Department of Materials and Production

ISSN (online): 2446-1636
ISBN (online): 978-87-7210-499-7

Published by:
Aalborg University Press
Langagervej 2
DK – 9220 Aalborg Ø
Phone: +45 99407140
aauf@forlag.aau.dk
forlag.aau.dk

Printed in Denmark by Rosendahls, 2019

Abstract

Spherical motion generator is a type of multi-degree-of-freedom devices to generate pure rotational motions and they can be found in many potential applications such as machine tools, solar panels, orientating devices and medical instruments. A spherical motion generator can be built by means of either spherical motors or spherical mechanisms. While many designs of spherical motion generators have been proposed, existing spherical motion generators show limitations in their large volume and weight and performances. New spherical motion generators characterized with simple and compact structure, low inertia and high accuracy are desirable, for which analytical modeling and advanced control techniques are requisite to support the development work.

This thesis aims to develop novel electromagnetic driven spherical motion generators. The focus is on the system modeling and analysis of integrated mechanism and electromagnetics design for the new motion generator. Kinematics, dynamics, analytical magnetic and torque modeling and control are covered in this thesis.

The thesis introduces first the integrated design of the new electromagnetic driven spherical motion generator. The design combines the kinematics of the spherical parallel manipulator and the electromagnetic driven principle of the permanent magnet spherical actuator, which features with a simple structure and low inertia.

The kinematics and dynamics of the new design is studied, addressing the kinematic Jacobian matrix, singularity and workspace analysis and dynamic modeling etc. Analytical magnetic and torque models are obtained for further study of electromagnetic actuation.

The thesis describes finally high-accuracy control of the spherical motion generator. The dynamic model of the spherical motion generator in task space will be established, with which the model uncertainties and external disturbances are duly considered. Addressing the uncertainties in the model, a robust adaptive switching learning control algorithm is developed which can improve the tracking performance of the spherical motion generator. A co-simulation platform by Matlab/Simulink and ADAMS was devel-

oped, with simulations conducted to reveal the dynamic performance of the motion generators.

The thesis contributes to the state-of-the-art of spherical motion generator design and modeling. A design which integrates spherical parallel manipulator and electromagnetic motors was for the first introduced and developed. The highly integrated electromechanical design can bring the system into a more compact and flexible structure. Compared with the conventional combination of single motors to implement multi-dof rotations, multi-dof actuation by an integrated electromagnetic driving component greatly improves the performance of the system. Moreover, analytical models are investigated including kinematic and dynamic analysis, magnetic field and torque modeling and high-precision control design, which constitutes the whole systematic modeling.

Resumé

En sfærisk bevægelsesgenerator er en type bevægelsesenhed, som, gennem kombination af elektromagnetisk aktuering og parallelmekanisme, kan aktuere rotationsbevægelse med 3 frihedsgrader. Der er mange potentielle anvendelser af en sådan enhed, f. eks. i værktøjsmaskiner, solpaneler, og medicinske instrumenter. En sfærisk bevægelsesgenerator kan bygges ved hjælp af enten sfæriske motorer eller aktuerede sfæriske mekanismer. Der eksisterer idag mange forskellige designs af sfæriske bevægelsesgeneratorer. Deres anvendelse er imidlertid begrænset på grund af deres store volumen, vægt og ydeevne. Der er derfor behov for nye sfæriske bevægelsesgeneratorer, der er karakteriseret ved en enkel og kompakt struktur og tilgodesér lav inerti og høj nøjagtighed. Dette behov skal understøttes igennem analytisk modellering og brug af avancerede styrings- og reguleringsteknikker.

Dette PhD-projekt sigter mod at udvikle nye elektromagnetiske drevne sfæriske bevægelsesgeneratorer. Fokus er på systemmodellering og på analyse af et integreret mekanisk og elektromagnetisk design af den nye bevægelsesgenerator. Kinematik, dynamik, analytisk modellering af elektromagnetiskaktuering og mekanisk moment samt styring er dækket i denne afhandling.

Indledningsvis introduceres det integrerede design af den elektromagnetisk drevne sfæriske bevægelsesgenerator. Designet kombinerer kinematikken i en bestemt sfærisk parallel-manipulator og det elektromagnetiske drev i en sfæriske aktuator med permanentmagneter, der har en enkel struktur og lav inerti.

De kinematiske og dynamiske egenskaber af de nye design analyseres. Dette indebærer bla en opstilling af Jakobianten, en analyse af singulariteter og arbejdejdsområde, samt en opstilling af en dynamisk model. Der opstilles analytiske modeller for elektromagnetisk aktuering og mekanisk moment.

PhD-rapporten beskriver ligeledes hvorledes en nøjagtig styring af den sfæriske bevægelsesgenerator kan realiseres. Den dynamiske model for den sfæriske bevægelsesgenerator opstilles i arbejdsområdet, med hensyntagen til modelunøjagtigheder og eksterne forstyrrelser. For at kompensere for modelunøjagtighedererne er der udviklet en robust adaptiv styringsalgoritme, der kan forbedre bevægelsesgeneratorens ydelse. Til simulering af de dy-

namiske egenskaber af den udviklede bevægelsesgenerator er der udviklet en integreret simuleringsplatform med Matlab/Simulink og ADAMS.

PhD projektet bidrager til state-of-art inden for design og modellering af sfæriske bevægelsesgeneratorer. Et design, der kombinerer en sfærisk parallel mekanisme med elektromagnetiske aktuering er introduceret og udviklet. Det integrerede elektromekaniske design muliggør en mere kompakt og fleksibel struktur. Derudover opnås, sammenlignet med konventionelle løsninger, en væsentlig forbedring af systemets ydelse. Yderligere bidrager projektet med en række analytiske modeller som understøtter en samlet systemisk analyse, herunder kinematiske og dynamiske modeller, magnetisk felt- og momenttmodellering, samt design af styring med henblik på høj præcision.

Publications

Parts of the work have been published in peer-reviewed scientific journals and international conferences.

Journal Papers

1. Xuerong Li, Jingmeng Liu, Weihai Chen, and Shaoping Bai. "Integrated design, modeling and analysis of a novel spherical motion generator driven by electromagnetic principle." *Robotics and Autonomous Systems*, 106 (2018): 69-81. doi:10.1016/j.robot.2018.04.006
2. Xuerong Li, Shaoping Bai, and Ole Madsen. "Dynamic modeling and trajectory tracking control of an electromagnetic direct driven spherical motion generator." *Robotics and Computer-Integrated Manufacturing*, 59 (2019): 201-212. doi:10.1016/j.rcim.2019.04.009
3. Xuerong Li, Jingmeng Liu, Weihai Chen, and Shaoping Bai. "Analytical magnetics and torque modeling of a multi-layer electromagnetic driven spherical motion generator." *Journal of Magnetism and Magnetic Materials*, 493 (2020): 165707. doi:10.1016/j.jmmm.2019.165707
4. Shaoping Bai, Xurong Li, and Jorge Angeles. "A review of spherical motion generation using either spherical parallel manipulators or spherical motors." *Mechanism and Machine Theory*, 140 (2019): 377-388. doi:10.1016/j.mechmachtheory.2019.06.012

Conference Papers

1. Xuerong Li, Shaoping Bai, Weihai Chen, and Jingmeng Liu. "Integrated design and modelling of an electro-magnets driven spherical parallel manipulator." In *2017 IEEE International Conference on Advanced Intelligent Mechatronics (AIM)*, Munich, Germany, pp. 1209-1214, July, 2017. doi:10.1109/AIM.2017.8014183

2. Xuerong Li, Shaoping Bai, Weihai Chen, and Jingmeng Liu. "Torque modelling and current optimization of a spherical actuator built as an electro-magnets driven spherical parallel manipulator." In *2017 IEEE International Conference on Cybernetics and Intelligent Systems (CIS) and IEEE Conference on Robotics, Automation and Mechatronics (RAM)*, Ningbo, China, pp. 626-631, November, 2017. doi:10.1109/ICCIS.2017.8274850

Contents

List of Figures

Preface

The thesis is submitted according to the requirements for the Doctor of Philosophy at Faculty of Engineering and Science, Aalborg University (AAU). The work has been carried out during the period from November 2015 to October 2019 at the Department of Materials and Production (MP), AAU. This work is supervised by Associate Professor Shaoping Bai, AAU and co-supervised by Professor Ole Madsen, AAU.

I highly appreciate my supervisor, Associate Professor Shaoping Bai for his splendid supervision and support. His research creativity, scientific attitude and working efficiency inspire me a lot on my work. I also would like to thank my co-supervisor, Professor Ole Madsen, for always sharing his expertise to my study.

I would like to acknowledge Associate Professor Kaiyuan Lu at Department of Energy Technology, AAU and Wenqi Lu at Faculty of Mechanical Engineering and Automation, Zhejiang Sci-Tech University for their technical support. In addition, I appreciate Professor Weihai Chen, at School of Automation Science and Electrical Engineering, Beihang University (BUAA) for his help in my research and during my exchange study in BUAA.

I would like to extend my appreciation to my kind and helpful colleagues. I also personally thank my family and friends for their companionship and support.

Funding from the Chinese Scholarship Council (CSC) is gratefully acknowledged.

Xuerong Li
Aalborg University, September 6, 2019

Chapter 1

Introduction

The research work presented in this thesis aims at developing an integrated design of a new 3-degree-of-freedom (dof) spherical motion generator. The novel electromagnetic driven spherical motion generator integrates the 3-RRR (Revolute-Revolute-Revolute joint) spherical parallel manipulator with electromagnetic driving principle of permanent magnet spherical actuators. Modeling and control of the multi-dof manipulator will be focuses of the study to achieve the objectives. Analytical magnetic field and torque models are proposed for the electromagnetic actuation of the spherical motion generator and control strategies are established for the spherical motion generator. Numerical simulations and experiments are designed to compared with the analytical models. Results are obtained to verify the integrated system.

1.1 Background

A spherical motion generator is a device that generates multi-degree of pure spherical rotations. Spherical motion generators can be found widely potential applications in medical apparatus [1, 2] and robotic applications [3], which require flexible spherical motion with large workspace in high accuracy and simple structure. Spherical motion generators can be implemented by two major ways, namely, spherical manipulators of serial and parallel configurations and spherical actuators [4, 5], as reviewed in Sec. 1.2.

A 3-dof spherical parallel manipulator is a closed mechanism constructed with three identical serial chains in parallel. It is characterized that all the links intersect at a common rotational center, which can implement a 3-dof pure rotational movement. Compared with conventional serial mechanisms and 6-dof parallel manipulators, the spherical parallel manipulators have the advantages of compact structure, high precision and good stability, which shows wide potential applications in high-accuracy machining, aerospace positioning system and robotic system. However, there is no effective solutions to the actuation of spherical parallel manipulators. Generally, the parallel manipulators are driven by single motors and corresponding connectors that are attached to each joints. On the one hand, the gears and transmission gears increase the hysteresis errors; on the other hand, the attached motors bring extra weight to the system, which influences the dynamic performance seriously and increases the power loss. Finally, the movement accuracy of the spherical parallel manipulator cannot be guaranteed.

Alternatively, spherical actuators can generate multi-dof spherical movement in one unit. A spherical actuator is generally constructed by permanent magnet rotor arrays and a series of stator coils which interact with each other to produce different electromagnetic forces in order to actuate the end-effector in 3D spherical movement. Nonetheless, the applications of the spherical actuators are confined due to its complex machining and the lack of high-precision and real-time position detection methods.

In the light of the abovementioned considerations, spherical motion generators that have the advantages of both the coaxial spherical parallel mechanism and the electromagnetic driving principle of spherical actuators are required. To achieve this goal, an integrated electromagnetic driven spherical motion generator is proposed in this thesis, which will be investigated in several aspects including electromechanical integrated design, kinematic and dynamic modeling, analytical magnetic modeling and high-precision control algorithms.

1.2 Reviews of spherical motion generators (SMG)

Spherical motion generators can be implemented by different principles and realizations, as shown in Fig. 1.1. From the point of mechanism, the spherical motion can be produced by conventional serial mechanism or multi-dof spherical parallel manipulators. From the perspective of actuation principle, the spherical motion generator can be designed as spherical actuators including spherical motors, actuated spheres which have been applied in spherical robots [6, 7].

1.2.1 Spherical parallel manipulators (SPM)

A spherical motion generator can generate spherical motion either in one, two or three degree of freedoms. One-dof spherical four-bar linkages are investigated in [9, 10]. Two-dof spherical motion generators are developed for applications such as pointing devices [11] and pitch-roll wrist [12]. However, most spherical motions are required in three degree of freedoms. Spherical motion can be realized by spherical mechanisms, either in serial or parallel

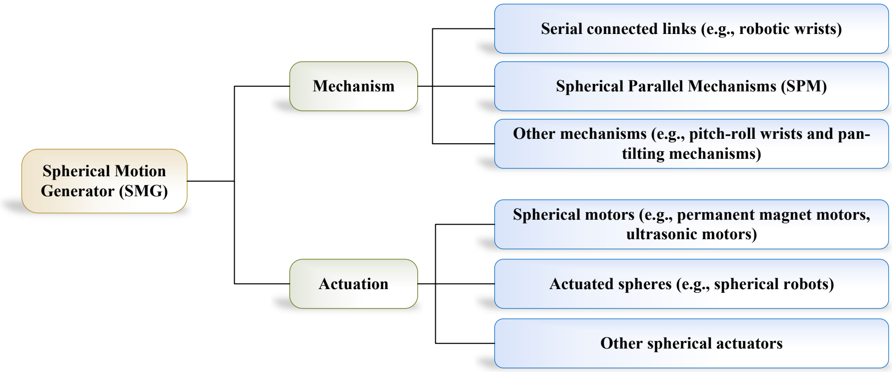

Figure. 1.1. Classification of spherical motion generators [8]

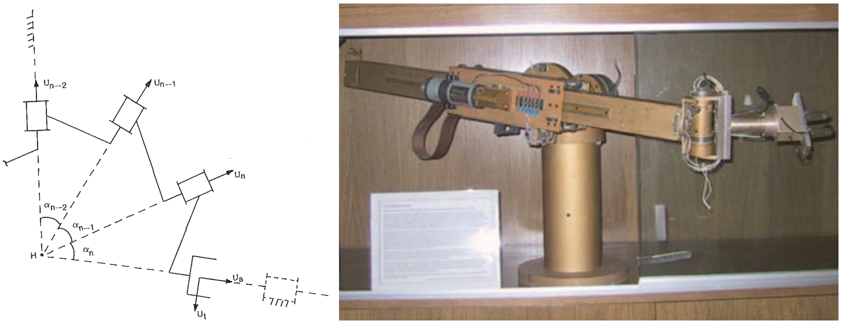

(a) Spherical four-bar linkage

(b) Stanford manipulator

Figure. 1.2. Spherical serial mechanism configurations, driven by ordinary single-axis motors. Spherical motion generators developed with serial configurations were reported in [13–15], shown as Fig. 1.2. The serial mechanism is characterized with the advantages of simple structure, low cost and large workspace. However, the driving motors are attached with each joints, which leads to the increment of the inertia of moving parts. In addition, the errors will be accumulated and amplified at the end-effector, which cannot meet the high-precision application requirement.

Figure. 1.3. Stewart platform

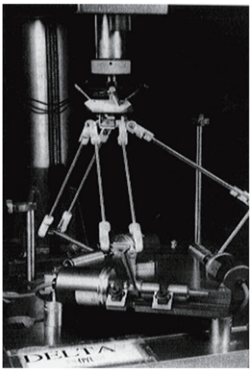

Figure. 1.4. Delta robot

Many spherical motion generators are designed as the type of spherical parallel manipulators. Compared with the serial ones, spherical parallel manipulators offer larger load capacity, better accuracy, greater rigidity and mass-reduction design. Spherical parallel manipulator pertains to the parallel robots, which have been studied extensively for many years. Parallel robots are used mainly in industrial fields. In recent years, parallel robot applications in other areas such as medical and service systems are also increasing. Stewart platform and the Delta robot are two of the most widely used parallel manipulators of different dofs. The Stewart platform [16] is a parallel mechanism with six degrees of freedom firstly designed for the flight simulator (Fig. 1.3), which has been extended for docking system and robotic crane [17], etc. The Delta robot [18] is developed by Clavel, which can perform fast positioning as shown in Fig. 1.4. As one example, the Delta robot has been used as the actuator of 3D printer called Rostock [19].

In recent years, spherical parallel manipulators [20–22], shown in Fig. 1.5, attract much more attention. Spherical parallel manipulators can implement pure rotations with the advantages of larger workspace and less interfering between components, which shows widely potential applications.

The spherical parallel manipulator is firstly introduced by Asada and Granito in 1985 [23], which is shown in Fig. 1.6. It is constructed by a closed loop mechanism in which an output shaft and three coaxial input shafts are

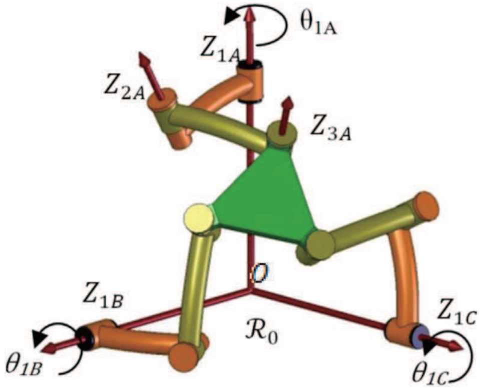

Figure. 1.5. 3-dof spherical parallel manipulators

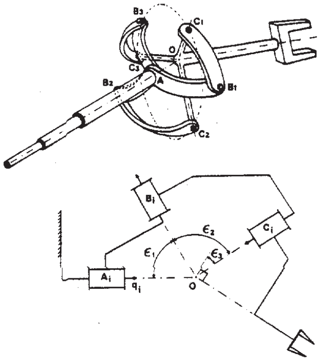

Figure. 1.6. SPM by Asada

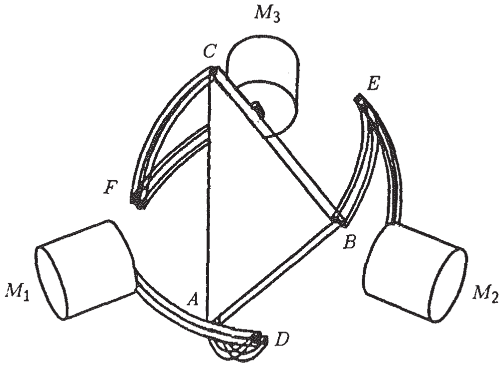

Figure. 1.7. SPM by Gosselin and Angeles

connected by three intermediate links. It can obtain limited pitch and yaw rotations and unlimited spinning motion around the spherical center **O**. Another type of spherical parallel manipulator is developed by Gosselin and Angeles in 1989 [4]. This kind of spherical parallel manipulator is generally constructed with two rigid platforms that are connected by three identical serial chains, shown as Fig. 1.7. One platform is the base which is attached to the fixed reference frame. The other one is the mobile platform that can rotate in its workspace. The links of each serial leg are usually connected with each other by spherical joints, revolute joints or prismatic joints. The actuation of the spherical parallel manipulator is implemented by attaching motors to each joints that are fixed on the base platform. The spherical parallel manipulators are best known for the Agile Eye applied in camera orienting devices [4, 24], and the Agile Wrist that is widely used in robotics and medical apparatus [25], as shown in Figs. 1.8 and 1.9, respectively. Compared with general 3-dof parallel manipulators, they can achieve more flexible rotations in a workspace with a torsion angle of $\pm 30^\circ$ and a conic angle of 140°, which can meet most occasions of spherical movement. Nevertheless, general spherical parallel manipulators are confined when they are applied in the fields such as robots and underwater vector propulsion devices which require large-scale spherical motion and infinite spinning motion [26, 27]. For example, a thruster is a crucial component of the underwater robot. The single propeller can produce propulsion along the axial direction, and an extra vectored thruster is needed to generate multi-dimensional propulsion to implement different steering motion. The steering motion is conventionally accomplished by the serial mechanism or 6-dof Stewart robots, however, only 3-dof rotational movement is required. Therefore, 3-dof coaxial spherical parallel manipulators provide new solution for the vectored propulsion technique, which can implement the propeller rotation and the adjustment of spatial attitude.

A 3-RRR spherical parallel manipulator with virtual coaxial shafts is developed by Bai [28], shown as Fig. 1.10(a). It is kinematically equivalent to the SPM by Asada and Granito, which can achieve unlimited spinning motion. Each sliding unit is attached with a motor which can move around the circular guide by gear transmission. Moreover, Bai analyzed the 3-RRR coaxial spherical parallel manipulator from the aspects of kinematics, dynamics and optimum design to improve its performance [29, 30]. Another spherical parallel manipulator with circular prismatic pairs is proposed by Li [31], with a prototype displayed in Fig. 1.10(b). Sudki et al. [32] apply the coaxial spherical parallel manipulator into marine propulsors as shown in Fig. 1.11(a). Tursynbek [33] developed a 3-dof spherical parallel manipulator by 3D printing technology and implemented its position control (Fig. 1.11(b)). Enferadi et al. [34] analyzed the workspace optimization and singularity of the spherical parallel manipulator with coaxial input shafts for the high-precision po-

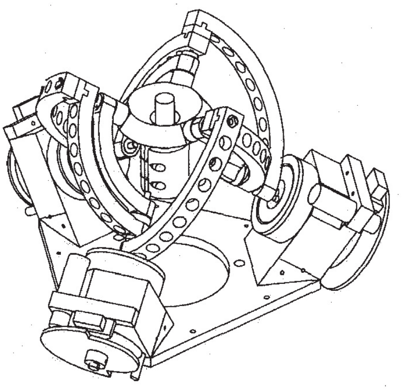

Figure. 1.8. The Agile Eye

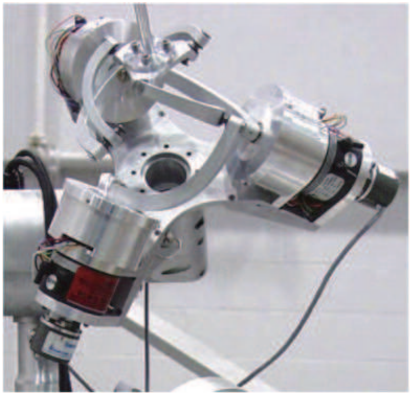

Figure. 1.9. The Agile Wrist

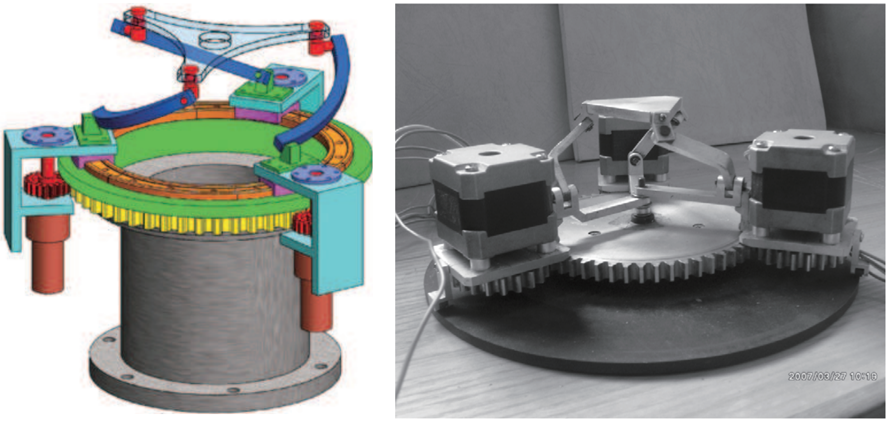

(a) SPM designed by Bai

(b) SPM designed by Li

Figure. 1.10. Spherical parallel manipulator with virtual coaxial shafts sitioning and rehabilitation applications, as illustrated in Fig. 1.11(c).

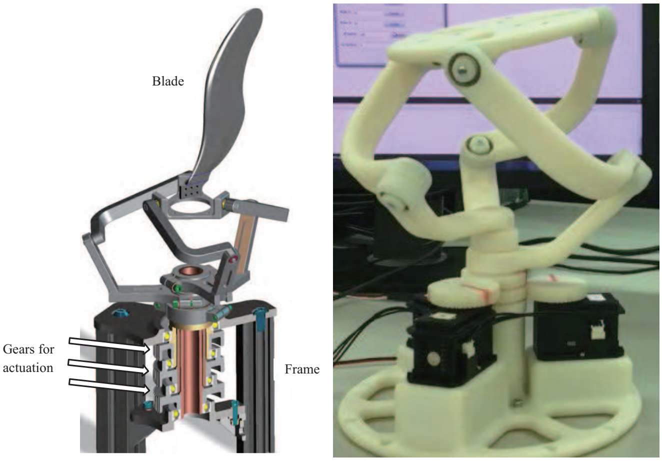

(a) SPM designed by Sudki (b) SPM designed by Tursynbek

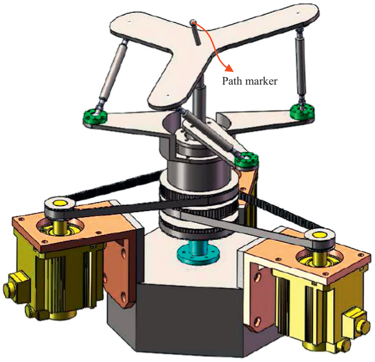

(c) SPM designed by Enferadi

Figure. 1.11. Spherical parallel manipulator with coaxial shafts

Above all, the actuation of spherical parallel manipulators is usually realized by separate driving motors. In Fig. 1.10, the motors are attached with the moving active links, and the motors' movement are transmitted to the end-effector of the SPM with virtual coaxial shafts by gear transmissions. The symmetric design simplifies the mechanism and fabrication. However, the attached gears and driving motors increase the weight and volume of the mechanism seriously, which will further influence the performance of the system. From Fig. 1.11, the driving motors are fixed at the base, and the coaxial input shafts are actuated by the gear or belt transmission, which causes hysteresis errors. Moreover, the elastic deformation and nonlinear friction will influence the performances of dynamics. Therefore, in addition to the kinematics problems and dynamic modeling, another crucial issue of the spherical parallel manipulators is the actuation.

1.2.2 Spherical actuators

Alternatively, multi-dof spherical motion can be implemented by spherical actuators which are a new type of electromagnetic devices similar to the human joints. A spherical actuator is designed in a compact structure with advantages of low inertia moment, rapid response and high energy density.

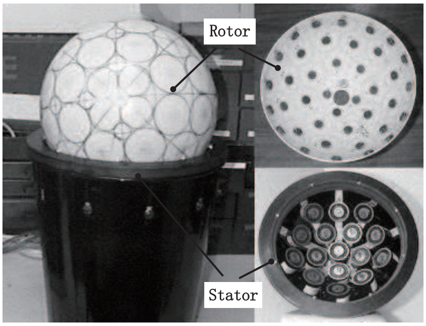

Figure. 1.12. Spherical stepper motor

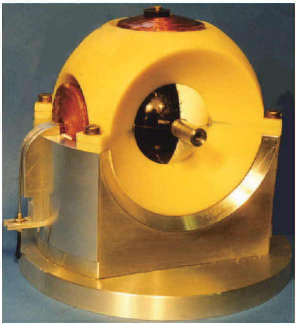

Figure. 1.13. PM spherical actuator

The first 2-dof spherical motor was developed by Williams et al. in the 1950s [35]. Since then, spherical motors with different structure and working principles have been designed [36–40]. Chirikjian et al. [41–43] introduced a spherical stepper motor as depicted in Fig. 1.12. The rotor of the spherical stepper motor consists of 80 rare-earth permanent magnets placed on the internal surface of a 12-in-diameter hollow plastic sphere. A number of stator coils with soft iron cores are distributed in a spherical cap for obtaining a large range of spherical movement. Wang et al. [44–46] developed 3-dof permanent magnet (PM) spherical actuators (Fig. 1.13). The spherical rotor consists of two pairs of permanent magnet quarter-spheres. Four sets of coils are housed within the spherical stator. This design contributes to simplifying the magnetic torque modeling and the design of control algorithms. As the rotor rotates within the spherical stator on a low friction surface coating, long-lasting wear of the coating cannot ensure the stability and accuracy of the system.

Lee et al. reported a variable-reluctance (VR) spherical motor [47], as shown in Fig. 1.14(a). A number of stator windings are housed in a hemisphere evenly. The permanent magnets are distributed on the rotor surface. The stator is connected with the permanent magnet rotor by means of gimbals. The end-effector of the rotor can roll freely on the gimbals. By varying

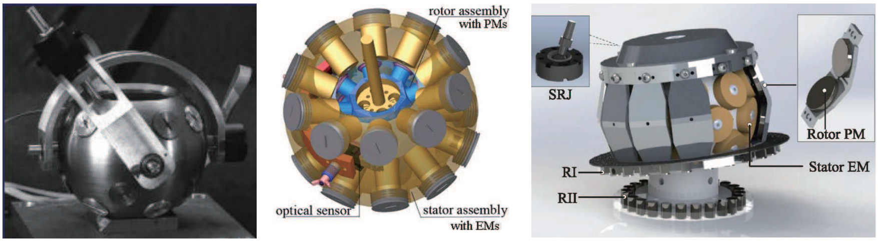

(a) VR spherical motor (b) SWM (c) PM spherical actuator

Figure. 1.14. Spherical actuators by Lee et al.

the input currents of the stator windings, there will be a 3-dof rotational movement at the end-effector of the rotor. However, the additional friction between the slide track and the rotor influences the system performance seriously. Controllers were developed to improve the precision [48]. In [49], a computed torque method which is widely used in the robotic area, was utilized for the control of VR spherical motor. Lee and Son designed a spherical wheel motor (SWM) [50, 51]. It consists of 20 stator air-core coils and 16 cylindrical PMs as illustrated in Fig. 1.14(b). A distributed multipole model (DMP) was proposed which was originated from the concept of a magnetic dipole. The typical orientation detection is usually to use the mechanical links with attached encoders, which increases the frictional torque greatly. The DMP method was then exploited to develop a two-dof orientation sensors to measure the orientation of the SWM in real-time control [52]. Lee and Bai investigated a 3-dof permanent magnet spherical actuator (Fig. 1.14(c)) by introducing the direct field-feedback control (DFC) for real-time controlling without orientation sensing system, which was applied in conformal printing of curved electronics [53, 54]. Toyama and Mashimo developed spherical ultrasonic motors which adopted the ultrasonic vibration to drive the spherical motor [55–57]. It can be designed in compact size and large movable range as shown in Fig. 1.15. The friction drive principle improves the responsiveness of the system. However, it influences the position precision and durability.

To improve the performance of the PM spherical motors, in-depth study on the PM rotor array is conducted. Yan designed the permanent magnet rotor arrays in 3D structure (Fig. 1.16), and employed the spherical harmonics (SH) to study the 3D rotor array for further control implementation and parameter optimization [58]. Xia presented a Halbach permanent magnet array for the spherical actuator in Fig. 1.17, to obtain a magnetic field with a kind of sinusoidal distribution [59]. Chen et al. proposed a high-precision and real-time orientation detection system for the PM spherical actuators [60]. As shown in Fig. 1.18, a passive spherical joint is introduced to connect the ro-

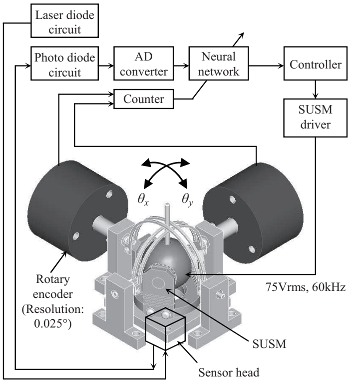

Figure. 1.15. Spherical ultrasonic motors

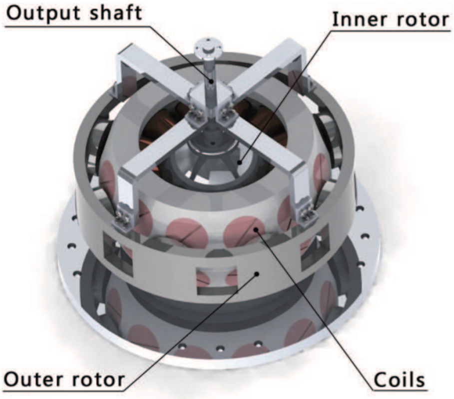

Figure. 1.16. PM spherical motor with 3D array

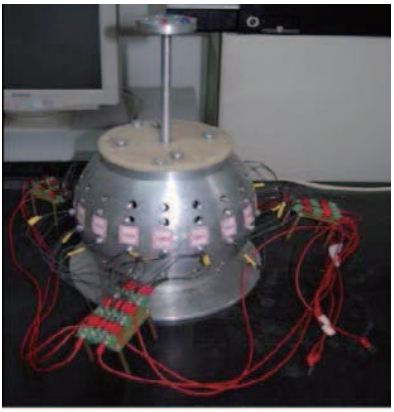

Figure. 1.17. PM spherical motor with Halbach rotor array

tor with the base. The rotor orientation is measured by the spherical joint with which the rotary encoder and two-axes tilt sensor are incorporated. In addition, corresponding trajectory tracking control algorithms were developed [61, 62].

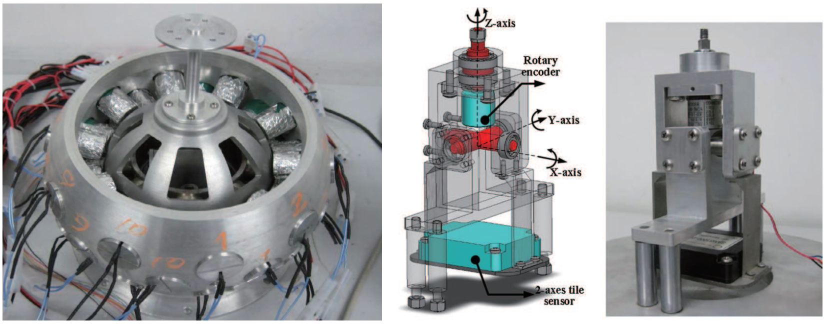

(a) PM spherical actuator prototype (b) Spherical joint

Figure. 1.18. A PM spherical actuator with position detection system [60]

A PM spherical actuator consists mainly of a spherical permanent magnet rotor array and a series of stator coils evenly housed in a spherical shape. PM spherical actuators have the advantages of rapid response, compact structure and high energy density. Nevertheless, due to the limitation of mechanical design, the maximum tilting angle is confined [62]. The spherical motors are subjected to relatively large size and heavy mass because of the utilization of the permanent magnet array and the supporting holder [63]. In addition, owing to uncertainties and nonlinearities in the dynamic models, the real-time control for the PM spherical actuators is also a challenging problem.

1.3 A new concept of integrated spherical motion generators

New designs of 3-dof spherical motion generators will be studied in this work. The new designs allow an integration of the spherical parallel mechanics and permanent magnet spherical actuators' driving principle for an actuator with high performance. A concept of integrated design of the electromagnetic driven spherical motion generator is proposed [64]. The multi-dof electromagnetic driven approach will be applied for the spherical motion generator.

The new concept was developed on the spherical parallel manipulators with virtual coaxial shafts proposed by Bai [28], which suggests a promising approach for performance improvement. The spherical parallel manipulator uses a circular guide with three free-moving sliding units as the base platform in Fig. 1.10(a). The sliding units are made of permanent magnets and used as rotors. There are a series of stator coils distributed evenly around the rotors. The end-effector will be actuated by the interaction between the rotor sliding units and the stator coils, as shown in Fig. 1.19(a). Compared with heavy rotor of permanent magnet spherical actuators, the sliding unit of low mass can be easily driven by the electromagnetic force.

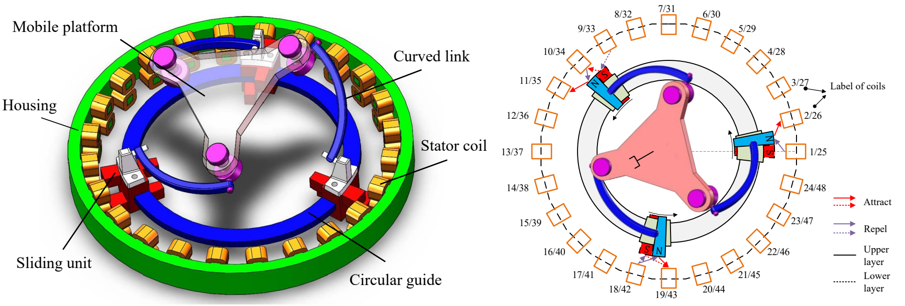

(a) Conceptual design

(b) Working principle

Figure. 1.19. Concept of the electromagnetic driven SMG

Figure 1.19(b) depicts the working principle of the spherical motion generator. Every sliding unit is consisting of two stagger permanent magnets with opposite magnetization in two layers, namely, an upper layer and a lower layer. The stator coils are distributed uniformly in two layers outside the rotor. The upper permanent magnet is mainly interacted with stator coils in the upper layer, in the same way, the lower permanent magnet is interacted with the stator coils in the lower layer. Then the sliding units will be actuated by the electromagnetic forces between the permanent magnet poles and the stator coils. All the stator coils are involved in the actuation of each sliding unit, which can be regarded as a multi-dof actuating method.

The spherical motion generator can operate in two type of motions, namely, a pure spinning motion and a general spherical motion. For the pure spinning motion, the three sliding units are driven in synchronous movement with equal torques simultaneously, then the mobile platform will rotate about its own central axis. For the general spherical motion, the three sliding units are actuated by different torques, then sliding units' relative motions will generate a 3D rotational movement at the end-effector of the mobile platform.

An embodiment of the spherical motion generator is displayed in Fig. 1.20. In the embodiment, the three sliding units are mounted on the circular guide through three identical links. The circular guide is composed of a pair of

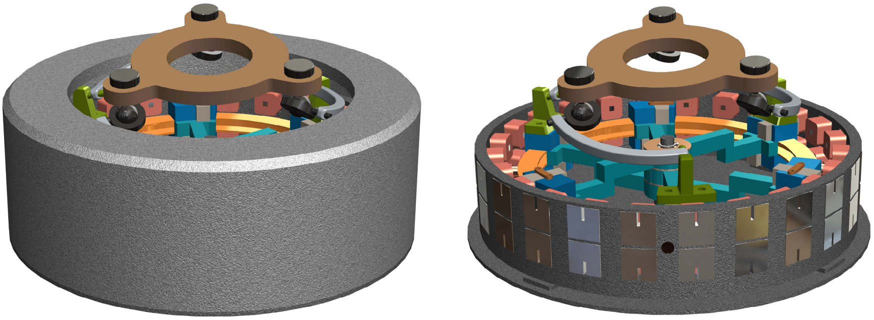

(a) Overall design (b) Internal view with housing removed

Figure. 1.20. Embodiment of the electromagnetic driven SMG

HCR guides from THK, which can obtain a high-precision movement of the sliding units. A symmetric layout of every sliding unit is adopted to keep the balance of the rotor.

Compared with conventional motor-driven spherical parallel manipulators and permanent magnet spherical actuators, the newly designed electromagnetic driven spherical motion generator brings some advantages. The non-contact electromagnetic driving principle eliminates the utilization of motors and gears, which brings out less mechanical wear and no backlash. The new design is advantageous due to a more compact and flexible structure. Moreover, the spherical motion generator has a larger workspace than the spherical actuators, and can implement 360° spinning motion superior to typical parallel manipulators.

1.4 Research challenges

In this section, a brief state-of-art on the developed methodologies is introduced, particularly emphasizing on issues that are relevant to the research of the electromagnetic driven spherical motion generators.

1.4.1 Kinematics and dynamics modeling

Extensive research on kinematics and dynamics analysis has been carried out for spherical parallel manipulators [65–68]. Gosselin and Lavoie investigated the kinematic design of spherical parallel manipulators with different types [69]. Gosselin et al. developed a method for the type synthesis of non-overconstrained spherical parallel manipulators based on screw theory [70], and proposed a linear invariants (LI) of the rotation matrix for workspace analysis [71]. Bai and Angeles analyzed the input-output equation of a spherical four-bar linkage by combining two closure equations of single individual limbs, which is applied for further modeling of the spherical parallel manipulators [72, 73]. Gregorio solved the kinematic model of a 3-URC wrist with all equal legs, moreover, the position and mobility analysis were proposed [74]. In [75], a "tilt-and-torsion angles" representation was introduced as a useful analytical methodology to determine the workspace boundaries of general symmetrical spherical parallel manipulators. By using geometric approach and an appropriate set of coordinates, direct and inverse kinematic models of spherical parallel manipulators are obtained [76].

Dynamics of spherical parallel manipulator is essential for high-precision control. To obtain the dynamic equations of motion for the parallel manipulators, the methods such as Newton-Euler method [77], Lagrange formulation and the virtual work principle are exploited. In [4], Newton-Euler method was utilized to analyze the dynamics and a complete simulation has been developed to determine the forces and torques for any given trajectory. A dynamic model was developed to optimize the structural and geometric parameters with the classical Lagrange multipliers approach which is widely used for dynamic modeling of parallel mechanism with geometry constraints [29]. The virtual work principle was introduced to solve the inverse dynamic problem of a 3-RRR Agile Wrist spherical parallel robot [78]. Gibbs-Appell method was derived for a spherical parallel robot, which contributes to a simple form of dynamic model [79]. By combining D'Alembert's principle and Kane's method, an enhanced approach was designed to reduce the computational time during the dynamic calculation [80].

1.4.2 Analytical magnetic modeling methods

The actuation of the spherical motion generator is based on the working principle of the permanent magnet spherical actuator. Therefore, in this study, the rotors designed as either sliding units or cylindrical arrays are constructed by permanent magnet poles.

The permanent magnet poles are mainly manufactured in tile shape or cylindrical shape. A cylindrical-shaped permanent magnet with axial magnetization has the advantages of easy magnetization and fabrication. The cylindrical PMs can be applied in the rotor structure of actuators, which can decrease the inertial moment in order to improve the dynamic response [81, 82]. However, compared with cylindrical permanent magnets, the tile-shaped permanent magnets contribute to a more compact rotor structure which can avoid the increase of the air gap between the neighbouring cylindrical permanent magnets and enhance the magnetic field in the air. The conventional numerical method, finite element method can obtain good accuracy in view of nonlinear factors and complicated geometry shapes. However, it is deficient in the computational efficiency, which is not favourable for the optimization design and further real-time control. Therefore, analytical magnetic field and torque models with better accuracy are quite necessary, which is a challenging work.

Magnetic field modeling

Up to now, several methods have been studied on the magnetic modeling, such as spherical harmonics, distributed multipole, magnetic equivalent circuit, the charge and current models. Spherical harmonics are special functions defined on the surface of a sphere, which is employed to study the magnetic field distribution of spherical actuators analytically in [58, 59, 83, 84]. Distributed multipole method is generally used to calculate the magnetic field distribution of cylindrical-shaped permanent magnets, in which the permanent magnets are equivalent to magnetic dipoles [51, 52]. Magnetic equivalent circuit is a method that can analyze the magnetic field by meshing the device geometry into elements with reasonable precision and computational complexity [85]. The charge and current models are alternative methods, which can be applied for the permanent magnets efficiently by virtue of some special functions or approximation deformation of the magnet structure [86–89].

Torque modeling

The electromagnetic torque model is formulated analytically in terms of the analytical magnetic field models, which includes Lorentz force law, virtual-work method, moment principle and so on. The conventional Lorentz force law can seriously increase the calculation complexity due to the multiple integration, which can be usually applied for simple structure [90]. In the virtual-work method, a force is derived by evaluating the magnetic potential energy in the framework of the finite element method [91–93]. Dipole moment principle was introduced by Lim and Son, which simplified the computational process greatly to obtain the resultant torque generated by spherical actuators [94, 95].

1.4.3 Control algorithms

On account of the uncertainties and nonlinear behavior of the dynamic system, accurate tracking is a challenging work to implement. To improve the trajectory tracking performance of the actuators, many control algorithms have been developed.

As a classic control algorithm, the proportional-derivative (PD) controller is typically applied to yield a better trajectory tracking performance with the asymptotic stability by adjusting the control gains [50]. Nonetheless, PD controller cannot ensure the stability in high-speed applications, and the precision cannot be guaranteed by PD controller without the compensation for the uncertainties and disturbances of the dynamic systems [96]. Computed torque model (CTM) is a model-based control scheme which has been widely employed to eliminate the strong coupling and nonlinearities in the manipulator dynamics [97–99]. Compared with controllers such as PID [100] and augmented PD control, CTM can achieve an ideal control performance by overcoming the external disturbance [101].

Intelligent control algorithms are studied in recent years, such as neural networks, adaptive, robust controllers and so on [102, 103]. Neural networks and adaptive controllers can compensate for the uncertainties at the expense of computation efficiency, which are restricted to real-time control [104, 105]. Iterative learning control (ILC) has a strong robustness to the modeling uncertainties, thus it is appropriate for devices with repetitive tasks [106, 107]. Moreover, hybrid control algorithms that integrate ILC, adaptive and robust controllers are investigated, which are advantageous to the combined control methods [108–110].

1.5 Objectives and scope of the work

The PhD project is aimed at developing an electromagnetic driven spherical motion generator for the robot manipulator to generate accurate spherical movement in 3-dof rotation. The integrated system of the spherical motion generator can be implemented in an open-loop scheme and a closed-loop scheme, as displayed in Fig. 1.21. The objective of the open loop is to study the working principle of the SMG. Defining a desired trajectory of the end-effector, the desired torques can be obtained from the inverse kinematics and dynamics. The magnetic field and electromagnetic torque models are then utilized to compute the current inputs corresponding to the calculated desired torques. The obtained currents can be used to actuate the SMG to produce a 3-dof spherical motion. To investigate the control system which is essential for the practical use of SMG, a closed-loop system is designed. The control task is to determine the torques to ensure that the real motion tracks the desired trajectory.

The following objectives will be achieved in the project:

1. to design an integrated electromagnetic-mechanical actuator;
2. to establish the actuating models and analyzing the working principle;
3. to develop actuation control strategies to achieve efficient movement at the end-effectors.

To achieve these goals, this project will deal with the following research problems based on Fig. 1.21:

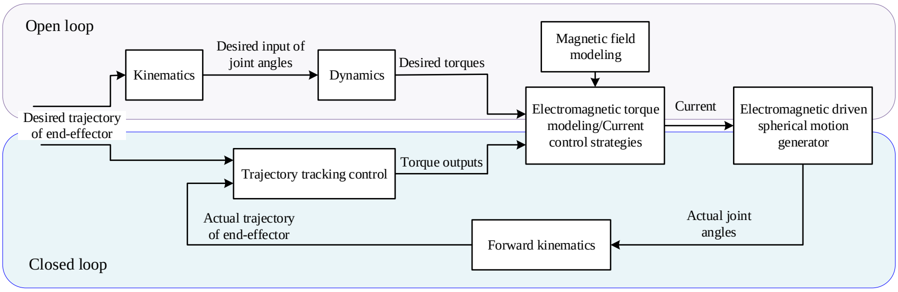

Figure. 1.21. Integrated system design

Kinematic analysis of coaxial spherical parallel manipulators. The 3-dof spherical motion is generally implemented by multi-dof spherical parallel manipulators. Conventional spherical parallel manipulator with fixed bases can obtain various spatial motion on the sphere, however, the workspace of the parallel manipulators is confined, particularly in the applications such as the underwater vector propellers that require unlimited spinning motion and a wide range of attitude motion. In addition, the nonlinearities and coupling among the kinematic chains increase the system complexity. 3-dof spherical parallel manipulators with coaxial shafts can realize spherical movement with unlimited spinning motion. Thus, for high-precision and high-speed applications with large-scale workspace, this study will investigate and improve the coaxial spherical parallel manipulators from the perspective of mechatronic design to develop an integrated spherical motion generator. The kinematics of the spherical motion generator will be studied and the Jacobian matrix will be derived for further singularity and workspace analysis.

The integrated multi-dof electromagnetic actuation. The actuation of the coaxial spherical parallel manipulators are mainly implemented by the combination of the single-axis motors and gear transmission, which influences the performance of the system due to the hysteresis errors. Therefore, an innovative electromagnetic actuation will be the focus of this work. The highly integrated electromagnetic driven design will avoid the problems caused by gear transmission. The novel actuator incorporates the spherical actuator principle with the spherical parallel manipulator to generate 3-dof rotations. In particular, ferromagnetic materials such as permanent magnets can be used as the rotor of spherical motor. A number of stator coils which are equally distributed around the circular guide can interact with the permanent magnets to actuate three permanent magnet sliding units in respective movement.

Analytical and numerical modeling. Analytical and numerical models of the magnetic field distribution and torque will be developed to study the actuation. The magnetic charge model is used to study the spatial magnetic field distribution. In the charge model, the permanent magnet poles of the rotor array can be equivalent to a spatial distribution of "magnetic charges" which are applied as a source term in the magnetostatic field equations. The complete solution for the magnetic flux density of the rotors can be calculated by the superposition of the magnetic flux density generated by each permanent magnet pole. The torque model can be obtained by Lorentz force law or the dipole moment principle. To simplify the control of the motion generator, the stator coils are constructed with non-ferromagnetic cores so that the torque output is proportional to the current output. The complete torque produced by multiple coils can be obtained by superposition principle. The analytical models are then compared and validated with the numerical Ansoft models and experiments.

Actuation control strategy. The torque is generated by the interaction of the permanent magnet rotor and the surrounding stator coils. The end-effector of the spherical motion can produce 3-dof rotational motion within the workspace through varying the current inputs of stator coils. Therefore, the current control is the premise of the position control. The current control strategy will be developed to realize that the separate rotors are controlled respectively by the stator coils. Moreover, the dynamic model of the spherical parallel manipulator is a complex system with the characteristics of nonlinearity and coupling, which will reduce the kinematic accuracy of the system. Besides, the uncertainties including the manufacturing errors, external disturbances and so on, are also key issues of the spherical parallel manipulators. Thus, another research emphasis is to design a hybrid control algorithm which can contribute to improving the trajectory tracking performance.

Prototyping and experiments. A prototype will be built based on the conceptual mechanical design. The experiment system which includes hardware design and software design will also be developed to control the spherical motion generator. The experiments will be performed to verify the modeling of the integrated spherical motion generator.

In summary, it is a great challenging work to design a novel integrated spherical motion generator which can combine the advantages of both the mechanical structure of spherical parallel manipulator and the innovative actuation principle of the spherical actuators. This thesis will investigate the electromagnetic driven spherical motion generators from several aspects including the structure design, kinematic and dynamic analysis, magnetic modeling and high-accuracy control.

1.6 Outline of thesis

The thesis consists of six chapters. The outline of the thesis is introduced as follows.

Chapter 1 provides necessary background and a summary of the state-of-art of spherical motion generators, mainly focusing on the spherical parallel manipulators and spherical actuators. The research challenges of electromagnetic driven spherical motion generators are analyzed, which initiated this study.

Chapter 2 introduces the analytical modeling of the spherical motion generators. Mathematic theory of integrated systems are described in detail for further study, including kinematics and dynamics, analytical magnetic methods, and analytical magnetic torque calculation.

Chapter 3-6 are the selected and representative publications through which the thesis subjects are treated specifically.

Chapter 3 describes the systematic design and modeling of an integrated spherical motion generator. The integrated design is constructed by a spherical parallel manipulator with virtual coaxial shafts and a multi-dof electromagnetic actuating unit. The integrated system is analyzed from several aspects: the kinematics and dynamics, the analytical magnetic field and torque modeling and preliminary trajectory tracking control with PD and computed torque methods, which evaluates the validity and rationality of the integrated design.

Chapter 4 presents a robust adaptive switching learning PD control algorithm for the integrated spherical motion generator to improve its trajectory tracking performance. The stability of the hybrid control algorithm is proved in details. A co-simulation platform is designed. The control algorithm is implemented by Matlab/Simulink and the virtual prototype is established and defined with parameters in ADAMS. Finally, the developed algorithm is verified effectively.

Chapter 5 describes analytical magnetic modeling and torque modeling of an integrated spherical motion generator with multi-layer electromagnetic actuations. The analytical magnetic model is developed based on the charge model and the transformation methods. The analytical torque model is established on the basis of the dipole moment principle which greatly simplifies the computation compared with the conventional integral calculation of Lorentz force law. Furthermore, these models are validated by numerical finite element methods and experiments.

Chapter 6 concludes this thesis, with a summary of observations from the project study and contribution. Future work is also suggested.

Chapter 2

Integrated analytical modeling

This chapter introduces the theoretical basis of the spherical motion generator, including the kinematics, dynamics, analytical magnetic field and torque modeling, followed by an example of an integrated SMG with multi-layer actuation.

2.1 Kinematics and dynamics of the spherical motion generator

The spherical parallel manipulators can be categorized into three types, general spherical parallel manipulators, spherical parallel manipulators with coaxial shafts, advanced spherical parallel manipulators with virtual coaxial shafts. Figure 2.1(a) displays the general type that was introduce by Gosselin and Angeles. By defining the parameter $\gamma = 0$ in Fig. 2.1(a), the three proximal links will form a coaxial structure at the joints connected to the base, which contributes to the reduction of the base platform. As a result, it can generate an unlimited spinning motion at the end-effector as depicted in Fig. 2.1(b). Based on the coaxial spherical parallel mechanism, a spherical parallel manipulator with virtual shafts was introduced by Bai [72] by using the sliding units to replace the proximal links. By introducing the circular guide along which the sliding units can move separately as shown in Fig. 2.1(c), the design is improved in enhanced stiffness and high symmetry. In this study, the mechanical design of the spherical motion generator is base on a 3-RRR spherical parallel manipulator with coaxial shafts.

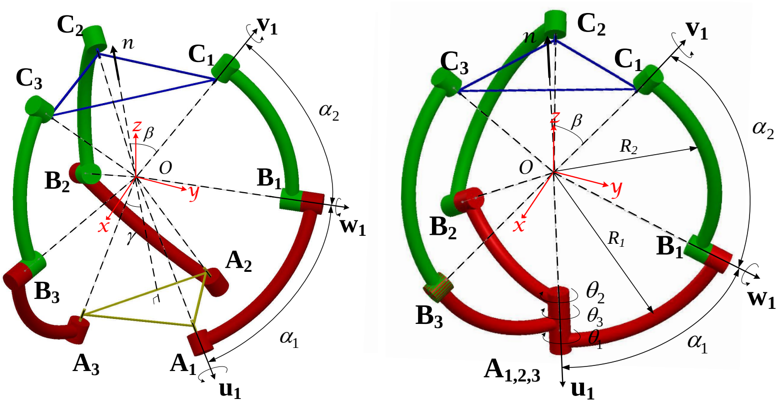

(a) General SPM

(b) SPM with coaxial shafts

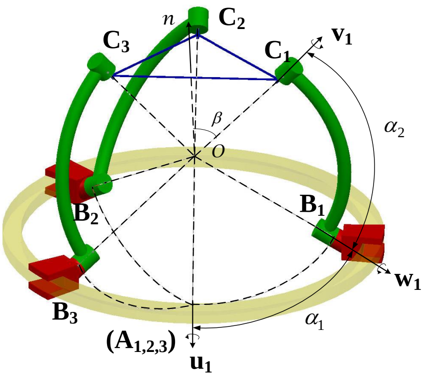

(c) SPM with virtual coaxial shafts

Figure. 2.1. Kinematic models of spherical parallel manipulators

2.1.1 Orientation representation

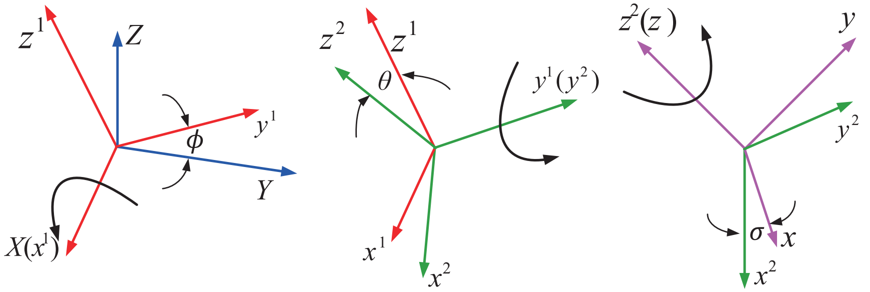

Figure. 2.2. Coordinate system conversion

In this work, X-Y-Z Euler angles are utilized to express the orientation of the mobile platform with respect to the global fixed coordinate system [111]. As shown in Fig. 2.2, the complete transformation matrix from the mobile coordinate system to base coordinate system is derived. The X-Y-Z coordinate system is rotated first about the X-axis by an angle ϕ, and then is rotated about the new y^1-axis by an angle θ. Finally the new coordinate system is rotated about the newest z^2-axis by an angle σ. The resulting rotating matrix **R** can be constructed by three transformation matrices

$$\mathbf{R}_\phi = \begin{bmatrix} 1 & 0 & 0 \\ 0 & \cos\phi & -\sin\phi \\ 0 & \sin\phi & \cos\phi \end{bmatrix} \mathbf{R}_\theta = \begin{bmatrix} \cos\theta & 0 & \sin\theta \\ 0 & 1 & 0 \\ -\sin\theta & 0 & \cos\theta \end{bmatrix} \mathbf{R}_\sigma = \begin{bmatrix} \cos\sigma & -\sin\sigma & 0 \\ \sin\sigma & \cos\sigma & 0 \\ 0 & 0 & 1 \end{bmatrix} \tag{2.1}$$

Thus, the rotation matrix can be formulated as

$$\begin{aligned} \mathbf{R} &= \mathbf{R}_\phi \mathbf{R}_\theta \mathbf{R}_\sigma \\ &= \begin{bmatrix} c(\theta)c(\sigma) & -c(\theta)s(\sigma) & s(\theta) \\ c(\phi)s(\sigma) + s(\phi)s(\theta)c(\sigma) & c(\phi)c(\sigma) - s(\phi)s(\theta)s(\sigma) & -s(\phi)c(\theta) \\ s(\phi)s(\sigma) - c(\phi)s(\theta)c(\sigma) & s(\phi)c(\sigma) + c(\phi)s(\theta)s(\sigma) & c(\phi)c(\theta) \end{bmatrix} \end{aligned} \tag{2.2}$$

where $s(\cdot) = \sin(\cdot)$ and $c(\cdot) = \cos(\cdot)$.

2.1.2 Kinematics modeling

The kinematic model of the spherical motion generator is derived from the kinematics of a spherical parallel manipulator [112, 113], as shown in Fig. 2.1(b). The axes of the revolute joints are denoted by unit vectors $\mathbf{u}_i$, $\mathbf{v}_i$ and $\mathbf{w}_i$, respectively, where i represents the link number, $i = 1, 2, 3$, and all the unit vectors point to the spherical center **O**. The unit vectors, $\mathbf{u}_i$, are parallel to

z-axis, which can be formulated as

$$\mathbf{u}_i = \begin{bmatrix} 0 & 0 & -1 \end{bmatrix}^{\mathrm{T}} \tag{2.3}$$

The unit vectors, $\mathbf{w}_i$, expressed in the stator coordinate system, are related to the actuated-joint angles θ_i,

$$\mathbf{w}_i = \begin{bmatrix} \Big(c(\eta_i)s(\theta_i) - s(\eta_i)c(\theta_i)\Big)s(\alpha_1) \\ \Big(s(\eta_i)s(\theta_i) + c(\eta_i)c(\theta_i)\Big)s(\alpha_1) \\ -c(\alpha_1) \end{bmatrix} \tag{2.4}$$

where $\eta_i = 2(i-1)\pi/3, i = 1,2,3$. Transferring the unit vector $\mathbf{v}_i^*$ of the top revolute joint axis from its local coordinate to the global coordinate system by the rotation matrix $\mathbf{R}$, the unit vectors, $\mathbf{v}_i$, are expressed as

$$\mathbf{v}_i = \begin{bmatrix} v_{ix} & v_{iy} & v_{iz} \end{bmatrix}^{\mathrm{T}} = \mathbf{R}\mathbf{v}_i^* \tag{2.5}$$

with

$$\mathbf{v}_i^* = \begin{bmatrix} -\sin\eta_i \sin\beta & \cos\eta_i \sin\beta & \cos\beta \end{bmatrix}^{\mathrm{T}}$$

The intermediate joint $\mathbf{w}_i$ and the revolute joint of the mobile platform $\mathbf{v}_i$ are connected together by the distal link $\mathbf{B}_i\mathbf{C}_i$ with a fixed central angle α_2. Therefore, the constrained function can be expressed as

$$\mathbf{w}_i \cdot \mathbf{v}_i = \cos\alpha_2, \ i = 1,2,3 \tag{2.6}$$

that is,

$$w_{ix} \cdot v_{ix} + w_{iy} \cdot v_{iy} + w_{iz} \cdot v_{iz} = \cos\alpha_2 \tag{2.7}$$

Substituting Eqs. (2.4) and (2.5) into Eq. (2.7), the new equations produce

$$D_i \sin\theta_i + E_i \cos\theta_i = F_i, \ i = 1,2,3 \tag{2.8}$$

with

$$\begin{cases} D_i = v_{ix}\cos\eta_i \sin\alpha_1 + v_{iy}\sin\eta_i \sin\alpha_1 \\ E_i = -v_{ix}\sin\eta_i \sin\alpha_1 + v_{iy}\cos\eta_i \sin\alpha_1 \\ F_i = \cos\alpha_1 v_{iz} + \cos\alpha_2 \end{cases} \tag{2.9}$$

Let $t_i = \tan(\frac{\theta_i}{2})$, then the following functions can be found

$$\sin\theta_i = \frac{2t_i}{1+t_i^2}, \ \cos\theta_i = \frac{1-t_i^2}{1+t_i^2} \tag{2.10}$$

Substituting Eq. (2.10) into Eq. (2.8), the equations are obtained as

$$(E_i + F_i)t_i^2 + 2D_i t_i - E_i + F_i = 0, \ i = 1,2,3 \tag{2.11}$$

Then the unknown parameter t_i can be solved by

$$t_i = \frac{D_i \pm \sqrt{D_i^2 - E_i^2 + F_i^2}}{E_i + F_i},\ i = 1,2,3 \tag{2.12}$$

Thus, the inverse kinematics of the spherical parallel manipulators is obtained.

By differentiating Eq. (2.7), the Jacobian matrix can be obtained,

$$\dot{\mathbf{w}}_i \cdot \mathbf{v}_i + \mathbf{w}_i \cdot \dot{\mathbf{v}}_i = 0,\ i = 1,2,3 \tag{2.13}$$

with

$$\dot{\mathbf{w}}_i = \dot{\theta}_i \mathbf{u}_i \times \mathbf{w}_i,\ \dot{\mathbf{v}}_i = \boldsymbol{\omega} \times \mathbf{v}_i \tag{2.14}$$

where $\boldsymbol{\omega} = \begin{bmatrix} \omega_x & \omega_y & \omega_z \end{bmatrix}^{\mathrm{T}}$ is the angular velocity of the mobile platform. Utilizing vector product,

$$\dot{\theta}_i (\mathbf{u}_i \times \mathbf{w}_i) \cdot \mathbf{v}_i = \boldsymbol{\omega} \cdot (\mathbf{w}_i \times \mathbf{v}_i) \tag{2.15}$$

the Jacobian matrix $\mathbf{J}_s$ is obtained as

$$\dot{\boldsymbol{\theta}} = \mathbf{J}_s \boldsymbol{\omega} \tag{2.16}$$

where

$$\mathbf{J}_s = \mathbf{J}_b^{-1} \mathbf{J}_a \tag{2.17}$$

with

$$\begin{cases} \mathbf{J}_a = \begin{bmatrix} \mathbf{w}_1 \times \mathbf{v}_1 & \mathbf{w}_2 \times \mathbf{v}_2 & \mathbf{w}_3 \times \mathbf{v}_3 \end{bmatrix}^{\mathrm{T}} \\ \mathbf{J}_b = \mathrm{diag} \begin{bmatrix} (\mathbf{u}_1 \times \mathbf{w}_1) \cdot \mathbf{v}_1 & (\mathbf{u}_2 \times \mathbf{w}_2) \cdot \mathbf{v}_2 & (\mathbf{u}_3 \times \mathbf{w}_3) \cdot \mathbf{v}_3 \end{bmatrix} \end{cases}$$

2.1.3 Dynamics modeling

Considering that a spherical parallel manipulator is a constrained multi-body system, the dynamics of the spherical parallel manipulators can be formulated by generalizing the Hamilton's principle by means of Lagrange multiplier technique [29, 114], as follows

$$\frac{d}{dt}\left(\frac{\partial \mathbf{L}}{\partial \dot{\mathbf{q}}}\right) - \frac{\partial \mathbf{L}}{\partial \mathbf{q}} + \mathbf{C}_q^{\mathrm{T}} \boldsymbol{\lambda} = \mathbf{Q}_{ex} \tag{2.18}$$

where $\mathbf{q} = \begin{bmatrix} \mathbf{q}_a & \mathbf{q}_e \end{bmatrix}^{\mathrm{T}}$, $\mathbf{q}_a = \begin{bmatrix} \theta_1 & \theta_2 & \theta_3 \end{bmatrix}^{\mathrm{T}}$ is the vector of input joint angles, $\mathbf{q}_e = \begin{bmatrix} \phi & \theta & \sigma \end{bmatrix}^{\mathrm{T}}$ is the vector of the end-effector. $\mathbf{Q}_{ex} = \begin{bmatrix} \boldsymbol{\tau}^{\mathrm{T}} & \mathbf{0} \end{bmatrix}^{\mathrm{T}}$ is the vector of generalized external forces, and vector $\boldsymbol{\tau} = \begin{bmatrix} \tau_1 & \tau_2 & \tau_3 \end{bmatrix}^{\mathrm{T}}$ characterized the actuated torques.

Moreover, $\boldsymbol{\lambda} = \begin{bmatrix} \lambda_1 & \lambda_2 & \lambda_3 \end{bmatrix}^{\mathrm{T}}$ is a vector of Lagrange multipliers. Matrix $\mathbf{C}_q$ is the system's constraint Jacobian, which can be found from Eq. (2.17),

$$\mathbf{C}_q \dot{\mathbf{q}} = \mathbf{0} \tag{2.19}$$

with $\mathbf{C}_q = \begin{bmatrix} \mathbf{J}_b & -\mathbf{J}_a \boldsymbol{\Phi} \end{bmatrix}^{\mathrm{T}}$, where $\boldsymbol{\Phi}$ is the transformation matrix between the angular velocity $\boldsymbol{\omega}$ and angle rates. $\mathbf{L} = \mathbf{T} - \mathbf{V}$ is the Lagrangian function. $\mathbf{T}$ is the kinematic energy of the system, which can be described as

$$\mathbf{T} = \frac{1}{2} \dot{\mathbf{q}}^{\mathrm{T}} \mathbf{M}(\mathbf{q}) \dot{\mathbf{q}} \tag{2.20}$$

where $\mathbf{M}$ is the mass matrix of the system. Thus,

$$\frac{d}{dt}\left(\frac{\partial \mathbf{L}}{\partial \dot{\mathbf{q}}}\right) = \mathbf{M}\ddot{\mathbf{q}} + \dot{\mathbf{M}}\dot{\mathbf{q}} \tag{2.21}$$

and

$$\mathbf{L}_q = \frac{\partial \mathbf{L}}{\partial \mathbf{q}} = \frac{\partial \mathbf{T}}{\partial \mathbf{q}} - \frac{\partial \mathbf{V}}{\partial \mathbf{q}} = \mathbf{T}_q - \mathbf{V}_q \tag{2.22}$$

Therefore, the dynamics of the spherical parallel manipulators can be obtained

$$\begin{bmatrix} \mathbf{M}(\mathbf{q}) & \mathbf{C}_q^T \\ \mathbf{C}_q & \mathbf{0} \end{bmatrix} \begin{bmatrix} \ddot{\mathbf{q}} \\ \boldsymbol{\lambda} \end{bmatrix} = \begin{bmatrix} \boldsymbol{\tau}_\theta - \dot{\mathbf{M}}(\mathbf{q})\dot{\mathbf{q}} + \mathbf{T}_q - \mathbf{V}_q \\ -\dot{\mathbf{C}}_q \dot{\mathbf{q}} \end{bmatrix} \tag{2.23}$$

2.2 Analytical magnetic methods

2.2.1 Review of Maxwell's equations

Maxwell's equations govern the electromagnetic fields between the interactions of charge and current sources, which provides a fundamental of general electromagnetic phenomenons [115]. The differential forms of Maxwell's equations are described as follows

$$\nabla \times \mathbf{H} = \mathbf{J} + \tfrac{\partial \mathbf{D}}{\partial t}, \tag{2.24}$$

$$\nabla \cdot \mathbf{B} = 0, \tag{2.25}$$

$$\nabla \times \mathbf{E} = -\tfrac{\partial \mathbf{B}}{\partial t}, \tag{2.26}$$

$$\nabla \cdot \mathbf{D} = \rho \tag{2.27}$$

where the sources terms, $\mathbf{J}$ and ρ, are the free current density with unit of $(\mathrm{A/m^2})$ and the free charge density with unit of $(\mathrm{C/m^2})$, respectively, and

Table 2.1. Descriptions of fields

Field	Description
H	Magnetic field intensity (A/m)
D	Electric flux density (C/m^2)
B	Magnetic flux density (T)
E	Electric field intensity (V/m)
M	Magnetization (A/m)
P	Polarization (C/m^2)

the fields **H**, **D**, **B** and **E** are defined as listed in Table 2.1. In Eqs. (2.24)-(2.27), all the fields can be functioned as vector-valued equations of space and time,

$$\mathbf{W} = W_x(x,y,z)\hat{\mathbf{x}} + W_y(x,y,z)\hat{\mathbf{y}} + W_z(x,y,z)\hat{\mathbf{z}} \tag{2.28}$$

where **W** can be substituted by the fields **H**, **D**, **B** or **E**. Due to that each field is consisting of three components, the overall equations become a system of 12 unknown field components. By combining the divergence of Eq. (2.24) and the time derivative of Eq. (2.27), the continuity equation is obtained

$$\nabla \cdot \mathbf{J} + \frac{\partial \rho}{\partial t} = 0 \tag{2.29}$$

These two curl Eqs. (2.24) and (2.26) can be applied to obtain the divergence Eqs. (2.25) and (2.27). Additionally, the following constitutive relations are required for completing the mathematical theory,

$$\mathbf{B} = \mu_0(\mathbf{B} + \mathbf{H}) \tag{2.30}$$

$$\mathbf{D} = \epsilon_0 \mathbf{E} + \mathbf{P} \tag{2.31}$$

where the constant μ_0 is the permeability of free space, $\mu_0 = 4\pi \times 10^{-7}\text{Tm/A}$, the constant ϵ_0 is the permittivity of free space, $\epsilon_0 = 8.854 \times 10^{-12}\text{F/A}$, and the fields **M** and **P** are noted in Table 2.1.

In stationary, linear, homogeneous and isotropic media, the constitutive relations in Eqs. (2.30) and (2.31) are reformulated as

$$\mathbf{B} = \mu \mathbf{H} \tag{2.32}$$

$$\mathbf{D} = \epsilon \mathbf{E} \tag{2.33}$$

An additional constitutive law that presents the relation between **J** and **E** is introduced

$$\mathbf{J} = \sigma \mathbf{E} \tag{2.34}$$

where μ and ϵ are the permeability and permittivity of the media, respectively, and σ is the conductivity with the unit of $(\mathrm{A}/\mathrm{V}\cdot\mathrm{m})$. In a nonlinear, inhomogeneous or anisotropic media, Eqs. (2.32)-(2.34) will be modified by replacing the constants with nonlinear terms, $\mu(H)$, $\epsilon(E)$ and $\sigma(E)$.

Maxwell's equations can be alternatively written in integral forms which are applicable for highly symmetrical geometry [116]. By applying Strokes theorem to left-hand side, the curl Eqs. (2.24) and (2.26) are formulated in the surface integral form over an open surface S bounded by a contour C,

$$\oint_C \mathbf{H}d\mathbf{l} = \int_S (\mathbf{J} + \tfrac{\partial \mathbf{D}}{\partial t}) \cdot d\mathbf{s}, \tag{2.35}$$

$$\oint_C \mathbf{E}d\mathbf{l} = -\int_S \tfrac{\partial \mathbf{B}}{\partial t} \cdot d\mathbf{s} \tag{2.36}$$

Equation (2.35) is stated as Ampere's circuital law. It presents that the magnetic field intensity around any closed curve equals the free current flowing through the surface S bounded by the curve C. Equation (2.36) is Faraday's law of electromagnetic induction, which describes that the electromotive force around a closed path is equal to the negative time rate of the increase of the magnetic flux enclosed by the path.

By using the Divergence theorem to the left-hand side, the integration of the divergence Eqs. (2.25) and (2.27) over a volume V with a closed surface S can be obtained as

$$\nabla \cdot \mathbf{B} = 0, \tag{2.37}$$

$$\nabla \cdot \mathbf{D} = \int_V \rho dv \tag{2.38}$$

Equation (2.37) expresses the outward magnetic flux of a magnetic field **B** over a closed surface S is equal to zero, which implies there is no existence of magnetic monopole. Furthermore, Eq. (2.38) is known as Gauss's flux theorem which describes the outward electric flux of the electric field **D** over a closed surface S is equal to the total charge enclosed within the volume V bounded by S.

In summary, the differential and integral forms of Maxwell's equations are reviewed in this section. The Maxwell's equations for the magnetostatic field will be applied to analyze the magnetic field model of permanent magnets.

2.2.2 Magnetic field models for permanent magnets

In this study, the rotor array of the spherical motion generator is constructed by a series of permanent magnets in a certain arrangement. The permanent magnets are selected as the common tile or cylindrical shapes. To investigate the magnetic field of the permanent magnet rotor array, two basic methods, namely, the current model and the charge model, respectively, are used. For example, Fig. 2.3(a) shows a cylindrical permanent magnet with axial parallel magnetization. In the charge model, a permanent magnet is equivalent to a distribution of “magnetic charges” as shown in Fig. 2.3(b). In the current model, the permanent magnet is replicated as a distribution of equivalent current as shown in Fig. 2.3(c). Both the equivalent current and the magnetic charge can be then input into the magnetostatic field equations as a source term, and the field is obtained using standard methods [117]. With regard to the permanent magnets, the derivation of both methods start with the magnetostatic field equations of the Maxwell’s equations for current-free regions,

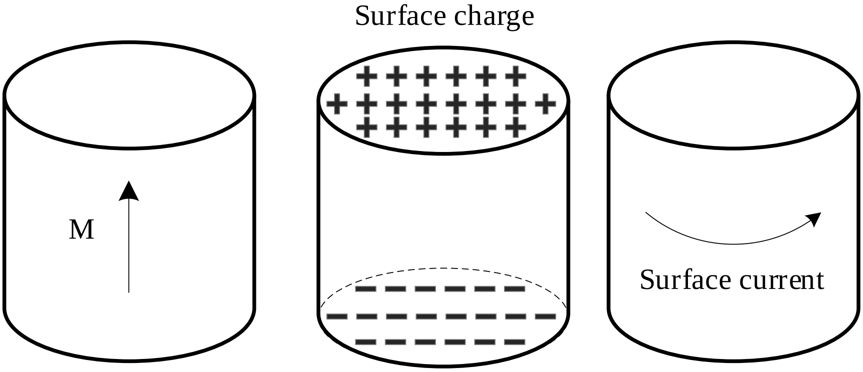

(a) Physical PM (b) Magnetic charge (c) Equivalent current

Figure. 2.3. Analytical magnetic modeling of a permanent magnet

$$\nabla \times \mathbf{H} = \mathbf{0} \tag{2.39}$$

$$\nabla \cdot \mathbf{B} = \mathbf{0} \tag{2.40}$$

The equivalent current model

In the current model [118], the magnetic flux density, **B** in Eq. (2.40) can be formulated as the curl of the vector potential field **A**,

$$\mathbf{B} = \nabla \times \mathbf{A} \tag{2.41}$$

Substituting Eq. (2.41) into Eq. (2.39) and taking into the constitutive relation in Eq. (2.30), this yields

$$\nabla^2 \mathbf{A} - \nabla(\nabla \cdot \mathbf{A}) = -\mu_0 \nabla \times \mathbf{M} \tag{2.42}$$

Considering the Coulomb gauge condition $\nabla \cdot \mathbf{A} = 0$, Eq. (2.42) is simplified,

$$\nabla^2 \mathbf{A} = -\mu_0 (\nabla \times \mathbf{M}) \tag{2.43}$$

Introducing the definition of an equivalent magnetic volume current density, $\mathbf{J}_m = \nabla \times \mathbf{M}$, the potential $\mathbf{A}$ can be obtained as

$$\nabla^2 \mathbf{A} = -\mu_0 \mathbf{J}_m \tag{2.44}$$

By imposing the free-space Green's function,

$$\mathbf{G}(\mathbf{r}, \mathbf{r}') = -\frac{1}{4\pi|\mathbf{r} - \mathbf{r}'|} \tag{2.45}$$

where $\mathbf{r}$ represents the position vector of the observation point $\mathbf{P}$ and $\mathbf{r}'$ is the position vector of the source point $\mathbf{P}'$, Eq. (2.44) can be formulated in integral form

$$\mathbf{A}(\mathbf{r}) = \frac{\mu_0}{4\pi} \int \frac{\mathbf{J}_m(\mathbf{r}')}{|\mathbf{r} - \mathbf{r}'|} dV' \tag{2.46}$$

According to Eq. (2.41), we obtain the magnetic flux density $\mathbf{B}$

$$\mathbf{B}(\mathbf{r}) = \frac{\mu_0}{4\pi} \int \frac{\mathbf{J}_m(\mathbf{r}') \times (\mathbf{r} - \mathbf{r}')}{|\mathbf{r} - \mathbf{r}'|^3} dV' \tag{2.47}$$

If the magnetization $\mathbf{M}$ is confined to a volume V, and falls abruptly to zero outside of V, Eqs. (2.46) and (2.47) become

$$\mathbf{A}(\mathbf{r}) = \frac{\mu_0}{4\pi} \int_V \frac{\mathbf{J}_m(\mathbf{r}')}{|\mathbf{r} - \mathbf{r}'|} dV' + \frac{\mu_0}{4\pi} \oint_S \frac{\mathbf{j}_m(\mathbf{r}')}{|\mathbf{r} - \mathbf{r}'|} ds' \tag{2.48}$$

and

$$\mathbf{B}(\mathbf{r}) = \frac{\mu_0}{4\pi} \int_V \frac{\mathbf{J}_m(\mathbf{r}') \times (\mathbf{r} - \mathbf{r}')}{|\mathbf{r} - \mathbf{r}'|^3} dV' + \frac{\mu_0}{4\pi} \oint_s \frac{\mathbf{j}_m(\mathbf{r}') \times (\mathbf{r} - \mathbf{r}')}{|\mathbf{r} - \mathbf{r}'|^3} ds' \tag{2.49}$$

respectively, where S is the surface of the magnet. $\mathbf{J}_m$ and $\mathbf{j}_m$ are equivalent volume and surface current densities, respectively, which are defined as

$$\begin{aligned} \mathbf{J}_m &= \nabla' \times \mathbf{M} \quad (\mathrm{A/m^2}) \\ \mathbf{j}_m &= \mathbf{M} \times \hat{\mathbf{d}}' \quad\quad (\mathrm{A/m}) \end{aligned} \tag{2.50}$$

where $\hat{\mathbf{d}}'$ is unit normal vector of the permanent magnet surfaces.

The charge model

In the charge model [64, 119], the magnetic field strength, $\mathbf{H}$ in Eq. (2.39) can be expressed as the divergence of the magnetic scalar potential φ

$$\mathbf{H} = -\nabla \cdot \varphi \tag{2.51}$$

Substituting Eqs. (2.51) and (2.30) into Eq. (2.40), this yields

$$\nabla^2 \cdot \varphi = \nabla \cdot \mathbf{M} \tag{2.52}$$

By using the free-space Green's function, Eq. (2.52) can be formulated in integral form in the absence of boundary surfaces,

$$\varphi(\mathbf{r}) = -\frac{1}{4\pi}\int \frac{\nabla \cdot \mathbf{M}}{|\mathbf{r}-\mathbf{r}'|}dV' \tag{2.53}$$

If the magnetization $\mathbf{M}$ is confined to a volume V (of permeability μ_0), and falls abruptly to zero outside of V, Eq. (2.53) reduces to

$$\varphi(\mathbf{r}) = \frac{1}{4\pi}\int_V \frac{\mathbf{J}_m(\mathbf{r}')}{|\mathbf{r}-\mathbf{r}'|}dV' + \frac{1}{4\pi}\oint_s \frac{\mathbf{j}_m(\mathbf{r}')}{|\mathbf{r}-\mathbf{r}'|}ds' \tag{2.54}$$

where S is the surface of the magnet. $\mathbf{J}_m$ and $\mathbf{j}_m$ are equivalent volume and surface current densities, respectively, which are defined as

$$\begin{aligned} \mathbf{J}_m &= -\nabla' \cdot \mathbf{M} \quad (\mathrm{A/m^2}) \\ \mathbf{j}_m &= \mathbf{M} \cdot \hat{\mathbf{d}} \quad (\mathrm{A/m}) \end{aligned} \tag{2.55}$$

where $\hat{\mathbf{d}}$ is the unit surface normals. The permanent magnet is in free space with the condition, $\mathbf{B} = \mu_0\mathbf{H}$. From Eqs. (2.51) and (2.54), we have

$$\mathbf{B}(\mathbf{r}) = \frac{\mu_0}{4\pi}\int_V \frac{\mathbf{J}_m(\mathbf{r}')(\mathbf{r}-\mathbf{r}')}{|\mathbf{r}-\mathbf{r}'|^3}dV' + \frac{\mu_0}{4\pi}\oint_s \frac{\mathbf{j}_m(\mathbf{r}')(\mathbf{r}-\mathbf{r}')}{|\mathbf{r}-\mathbf{r}'|^3}ds' \tag{2.56}$$

2.3 Electromagnetic force modeling

The actuation of the spherical motion generator is implemented by the electromagnetic torques generated by the interaction between the permanent magnet array and the stator coils. In this chapter, the electromagnetic torque model will be studied [64, 117].

For a particle of charge q moving through an external magnetic field $\mathbf{B}$, it will experience a Lorentz force which is formulated as

$$\mathbf{F} = q(\mathbf{u} \times \mathbf{B}_{\mathrm{ext}}) \tag{2.57}$$

Extending to the case of currents, a volume current density $\mathbf{J}$ is defined that ρ_u charges per unit volume move with the velocity $\mathbf{u}$, $\mathbf{J} = \rho_u\mathbf{u}$. The force density $\mathbf{f}$ which states the force per unit volume can be described as

$$\mathbf{f} = \mathbf{J} \times \mathbf{B}_{\mathrm{ext}}, (\mathrm{N/m^3}) \tag{2.58}$$

Therefore, the total force generated on a conductor with current density $\mathbf{J}$ can be obtained by the integration of $\mathbf{f}$ over the volume of conductor,

$$\mathbf{F} = \int_V \mathbf{f} dv \tag{2.59}$$

Moreover, the torque is determined by

$$\mathbf{T} = \int_V \mathbf{r} \times \mathbf{f} dv \tag{2.60}$$

where **r** is the vector from a point at which the torque is required to be computed.

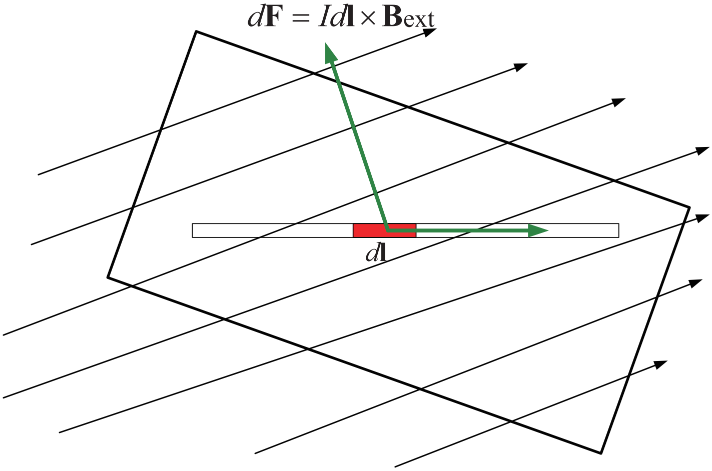

Figure. 2.4. Lorentz force law

Appling Eqs. (2.59) and (2.60) to the coils with current I, $\mathbf{J}dv$ is equivalent to $Id\mathbf{l}$ as shown in Fig. 2.4. Thus, the equations reduced to

$$\mathbf{F} = I \int d\mathbf{l} \times \mathbf{B}_{\text{ext}} \tag{2.61}$$

and

$$\mathbf{T} = I \int \mathbf{r} \times (d\mathbf{l} \times \mathbf{B}_{\text{ext}}) \tag{2.62}$$

where $\mathbf{B}_{\text{ext}}$ is the calculated magnetic field distribution from the analytical current or charge model.

2.4 Example

An example of the integrated modeling of the SMG is included. A multi-layer SMG is taken for modeling and simulation [119], as shown in Fig. 2.5(a). The three coaxial input shafts are attached with permanent magnet arrays, and three layers' stator coils are evenly distributed around the rotors with the total number of stator coils, $N_c = 18$. The actuation of each input shaft is implemented separately by the electromagnetic force generated between

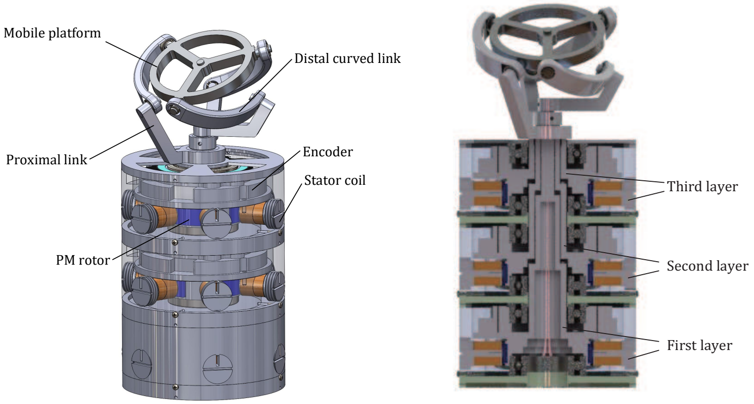

(a) Conceptual design (b) Cross-section view

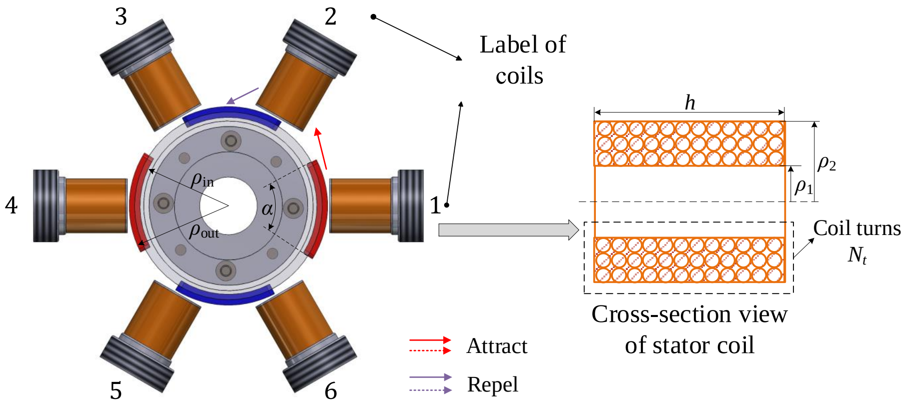

(c) Actuating principle

Figure. 2.5. Spherical motion generators with multi-layer actuation its own attached rotor array and the stator coils located on the same layer as displayed in Fig. 2.5(b). Compared with spherical actuators, the rotor is divided into three separate parts, which is easy for further control.

Figure 2.5(c) shows each layer's electromagnetic actuating principle. The permanent magnet rotor array is consisting of four tile-shaped permanent poles that are radial-symmetric distributed on cylindrical iron ring. The stator coils are constructed by six stator air-core windings that are mounted on a cylindrical stator shell. The rotational motion of the shaft is achieved by the repelling and attracting forces between the rotor and stator. This spherical motion generator is also can be divided into two types of motion modes, the spinning motion and the 3D general motion. In the spinning motion, all the proximal links are driven by equal electromagnetic forces continuously, and then the mobile platform will spin about its own axis. In the general spherical motion, the proximal links are required to be actuated with different torques through varying the currents of stator coils.

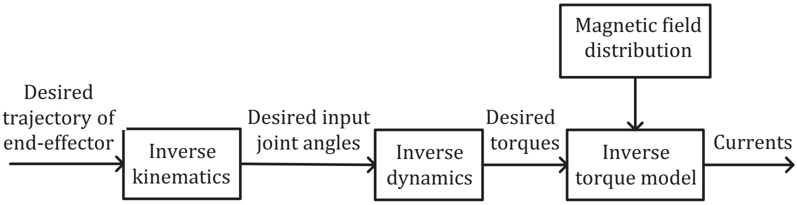

Figure. 2.6. Integrated modeling system

The analytical models of the kinematics, dynamics and the torque are implemented in Matlab/Simulink. The integrated modeling system is shown as Fig. 2.6. The parameters of SMG are listed in Table 2.2. The mass and inertia properties are given in Table 2.3.

2.4.1 Kinematic and dynamic simulation

The trajectory of the mobile platform in terms of X-Y-Z Euler angles is designed as

$$\phi = \frac{\pi}{36} \sin \pi t, \theta = 0.1t^2, \sigma = \frac{-54.7\pi}{180} + \frac{5\pi}{360} t^3 \tag{2.63}$$

which is a spatial trajectory on a sphere as shown in Fig. 2.7. The results from the kinematic and dynamic models are obtained. The joint angles and angular velocities are shown in Figs. 2.8 and 2.9, respectively. The solved joint torques are depicted in 2.10.

Table 2.2. Parameters of the SMG

Parameter	Value
Arc angle of proximal curve links α_1	$\frac{\pi}{2}$ rad
Arc angle of distal curve links α_2	$\frac{\pi}{2}$ rad
Geometry of mobile platform β	$\frac{\pi}{3}$ rad
Radius of proximal curve links R_1	50 mm
Radius of distal curve links R_2	42.5 mm
Inner radius of PM ρ_{in}	24.5 mm
Outer radius of PM ρ_{out}	27.5 mm
Tilt angle of PM pole α	$\frac{\pi}{3}$ rad
Inner radius of stator coil ρ_1	2 mm
Outer radius of stator coil ρ_2	9 mm
height radius of stator coil h	20 mm
Number of coils N_c	18/3 layers
Number of coil turns N_t	480

Table 2.3. Mass and inertia properties of the SMG

Parameter	Mass (kg)	Inertia property $[I_{xx}\ I_{yy}\ I_{zz}]$ (10^{-4}kg m^2)
Mobile platform	0.2972	[2.8511 2.8511 2.8511]
Distal links	0.181	[6.0480 0.0749 3.1665]
Proximal links	0.47	[0.1727 0.1796 0.2682]

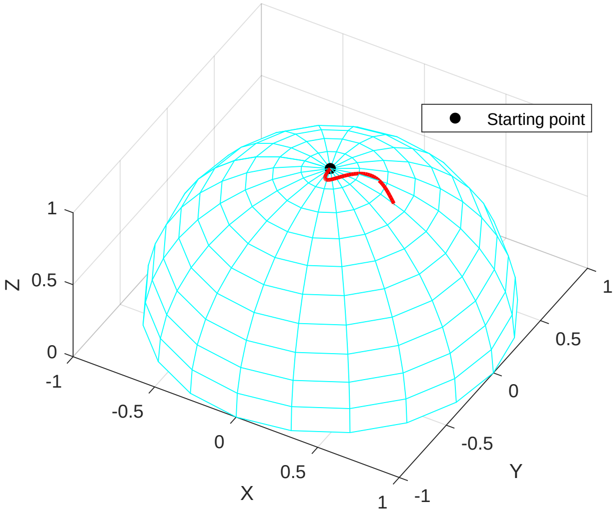

(a)

Figure. 2.7. Desired trajectory

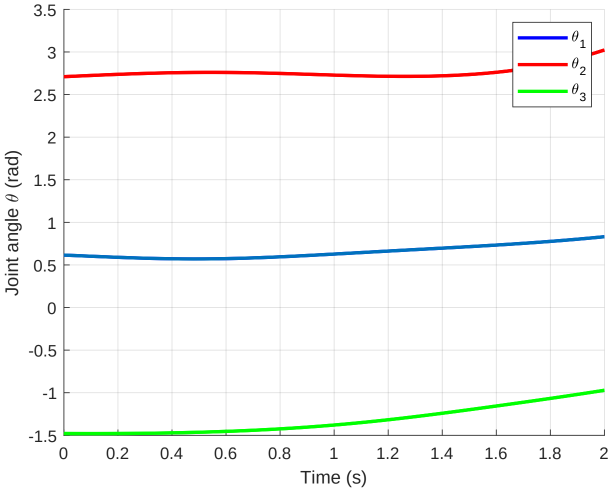

Figure. 2.8. Desired joint angles

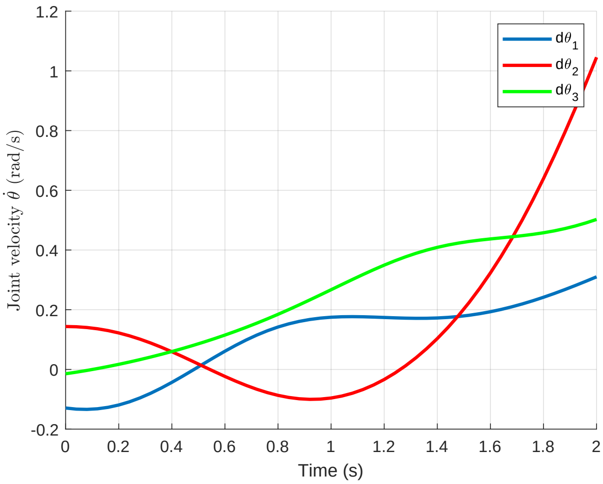

Figure. 2.9. Desired joint velocities

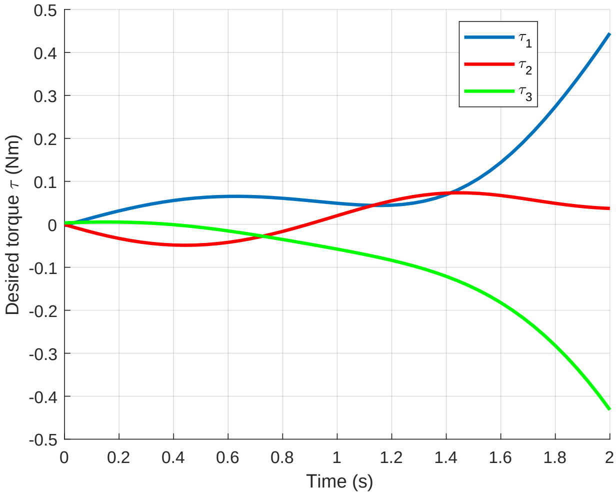

Figure. 2.10. Desired torques

2.4.2 Torque simulation

The desired torques are the outputs of the inverse dynamic model. The input joint angles are obtained from the inverse kinematic model. By using the analytical magnetic field and torque models, the required currents are obtained. Only the currents of the stator coils in the first layer are displayed in Fig. 2.11.

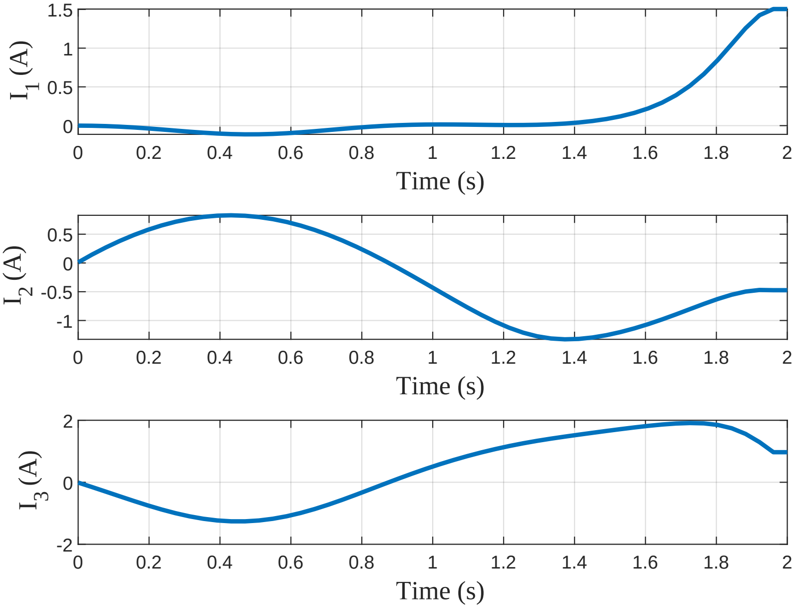

Figure. 2.11. Desired currents of the stator coils in the first layer

Above all, the systematic modeling of the electromagnetic driven spherical motion generator is investigated. To generate a spherical trajectory at the end-effector of the SMG, inverse kinematics and dynamics are utilized to calculate the input joint angles and the actuated torques, and the results are then applied in the analytical magnetic and torque models to solve the required input currents that will be used for further actuating the prototype of the spherical motion generator system. The example of the multi-layer SMG simulation evaluates the overall analytical models finally.

2.5 Summary

This chapter described the analytical methods to investigate the modeling of the electromagnetic driven SMG. The kinematic model of spherical parallel manipulators is analyzed and the Lagrange multiplier method is used for the dynamic modeling. The Maxwell equations that are the fundamental of the magnetic field modeling are reviewed and analytical torque methods are introduced. To evaluate the analytical methods that constitute the integrated modeling system, an example of the electromagnetic driven SMG with multilayer actuations is proposed.

Chapter 3

Paper I

Integrated design, modeling and analysis of a novel spherical motion generator driven by electromagnetic principle

Xuerong Li, Jingmeng Liu, Weihai Chen and Shaoping Bai

The paper has been published in the
Robotics and Autonomous Systems Vol. 106(2018), pp. 69–81, 2018.

Robotics and Autonomous Systems 106 (2018) 69–81

Contents lists available at ScienceDirect

Robotics and Autonomous Systems

journal homepage: www.elsevier.com/locate/robot

Integrated design, modeling and analysis of a novel spherical motion generator driven by electromagnetic principle

Xuerong Li [a,b], Jingmeng Liu [b], Weihai Chen [b], Shaoping Bai [a,*]

[a] Department of Materials and Production, Aalborg University, 9220 Aalborg, Denmark
[b] School of Automation Science and Electrical Engineering, Beihang University, 100191 Beijing, China

HIGHLIGHTS

- A novel design of a highly integrated spherical motion generator (SMG) is presented.
- A compact design integrates the parallel mechanism with electromagnetics actuator.
- Analytical models, including kinematics, dynamics, and torque models, are developed.
- A task-space trajectory tracking control is proposed for the SMG.

ARTICLE INFO

Article history:
Received 11 January 2018
Received in revised form 21 March 2018
Accepted 16 April 2018
Available online 2 May 2018

Keywords:
Spherical motion generator
Permanent magnet spherical motor
Spherical parallel manipulator
Torque model
Trajectory tracking control

ABSTRACT

Spherical motion generators are increasingly needed for constructing robots, manipulators and pointing devices. This paper presents a novel design of spherical motion generator built on the basis of a spherical parallel manipulator. The new motion generator integrates the electromagnetic actuator with the co-axial 3-RRR spherical parallel manipulator, thus leads to a more compact and light-weight structure with the advantages of no backlash, high stiffness and low inertia. In this paper, the inverse kinematics and dynamics of the spherical parallel manipulator are described. The analytical torque model of this spherical motion generator is developed and compared with the numerical finite element method by Ansoft Maxwell. The models allow for comprehensive design analysis and parameter optimization. It is shown that the proposed SMG has better performance with larger workspace and output torques than the existing permanent magnet spherical motors with comparable dimensions. Upon the developed model, a motion control method is developed for tracking trajectory to demonstrate the application of the analytical model.

1. Introduction

A multi-degree-of-freedom spherical motion generator (SMG) is a device of multi-degrees of pure rotations about their center of rotation. SMGs can be applied in areas such as machine tools, solar panels, orientating devices [1,2] and medical instruments [3].

SMGs can be implemented by two major approaches, namely, spherical motors or spherical manipulators of serial and parallel configurations. Spherical motors include the spherical ultrasonic motors [4], spherical induction motors, and permanent magnet spherical motors. Spherical ultrasonic motors adopted the ultrasonic vibration to drive the spherical motor. While the friction drive principle leads to the advantages of the high responsiveness [5], it influences the durability and the positioning accuracy. A small spherical stepping motor with two degrees of freedom was reported in [6], for which the torque output is limited. A spherical induction motor was optimized to obtain good performance in terms of the torque and energetic efficiency for applications in omnimobile robot [7]. SMGs in the form of permanent magnet spherical motor (PMSM) are reported in [8,9]. Fig. 1 illustrates a 3-DOF PMSM which mainly consists of a rotor constructed by spherical permanent magnet array and a set of multi-layer stator windings distributed in a spherical shape. PMSM offers advantages of compact structure, high energy density and rapid response. However, the maximum tilting angle of the PMSM is small, which is ±15° [10], due to the limitation of its mechanical structure. In addition, the spherical motors are suffered from relatively heavy mass and large size due to the use of the permanent magnet array and the supporting structure [11]. The real-time control methods for the PMSM are also a challenging problem because of its nonlinearities and uncertainties in the dynamic model.

SMG can also be implemented by spherical mechanisms actuated by ordinary motors, either in serial or parallel configurations.

---

* Corresponding author.
E-mail address: shb@mp.aau.dk (S. Bai).

https://doi.org/10.1016/j.robot.2018.04.006
0921-8890/

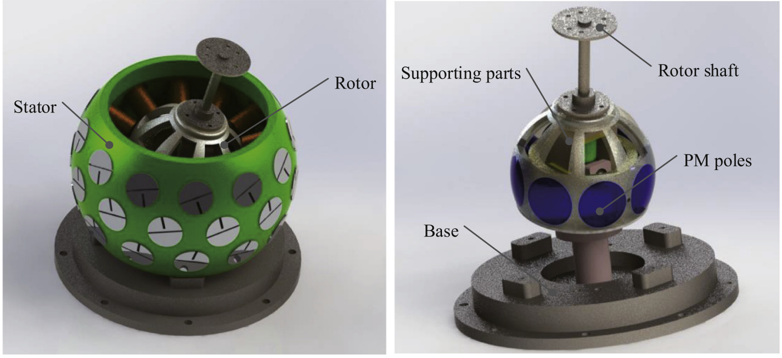

Fig. 1. Permanent magnet spherical motor [12].

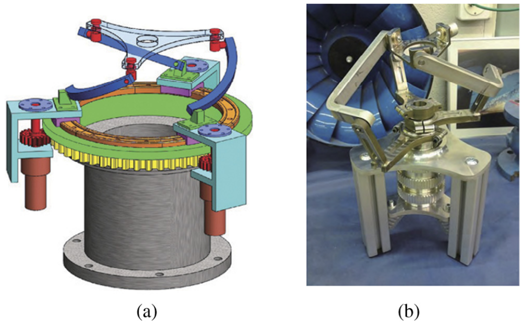

Fig. 2. Two spherical parallel manipulators with co-axial input shafts, (a) a design with virtual co-axial shaft, namely, a circular ring with three slide units [16], (b) a design with a common shaft for three revolute joints [17].

A SMG designed with serial links was reported in [13]. A two-DOF gearless pich-roll wrist was designed utilizing differential motion principle [14]. There are a number of SMGs designed as spherical parallel manipulators. Compared with the serial ones, spherical parallel manipulators (SPMs) offer greater rigidity, better accuracy, larger load capacity and reduction in mass. A common type of SPMs studied is the 3-RRR (Revolute–Revolute–Revolute joint) spherical parallel manipulator, exampled by the Agile Eye [2]. A 3-RRR SPM which can achieve unlimited rolling rotation was reported in [15]. The unlimited rolling rotation is feasible due to its design of co-axis inputs. Two embodiments of the co-axis input SPM can be found in [16,17], as shown in Fig. 2. Other types of SPMs include three PRS (Prismatic–Revolute–Spherical joint) kinematic chains in parallel [18] and the spherical double-triangle (DT) parallel manipulator [19], among others.

Compared with the spherical motors such as PMSMs, the 3-RRR SPM has a more light-weight mechanical structure and is more flexible in configuration design. However, the SPMs are generally driven by separated motors, which leads to complex transition systems and additional heavy structures. Moreover, hysteresis error exists objectively due to the gear clearance. As time goes on, the hysteresis error and noise will increase. As a result, precision will become low. In addition to the inertia of gears, the nonlinear friction and elastic deformation will also influence the dynamic performance.

This work proposes a new design of an integrated spherical motion generator that integrates the spherical parallel manipulator with electromagnetic principle of the permanent magnet spherical motor. The new design leads to a more compact and light-weight structure with the advantages of no backlash, high stiffness and low inertia.

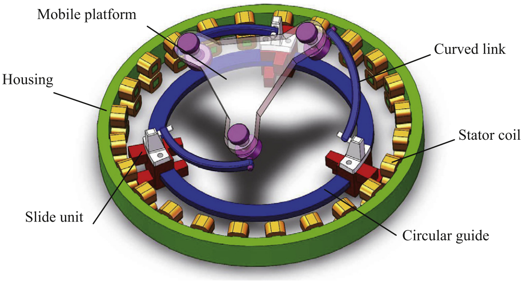

Fig. 3. A conceptual design of SMG.

The objective of this work is to develop the mechanical and electromagnetic models analytically for the newly designed SMG. This paper is organized as follows. Section 2 describes the conceptual design and working principle of the spherical motion generator. Section 3 depicts inverse kinematics and dynamics of the SMG. The analytical torque model is developed in Section 4, and the inverse torque model and current optimization is demonstrated. Section 5 introduces the trajectory tracking control, utilizing the developed dynamics and torque models. Simulation results are presented in 6. An embodiment is described in Section 7. Finally, the work is concluded in Section 8.

2. Conceptual design of integrated electromagnetic driven SMG

The integrated SMG is shown in Fig. 3, which is built on a conceptual design reported in [15]. The SMG consists of three curved links connected to a mobile platform which outputs spherical motions. The slide units in the SMG are permanent magnets (PMs). The stator coils are mounted on the housing. Under the electromagnetic forces, the permanent magnets can slide along the circular guide. Their motions are coupled to the mobile platform by curved links, thus generating 3-DOF spherical rotations. In this design, double-layer stator coils are distributed equally on the cylindrical housing. Accordingly, every slide unit consists of two PM poles in two layers, namely, a lower and an upper layer as shown in Fig. 4. This guarantees a smooth motion with a limited number of stators.

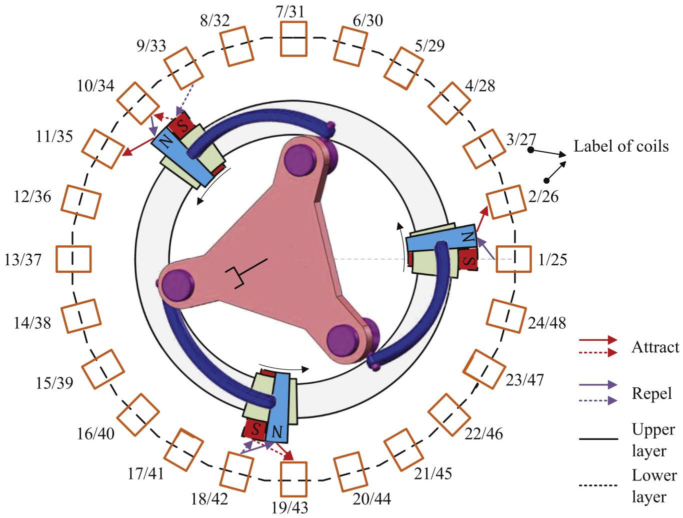

Fig. 4. Working principle of the SMG.

Through varying the current inputs of the double-layer stator coils, every single slide unit can rotate independently around the circle. 3-DOF rotational motion within the workspace will be produced in the end-effector due to slide units in different positions.

The SMG can operate with two motion modes, namely, a pure-spinning mode and a general 3D motion mode. In the pure-spinning mode, these three slide units are actuated with equal torques continuously, thus the end-effector can spin about its own axis. In the 3D motion mode, the slide units are driven by different torques separately and relative motions between the slide units will produce the 3D motion at the mobile platform.

Compared with PMSMs and SPMs, the new design brings some new features as follows

- The new design integrates the parallel mechanism and the motor in a more compact and flexible structure.
- The rotor structure is much simpler and more light-weight. The miniaturization of the manipulator can be realized.
- The SMG inherits the kinematic properties of 3-RRR SPM and thus has a larger workspace than the PMSMs.
- The non-contact electromagnetic driven principle eliminates the use of motors and gears, and leads to no backlash and less mechanical wear.
- As the SMG requires only two layers' stators and three pairs of permanent magnets, the material use is significantly reduced, compared with the PMSMs.

3. SMG kinematics and dynamics

3.1. Inverse kinematics

The kinematics of the SMG is essentially identical to a co-axial 3-RRR SPM. A 3-RRR SPM is shown in Fig. 5. The SPM consists of three revolute joints, whose axes are denoted by unit vectors $\mathbf{u}_i, \mathbf{v}_i$ and $\mathbf{w}_i$, $i = 1, 2, 3$. All links that are connected to the base platform and to the mobile platform have identical dimensions of α_1 and α_2, respectively. Moreover, β defines the geometry of the regular pyramid of the mobile platform and γ defines the geometry of the regular pyramid of base platform. The SMG kinematics pertains to a special case of general SPMs for which $\gamma = 0$. For given locations of the end-effector, the joint variables are found by inverse kinematics. The method presented in [15] was adopted for this purpose. The solution of the inverse kinematics can be reviewed in the Appendix.

3.2. Singularity analysis and workspace

The singularities encountered in spherical parallel manipulators can be classified into three types [20]. The manipulator's velocity equation is obtained as

$$\mathbf{A_1}\boldsymbol{\omega} = \mathbf{A_2}\dot{\boldsymbol{\theta}} \tag{1}$$

where $\boldsymbol{\omega}$ and $\dot{\boldsymbol{\theta}}$ are the angular velocity of the mobile platform and the velocity of input joints. Moreover, $\mathbf{A_1}$ and $\mathbf{A_2}$ are

$$\mathbf{A}_1 = \begin{bmatrix} (\mathbf{w}_1 \times \mathbf{v}_1)^T \\ (\mathbf{w}_2 \times \mathbf{v}_2)^T \\ (\mathbf{w}_3 \times \mathbf{v}_3)^T \end{bmatrix} \tag{2}$$

$$\mathbf{A_2} = diag\left[(\mathbf{u}_1 \times \mathbf{w}_1) \cdot \mathbf{v}_1 \quad (\mathbf{u}_2 \times \mathbf{w}_2) \cdot \mathbf{v}_2 \quad (\mathbf{u}_3 \times \mathbf{w}_3) \cdot \mathbf{v}_3\right] \tag{3}$$

Singularities occur in configurations where either $\mathbf{A_1}$ or $\mathbf{A_2}$ is singular.

The first kind of singularity is known to lie on the boundary of the workspace and appears whenever $\det(\mathbf{A_2}) = 0$. The conditions of the occurrence of singularity satisfy the expression

$$(\mathbf{u}_i \times \mathbf{w}_i) \cdot \mathbf{v}_i = 0, \quad i = 1, 2, 3 \tag{4}$$

which states that the vectors $\mathbf{u}_i$, $\mathbf{w}_i$, and $\mathbf{v}_i$ are coplanar. When γ equals to zero, the unit vector $\mathbf{u}_i$ is coincident with z-axis which is perpendicular to the base platform. As a result, the plane $\mathbf{OA_iB_i}$ determined by $\mathbf{u}_i$ and $\mathbf{w}_i$ is orthogonal to xy-plane as shown in Fig. 6. In terms of the condition of the first-type singularity, when the plane $\mathbf{OB_iC_i}$ formed from vectors $\mathbf{w}_i$ and $\mathbf{v}_i$ is also orthogonal to xy-plane, the first type of singularity occurs.

The second kind of singularity occurs when $\det(\mathbf{A_1}) = 0$. By definition, vector $\mathbf{w}_i$ is not coincident with vector $\mathbf{v}_i$, the condition will be satisfied when the three vectors $(\mathbf{w}_i \times \mathbf{v}_i,\ i = 1, 2, 3)$ are coplanar. In this work, the parameters are designed as $\alpha_1 = 90°, \alpha_2 = 90°$ and $\beta = 60°$. Since $\mathbf{w}_1$, $\mathbf{w}_2$ and $\mathbf{w}_3$ are coplanar

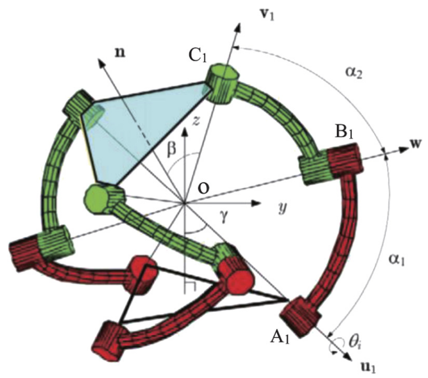

Fig. 5. Kinematic model of SPM.

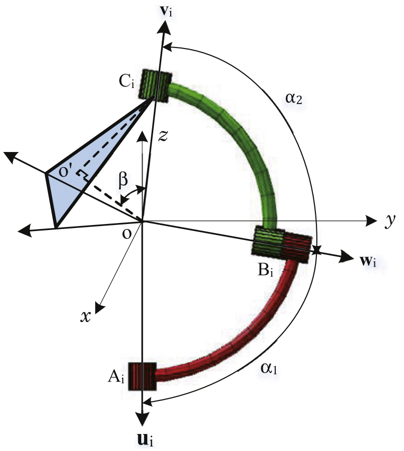

Fig. 6. Singularity analysis of SMG.

at xy-plane with $\alpha_1 = 90°$, the condition can be analyzed in two cases. (1) The three planes defined by pairs of vectors $(\mathbf{w}_i, \mathbf{v}_i)$, $i = 1, 2, 3$, respectively, are identical, that is, $\mathbf{v}_1$, $\mathbf{v}_2$ and $\mathbf{v}_3$ are coplanar. Nevertheless, the case would not occur under the condition of $\beta = 60°$. (2) The three planes intersect at a common shaft. If $\alpha_2 + \beta = 90°$ and the three links, $\mathbf{A_iB_i}$ $(i = 1, 2, 3)$, distribute uniformly along z-axis, all three links, $\mathbf{B_iC_i}$ $(i = 1, 2, 3)$, will be normal to xy-plane simultaneously. Consequently, three planes intersect at z-axis. However, for the set of SMG having $\alpha_2 + \beta = 150°$ in this work, the workspace of SMG is free of the second type of singularities.

The third kind of singularity occurs when both matrices $\mathbf{A_1}$ and $\mathbf{A_2}$ are singular simultaneously. This type of singularity is associated with architecture parameters. As stated above, with parameters selected for this design, the second type of singularities is avoided, so does the third type of singularities.

As the first type of singularity appears at the boundary of the workspace, the workspace of SMG can be obtained by combining all the singularity surfaces of individual links. When the plane of the link connected to the mobile platform is perpendicular to xy-plane, the first-type singularity appears. In addition, with the condition $\alpha_1 = \alpha_2 = 90°$, the vector $\mathbf{v_i}$ is parallel with z-axis, then the end-effector of SMG reaches its maximum tilting angle 60° which determined by β as shown in Fig. 6. As the proposed design is free of the second-type singularity and allows an unlimited rotation motion, the singularity-free workspace of the SMG is a pointing cone of 120° opening with 360° full rotation. Compared with the PMSMs whose maximum tilting angle is ±18° [21], the SMG increases the workspace with the maximum tilting angle reaching to ±60°.

3.3. Inverse dynamics

According to Lagrange equation, the dynamic equation of an open-chain SPM can be expressed as

$$\mathbf{M}(\mathbf{q})\ddot{\mathbf{q}} + \mathbf{N}(\mathbf{q}, \dot{\mathbf{q}})\dot{\mathbf{q}} + \mathbf{G}(\mathbf{q}) = \boldsymbol{\tau} \tag{5}$$

where $\mathbf{q} = \begin{bmatrix} \mathbf{q_a}^T & \mathbf{q_e}^T \end{bmatrix}^T$ is the generalized coordinates of the manipulator, $\mathbf{q_a} = \begin{bmatrix} \theta_1 & \theta_2 & \theta_3 \end{bmatrix}^T$ is the vector of actuated joint angles, and $\mathbf{q_e} = \begin{bmatrix} \phi & \theta & \sigma \end{bmatrix}^T$ is the vector of X–Y–Z Euler angles of the mobile platform. $\mathbf{M}(\mathbf{q})$ is the inertial matrix; $\mathbf{N}(\mathbf{q}, \dot{\mathbf{q}})$ is the Coriolis and centrifugal matrix; $\mathbf{G}(\mathbf{q})$ includes gravity terms and other forces which act at the joints; $\boldsymbol{\tau} = \begin{bmatrix} \boldsymbol{\tau}_a{}^T & \mathbf{0_3} \end{bmatrix}^T$ is the vector of external torques and the vector $\boldsymbol{\tau}_a = \begin{bmatrix} \tau_1 & \tau_2 & \tau_3 \end{bmatrix}^T$ characterizes the actuator torques.

The closed-chain system can be viewed as the open-chain system with the loop constraints. The kinematic constraints are considered independent of time and the kinematic constraint matrix $\mathbf{C}(\mathbf{q})$ is expressed as

$$\mathbf{C}(\mathbf{q}) = \begin{bmatrix} \mathbf{A_2} & -\mathbf{A_1}\boldsymbol{\Phi} \end{bmatrix} \tag{6}$$

where $\boldsymbol{\Phi}$ is the transformation matrix between the angular velocity and angle rates. The relation between the angle rates of the actuated joints and the mobile platform can be written as

$$\begin{aligned} \dot{\mathbf{q}}_{\mathbf{a}} &= \frac{\partial \mathbf{q_a}}{\partial \mathbf{q_e}} = \mathbf{S}\dot{\mathbf{q}}_{\mathbf{e}} \\ \dot{\mathbf{q}} &= \frac{\partial \mathbf{q}}{\partial \mathbf{q_e}} = \mathbf{W}\dot{\mathbf{q}}_{\mathbf{e}} \end{aligned} \tag{7}$$

where $\mathbf{S} = \mathbf{A_2}^{-1}\mathbf{A_1}\boldsymbol{\Phi}$ and $\mathbf{W} = \begin{bmatrix} \mathbf{S}^T & \mathbf{E} \end{bmatrix}^T$, $\mathbf{E}$ is the 3 × 3 identical matrix.

The actuated torque $\boldsymbol{\tau}_a$ of the closed-chain system required to generate the same motion can be calculated by

$$\mathbf{W}^T\boldsymbol{\tau} = \mathbf{S}^T\boldsymbol{\tau}_a \tag{8}$$

Substituting Eq. (5) into Eq. (8) yields

$$\mathbf{W}^T(\mathbf{M}(\mathbf{q})\ddot{\mathbf{q}} + \mathbf{N}(\mathbf{q}, \dot{\mathbf{q}})\dot{\mathbf{q}} + \mathbf{G}(\mathbf{q})) = \mathbf{S}^T\boldsymbol{\tau}_a \tag{9}$$

Making use of the kinematic constraints

$$\begin{aligned} \dot{\mathbf{q}} &= \mathbf{W}\dot{\mathbf{q}}_{\mathbf{e}} \\ \ddot{\mathbf{q}} &= \dot{\mathbf{W}}\dot{\mathbf{q}}_e + \mathbf{W}\ddot{\mathbf{q}}_e \end{aligned} \tag{10}$$

the dynamic equation of an actuated closed-chain mechanism in task space is obtained as follows:

$$\mathbf{M}_1\ddot{\mathbf{q}}_e + \mathbf{N}_1\dot{\mathbf{q}}_e + \mathbf{G}_1 = \mathbf{S}^T\boldsymbol{\tau}_a \tag{11}$$

where

$$\begin{aligned} \mathbf{M}_1 &= \mathbf{W}^T\mathbf{M}\mathbf{W} \\ \mathbf{N}_1 &= \mathbf{W}^T\mathbf{M}\dot{\mathbf{W}} + \mathbf{W}^T\mathbf{N}\mathbf{W} \\ \mathbf{G}_1 &= \mathbf{W}^T\mathbf{G} \end{aligned}$$

The inverse dynamic model of SPM can be rewritten as

$$\boldsymbol{\tau}_a = (\mathbf{S}^T)^+(\mathbf{M}_1\ddot{\mathbf{q}}_e + \mathbf{N}_1\dot{\mathbf{q}}_e + \mathbf{G}_1) \tag{12}$$

where $(\mathbf{S}^T)^+ = \mathbf{S}(\mathbf{S^TS})^{-\mathbf{1}}$ and satisfies $\mathbf{S}(\mathbf{S}^T)^+ = \mathbf{E}$.

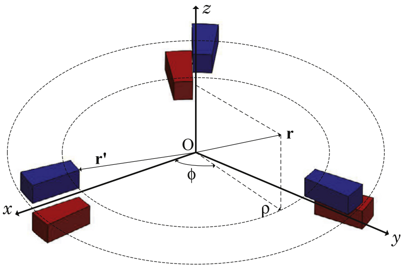

Fig. 7. Rotor structure in the cylindrical coordinate system.

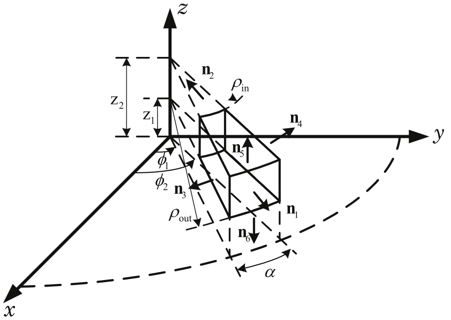

Fig. 8. Permanent magnet (PM) structure.

4. Inverse torque model

The inverse torque model of the SMG is to establish the relation between the current outputs of the stator coils and the required torque calculated in Eq. (12). The driving torque is based on the solution to the magnetic field distribution of PM slide units. When the magnetic flux density **B** produced by the slide units is known, the torque can be obtained analytically according to Lorentz force law. The magnetic charge model developed in [22] is adopted first to analyze the spatial distribution of the magnetic flux density.

4.1. 3D distribution of magnetic flux density

In this model, a permanent magnet which composes the rotor slide unit in the SPM structure is considered as an equivalent spatial distribution of "magnetic charges" that are used as a source term in the magnetostatic field equations [23]. The complete solution for the magnetic flux density of the rotor slide units can be obtained by the superposition of the magnetic field distribution produced by every single permanent magnet. The permanent magnets distribution of the rotor slider units in the cylindrical coordinate system is shown in Fig. 7, where $\mathbf{r} = \rho\mathbf{e}_\rho + \phi\mathbf{e}_\phi + z\mathbf{e}_z$ is the position vector of an observation point, $\mathbf{r}'$ is the position vector to each magnetic source point on the magnetic geometry surfaces.

According to the charge model [22], the magnetic scalar potential φ_{m} of one single permanent magnet can be formulated as

$$\varphi_m(\mathbf{r}) = \frac{1}{4\pi}\int_V \frac{\rho_m}{|\mathbf{r}-\mathbf{r}'|}dv' + \frac{1}{4\pi}\oint_S \frac{\sigma_m}{|\mathbf{r}-\mathbf{r}'|}ds' \tag{13}$$

where S is the surface of that bound V. Moreover, ρ_m and σ_m are magnetic volume and surface charge density, respectively, which are defined as

$$\begin{aligned} \rho_m &= -\nabla\cdot\mathbf{M} \quad (\mathrm{A/m^2}) \\ \sigma_m &= \mathbf{M}\cdot\mathbf{n} \quad\;\; (\mathrm{A/m}) \end{aligned} \tag{14}$$

where ∇ indicates differentiation with respect to the unprimed variables. **M** is the magnetization vector and **n** is the outward unit vector normal to S. Finally, the magnetic flux density at the observation point outside the magnet is obtained

$$\mathbf{B}(\mathbf{r}) = \frac{\mu_0}{4\pi}\int_V \frac{\rho_m(\mathbf{r}')(\mathbf{r}-\mathbf{r}')}{|\mathbf{r}-\mathbf{r}'|^3}dv' + \frac{\mu_0}{4\pi}\oint_S \frac{\sigma_m(\mathbf{r}')(\mathbf{r}-\mathbf{r}')}{|\mathbf{r}-\mathbf{r}'|^3}ds' \tag{15}$$

A generic magnet model is shown in Fig. 8, wherein ρ_{in} and ρ_{out} is the inner and outer radius of the PM, respectively. It is assumed that the PM pole is uniformly magnetized with the parallel magnetization vector **M**. Hence the magnetic volume charge density is zero, that is, $\rho_m(\mathbf{r}') = 0$. The magnetic flux density at the observation point in the air outside the magnet can be rewritten as

$$\mathbf{B}(\mathbf{r}) = \frac{\mu_0}{4\pi}\oint_S \frac{\sigma_m(\mathbf{r}')(\mathbf{r}-\mathbf{r}')}{|\mathbf{r}-\mathbf{r}'|^3}ds' \tag{16}$$

The surface of the permanent magnet can be divided into six subsurfaces, each with its own unit vector as shown in Fig. 8. These normal vectors are defined as $\mathbf{n}_{1,2} = \pm\mathbf{e}_\rho$, $\mathbf{n}_{3,4} = \mp\mathbf{e}_\phi$, $\mathbf{n}_{5,6} = \pm\mathbf{e}_z$. For a uniformly magnetized PM, the magnetization vector is presented as $\mathbf{M}(\mathbf{r}') = M\cdot\mathbf{r}'$, where $M = \frac{B_{\mathrm{rem}}}{\mu_0}$ with the remanent magnetization of the PM, B_{rem}. The corresponding magnetic surface charge densities are given by

$$\begin{aligned} \sigma_{\mathrm{m}1,2} &= \mathbf{M}\cdot\mathbf{n}_{1,2} = \pm M \\ \sigma_{\mathrm{m}3,4} &= \mathbf{M}\cdot\mathbf{n}_{3,4} = -M\cdot\sin(\frac{\alpha}{2}) \\ \sigma_{\mathrm{m}5,6} &= \mathbf{M}\cdot\mathbf{n}_{5,6} = 0 \end{aligned} \tag{17}$$

where α is the range of the tile angle defined in the xy-plane. The resulting magnetic flux density on the surfaces of the permanent magnet can be obtained in the cylindrical coordinate system in Eq. (18).

$$\begin{aligned} \mathbf{B}_{1,2} &= \frac{\mu_0}{4\pi}\int_{s_{1,2}} \frac{\sigma_{\mathrm{m}1,2}(\mathbf{r}-\mathbf{r}')}{|\mathbf{r}-\mathbf{r}'|^3}ds' \\ &= \frac{\mu_0 M}{4\pi} \\ &\quad\times \int_{z_1}^{z_2}\int_{\phi_1}^{\phi_2} \frac{(\rho-\rho_{\mathrm{out,in}})\mathbf{e}_\rho + (\phi-\phi')\mathbf{e}_\phi + (z-z')\mathbf{e}_z}{(\rho^2+\rho_{\mathrm{out,in}}^2 - 2\rho\rho_{\mathrm{out,in}}\cos(\phi-\phi') + (z-z')^2)^{3/2}} \\ &\quad\times \rho_{\mathrm{out,in}}d\phi'dz' \\ \mathbf{B}_{3,4} &= \frac{\mu_0}{4\pi}\int_{s_{3,4}} \frac{\sigma_{\mathrm{m}3,4}(\mathbf{r}-\mathbf{r}')}{|\mathbf{r}-\mathbf{r}'|^3}ds' \\ &= \frac{\mu_0 M}{4\pi}\sin(\frac{\alpha}{2}) \\ &\quad\times \int_{z_1}^{z_2}\int_{\rho_{\mathrm{in}}}^{\rho_{\mathrm{out}}} \frac{(\rho-\rho')\mathbf{e}_\rho + (\phi-\phi_{1,2})\mathbf{e}_\phi + (z-z')\mathbf{e}_z}{(\rho^2+\rho'^2-2\rho\rho'\cos(\phi-\phi_{1,2}) + (z-z')^2)^{3/2}}d\rho'dz' \\ \mathbf{B}_{5,6} &= \frac{\mu_0}{4\pi}\int_{s_{5,6}} \frac{\sigma_{\mathrm{m}5,6}(\mathbf{r}-\mathbf{r}')}{|\mathbf{r}-\mathbf{r}'|^3}ds' = 0 \end{aligned} \tag{18}$$

The total magnetic flux density in the air gap, generated by one single permanent magnet, is the summation of the individual magnetic flux densities, hence

$$\mathbf{B}(\mathbf{r}) = \sum_{i=1}^{6}\mathbf{B}_i \tag{19}$$

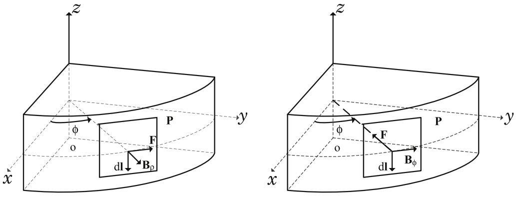

(a) ρ-direction. (b) ϕ-direction.

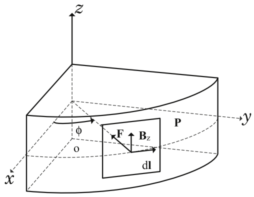

(c) z-direction.

Fig. 9. Force activated by three components of the flux density.

The magnetic field distribution produced by all separate slide units can be calculated by the superposition of all the models of PM in different positions.

4.2. Formulation of torque model

The torque can be obtained according to Lorentz Force Law

$$\mathbf{T} = -\int_v \mathbf{r} \times (\mathbf{J} \times \mathbf{B})dv \tag{20}$$

where the negative sign indicates that the force imposed on the rotor slide unit is the reaction force of the one exerted by the magnetic field, and $\mathbf{J}$ represents the current density of the stator coils, defined as

$$\mathbf{J} = \frac{\Delta\mathbf{I}}{\Delta S} = \frac{\Delta N_t \cdot \mathbf{I}_j}{\Delta S} \tag{21}$$

where $\mathbf{I}_j$ is the current passing through solid conductor of jth stator coil, N_t is the loop number of the stator coil, and $\Delta\mathbf{I}$ is the current that passes through the sectional area ΔS.

The direction of the force generated by each component of the flux density can be determined as shown in Fig. 9. The differential length d$\mathbf{l}$ of the wire is tangent to the cylindrical surface. $\mathbf{P}$ is a plane tangential to the cylindrical surface. $\mathbf{B}_\phi$ and $\mathbf{B}_z$ are vectors on plane $\mathbf{P}$, and $\mathbf{B}_\rho$ is normal to plane $\mathbf{P}$. Only $\mathbf{B}_\rho$ can produce a torque to change the rotor orientation, because the action lines of magnetic forces generated by $\mathbf{B}_\phi$ and $\mathbf{B}_z$ pass through the central axis z, which does not produce the rotational torque. The torque model is only based on the radial component $\mathbf{B}_\rho$.

To simplify the computation of the torque output, the rectangular-shape coil denoted by ABCD can be approximated by a tile-shaped coil denoted by A′B′C′D′ in the cylindrical coordinate system, which has been reviewed in a spherical coordinate in literature [24].

Fig. 10 shows the differential sectional area of $d\mathbf{l}$ which can be computed by $ds = \rho d\rho d\phi$. The current passing through this section area is $J\rho d\rho d\phi$, where J is the current density in the sectional area of the coil. According to Lorentz force law, the differential force on the rotor slide unit caused by the interaction between magnetic field of the rotor and the current-carrying conductor I$d\mathbf{l}$ is

$$d\mathbf{F} = -\mathrm{I}d\mathbf{l} \times B_\rho(\rho,\phi,z)\mathbf{e}_\rho = -J\rho d\rho d\phi d\mathbf{l} \times B_\rho(\rho,\phi,z)\mathbf{e}_\rho \tag{22}$$

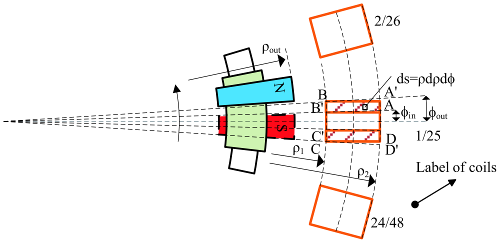

(a) Sectional view.

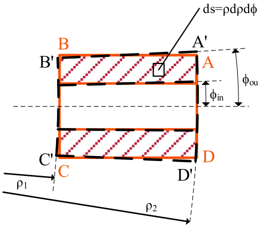

(b) Zoomed view of the cross-section of a single coil.

Fig. 10. Diagram of coil approximation.

According to Eq. (20), the torque generated by one single coil is the integration of the differential torque within the entire volume covered by the coil,

$$\boldsymbol{\tau} = J\int_{\rho_1}^{\rho_2}\int_{\phi_{in}}^{\phi_{out}}\{\int_C \rho\mathbf{e}_\rho \times [B_\rho(\rho,\phi,z)\mathbf{e}_\rho \times d\mathbf{l}]\}\rho d\rho d\phi \tag{23}$$

where $\int_C$ denotes the line integral of the differential torque along a rectangular loop of the winding that has a section area of ds. Moreover, ϕ_{in} and ϕ_{out} are two angles defining the shape of the cross-section, as shown in Fig. 10. The differential length $d\mathbf{l}$ which is perpendicular to $\mathbf{e}_\rho$ leads to the relationship, $\mathbf{e}_\rho \times \mathbf{e}_\rho \times d\mathbf{l} = -d\mathbf{l} = d\mathbf{z}$. As a result, Eq. (23) becomes

$$\boldsymbol{\tau} = -J\int_{\rho_1}^{\rho_2}\int_{\phi_{in}}^{\phi_{out}}\{\int_C \rho B_\rho(\rho,\phi,z)d\mathbf{z}\}\rho d\rho d\phi \tag{24}$$

The torque $\boldsymbol{\tau}_{i,j}$ exerted on the ith slide unit by the jth coil can be rewritten as

$$\boldsymbol{\tau}_{i,j} = \boldsymbol{\lambda}(\phi_{i,j}, z_j)\mathrm{I}_j \tag{25}$$

where $\boldsymbol{\lambda}(\phi_{i,j}, z_j) = -\frac{\mathrm{N_t}}{\mathrm{S}}\int_{\rho_1}^{\rho_2}\int_{\phi_{in}}^{\phi_{out}}\{\int_C \rho B_\rho(\rho,\phi_{i,j},z_j)d\mathbf{z}\}\rho d\rho d\phi$.

In this model, stator coils are wound on non-ferromagnetic cores, hence the torque output is proportional to the current output. Therefore, the actuated torque generated by multiple coils can be obtained by using the superposition of the torque generated by every single coil, that is,

$$\boldsymbol{\tau}_a = \boldsymbol{\lambda}\mathbf{I} \tag{26}$$

where $\boldsymbol{I} = \begin{bmatrix}\mathrm{I}_1 & \mathrm{I}_2 & \cdots & \mathrm{I}_n\end{bmatrix}^T$ is the input current vector of the stator coils, and $\boldsymbol{\lambda}$ is the complete torque matrix, derived by

$$\boldsymbol{\lambda} = \begin{bmatrix}\boldsymbol{\lambda}(\phi_{1,1},z_1) & \boldsymbol{\lambda}(\phi_{1,2},z_2) & \cdots & \boldsymbol{\lambda}(\phi_{1,n},z_n)\\ \boldsymbol{\lambda}(\phi_{2,1},z_1) & \boldsymbol{\lambda}(\phi_{2,2},z_2) & \cdots & \boldsymbol{\lambda}(\phi_{2,n},z_n)\\ \boldsymbol{\lambda}(\phi_{3,1},z_1) & \boldsymbol{\lambda}(\phi_{3,2},z_2) & \cdots & \boldsymbol{\lambda}(\phi_{3,n},z_n)\end{bmatrix} \tag{27}$$

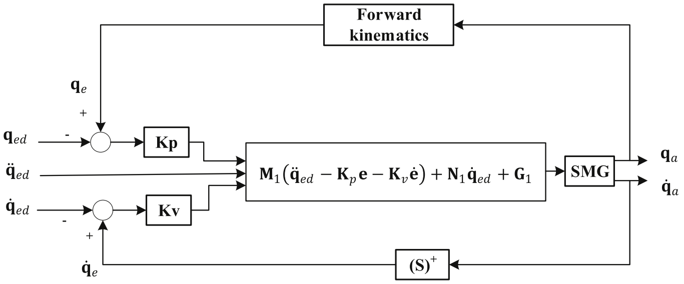

Fig. 11. Computed torque control.

By introducing a weightings matrix **R**, the inverse torque model can be solved by [25]

$$\mathbf{I}=\mathbf{R}^{-1}\boldsymbol{\lambda}^T(\boldsymbol{\lambda}\mathbf{R}^{-1}\boldsymbol{\lambda}^T)^{-1}\boldsymbol{\tau}_a \tag{28}$$

where $\boldsymbol{\tau}_a$ is the driving torque obtained in the dynamic model. **R** is a positive definite matrix in the form of

$$\mathbf{R}=\mathrm{diag}\begin{bmatrix}\mathrm{R}_1 & \mathrm{R}_2 & \dots & \mathrm{R}_n\end{bmatrix} \tag{29}$$

where $\mathrm{R}_1, \mathrm{R}_2, \dots, \mathrm{R}_n$ are positive weightings determined by coil's resistance. When the calculated currents are within the current limits, the results could be applied to the coils directly, and the power consumption of the system is minimized.

If the current input exceeds its saturate current, the desired torque could not be reached. In this situation, the desired torque can be calculated by using the principle of minimizing the energy consumption with the compensation of other coils by current redistribution. This can be formulated as follows:

$$\text{Minimize} \quad w=\mathbf{I}^T\mathbf{R}\mathbf{I} \tag{30}$$

$$\text{Subject to} \quad \boldsymbol{\tau}_a=\boldsymbol{\lambda}\mathbf{I} \tag{31}$$

$$\mathbf{I}\le\mathbf{I}_{\max} \tag{32}$$

$$\mathbf{I}_{\min}\le\mathbf{I} \tag{33}$$

So far, we have developed all models needed.

5. Task-space trajectory tracking control

The analytical model allows us to develop an effective control method for motion control, for example, trajectory tracking. In this section, we include a trajectory control, in which the model is used in a control method, namely, computed torque control.

The computed torque control has a good trajectory tracking ability and can overcome the external disturbance to achieve an ideal control performance [26], compared with other control algorithms like PID [27] and augmented PD control as shown in Fig. 11. The control law of the computed torque method is

$$\boldsymbol{\tau}_a=(\mathbf{S}^T)^+(\mathbf{M}_1(\ddot{\mathbf{q}}_{ed}-\mathbf{K}_v\dot{\mathbf{e}}-\mathbf{K}_p\mathbf{e})+\mathbf{N}_1\dot{\mathbf{q}}_e+\mathbf{G}_1) \tag{34}$$

where $\mathbf{e}=\mathbf{q}_e-\mathbf{q}_{ed}$, and $\mathbf{K}_v$ and $\mathbf{K}_p$ are constant gain matrices. When Eq. (34) is substituted into Eq. (12), the error dynamics can be written as

$$(\mathbf{S}^T)^+\mathbf{M}_1(\ddot{\mathbf{e}}+\mathbf{K}_v\dot{\mathbf{e}}+\mathbf{K}_p\mathbf{e})=0 \tag{35}$$

Since $\mathbf{M}_1$ is always positive definite, we have

$$\ddot{\mathbf{e}}+\mathbf{K}_v\dot{\mathbf{e}}+\mathbf{K}_p\mathbf{e}=0 \tag{36}$$

This is a linear differential equation which governs trajectory tracking control.

Table 1
Parameters of the SMG.

Parameter	Value
Arc angle of proximal curve links α_1	90°
Arc angle of distal curve links α_2	90°
Geometry of mobile platform β	60°
Radius of mid-curve R_c	100 mm
Inner radius of PM ρ_{in}	85 mm
Outer radius of PM ρ_{out}	115 mm
Inner radius of stator coil ρ_1	116 mm
Outer radius of stator coil ρ_2	130 mm
Tilt angle of PM pole α	7°
Number of coils n	48
Number of coil turns N_t	1600

Table 2
Mass and inertia properties of the SMG.

Parameter	Mass (kg)	Inertia property $[I_{xx}\ I_{yy}\ I_{zz}]$ (10^{-4} kg m^2)
Mobile platform	0.397	[3.8511 3.8511 3.8511]
Curve link	0.361	[6.0480 0.1449 6.1665]
Sliding unit	0.94	[0.3527 0.3496 0.5182]

Eq. (34) is called the computed torque control law, which can be written as two components,

$$\begin{aligned}\boldsymbol{\tau}_a&=[(\mathbf{S}^T)^+(\mathbf{M}_1\ddot{\mathbf{q}}_{ed}+\mathbf{N}_1\dot{\mathbf{q}}_e+\mathbf{G}_1)]+[(\mathbf{S}^T)^+\mathbf{M}_1(-\mathbf{K}_v\dot{\mathbf{e}}-\mathbf{K}_p\mathbf{e})]\\&=[\boldsymbol{\tau}_{ff}]+[\boldsymbol{\tau}_{fb}]\end{aligned} \tag{37}$$

The term $\boldsymbol{\tau}_{ff}$ is the feedforward component, which provides the amount of torque necessary to drive the system along its nominal path. The term $\boldsymbol{\tau}_{fb}$ is the feedback component, which provides correction torques to reduce any errors in the trajectory of the manipulator. The computed torque control law converts a nonlinear dynamical system into a linear one, which is a general technique known as feedback linearization, where a nonlinear system is rendered linear via full-state nonlinear feedback.

6. Simulations

In this section, the analytical models of the kinematics, dynamics and the torque are simulated and compared with the numerical results, and the computed torque method is validated. The parameters of SMG for the simulations are shown in Table 1.

6.1. Simulation of inverse kinematics and dynamics

Based on the inverse kinematics and dynamics, a model is built to illustrate the motion with Matlab/Simulink. The mass and inertia properties are given in Table 2.

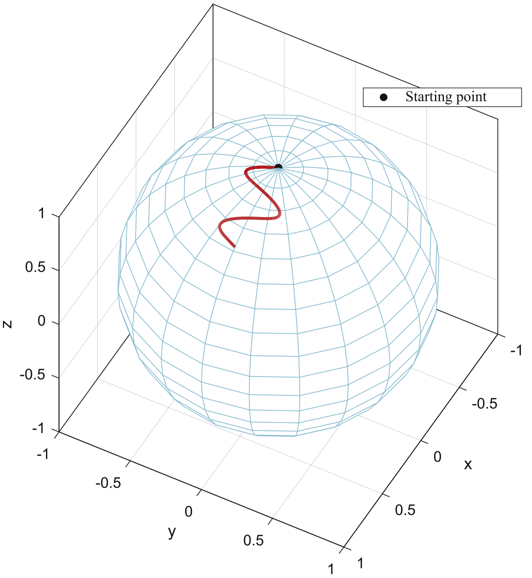

Fig. 12. Trajectory of the mobile platform orientation.

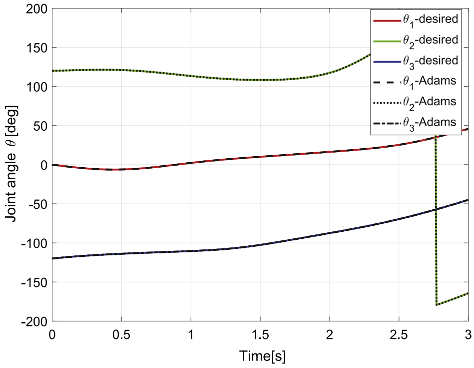

Fig. 13. Rotations of three slide units.

The trajectory of the mobile platform in terms of X–Y–Z Euler angles is designed as

$$\phi = \frac{\pi}{18}\sin(\pi t), \theta = 0.2t, \sigma = 0.3\pi + \frac{\pi}{72}t^3 \tag{38}$$

all with unit of rad. The desired trajectory of the mobile platform is shown in Fig. 12. The moment of inertia of the mobile platform takes value of [3.885, 3.885, 7.668] (10^{-4} kg m^2) as adopted from [16], which is about one order lower in magnitude, compared with the moment of inertia of the rotor in PMSM [10] in Fig. 1, [2.219, 2.176, 2.256] (10^{-3} kg m^2). Furthermore, compared with the SPM with co-axial shafts driven by the three attached motors in Fig. 2(a), the SMG can generate commensurate torques using the same parameters of the kinematic chains in Table 1 and the same mass and inertia properties in Table 2.

The simulation results are shown in Figs. 13 and 14. For comparison purpose, an ADAMS model was also developed, with the same set of parameters of the system and trajectory. The results from ADAMS model are displayed in Figs. 13 and 14 as well. It is seen that these two models agree well with each other.

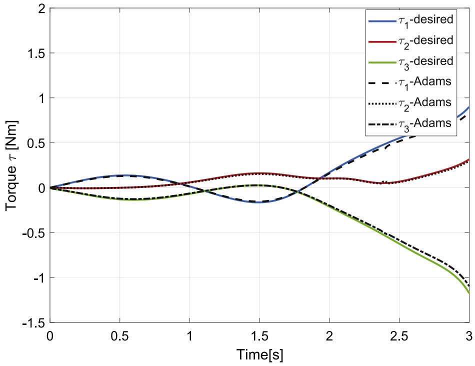

Fig. 14. Driving torques of three PM slide units.

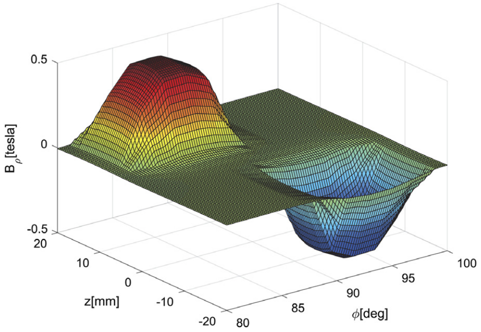

Fig. 15. Analytical results of 3D radial magnetic field distribution B_ρ at $\rho = 116$ mm.

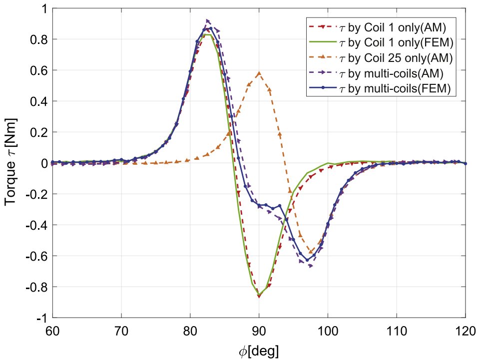

Fig. 16. T_z generated by one slide unit and two coils.

6.2. Simulation of torque model

The magnetic flux density **B** can be analyzed in three scalar components in the cylindrical coordinate system, B_ρ, B_ϕ and B_z.

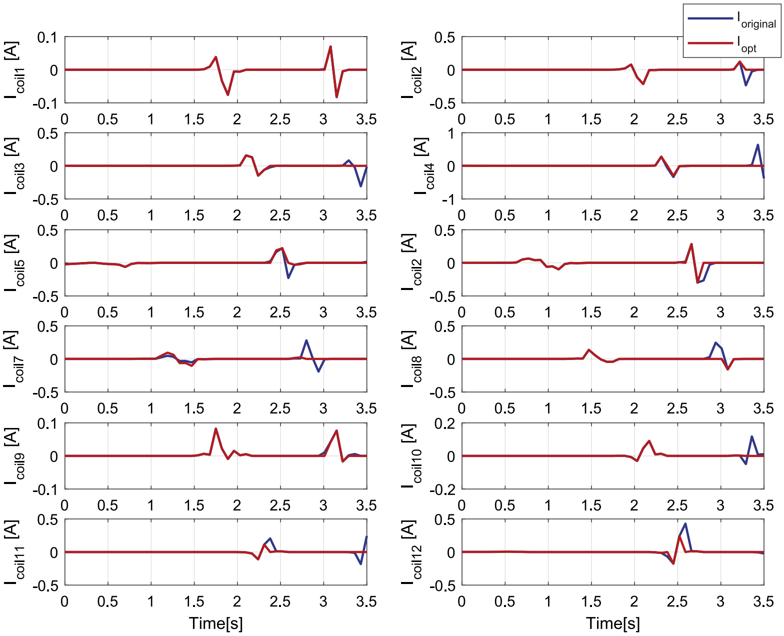

Fig. 17. The original and optimized input currents.

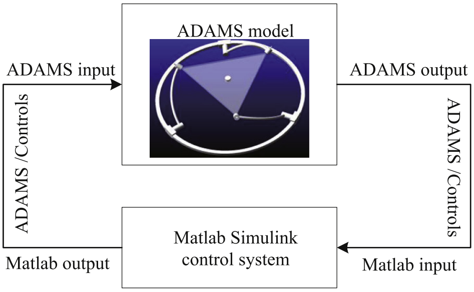

Fig. 18. Co-simulation block diagram.

The torque that produces the rotation movement is only dependent on B_ρ. Thus, only the radial magnetic field distribution of one slide unit which is positioned along the y-axis is shown in Fig. 15.

Fig. 15 shows the 3D distribution of the radial component of the flux density calculated by the analytical models. It can be seen that the peak values of B_ρ appear at the centerline of every PM. The analytical model was validated with a FEM software package from Ansoft, Maxwell 15, and the error is found about 5.62%, which is acceptable [28].

Fig. 16 shows the torque calculated from Eq. (24). It shows the torques produced by one slide unit with one coil and two coils, respectively. There are three sets of data obtained. They are torques produced by energizing Coil 1 in current output 3 A alone, torque by Coil 25 in current output −2 A alone, and torque by Coil 1 and Coil 25 simultaneously. It can be seen from the figure that the analytical torque model fits the Maxwell results well. It is noted that the superposition principle is used to obtain the torque generated by two individual coils in the analytical torque model. The result fits well with the torque generated by energizing two coils simultaneously in the Maxwell model.

From the above analysis, the maximum output torque of the SMG generated by a single coil can reach about 0.8 N m with maximum input current of 3 A. With the similar size dimensions and the same input current, the proposed SMG can generate a larger output torque compared with the PMSM whose maximum torque generated by a single coil is about 0.3 N m in [11]. The output torque of the SPMs actuated by separated motors mainly depends on the size of the conventional motors used, which can vary significantly.

6.3. Inverse torque model

The simulation examples using the proposed current optimal algorithm are included and the optimization problem is solved with the toolbox Yalmip [29]. As all the coils have the same property and are evenly spaced, the positive weighting **R** is normalized to 1. The desired torque is the output of the inverse dynamic model. The orientations of three slide units are their joint angles from the inverse kinematic model. The simulation results are shown in Fig. 17. Only twelve input currents are presented. The blue line represents the current inputs without current optimization, and the red line represents the optimized current inputs. It can be seen from Fig. 17 that the difference between the redistributed currents and the original currents is noticeable.

6.4. Trajectory tracking control

We finally include an example of trajectory control by the computed torque method (CTM) to illustrate the application of

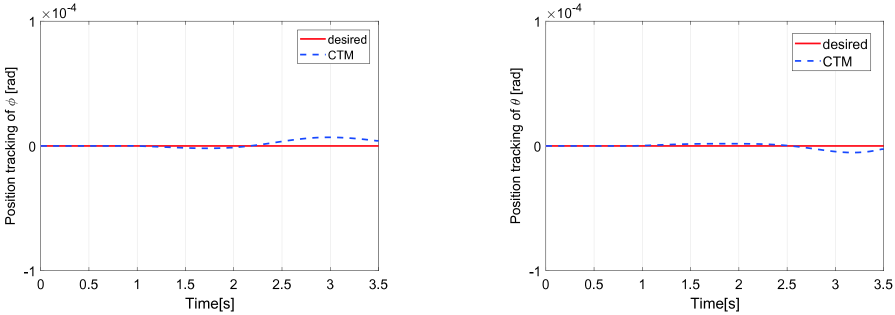

(a) Trajectory tracking of ϕ.

(b) Trajectory tracking of θ.

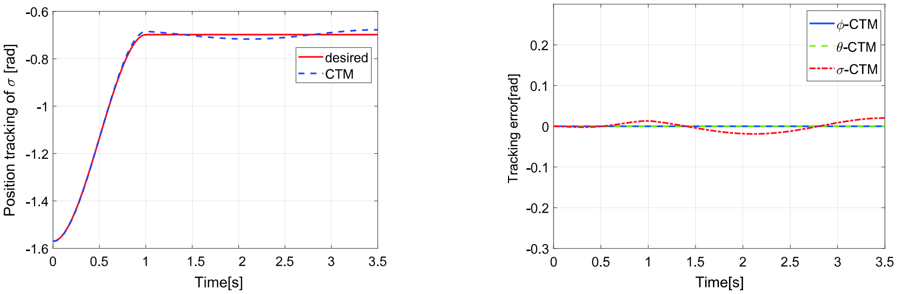

(c) Trajectory tracking of σ.

(d) Trajectory errors.

Fig. 19. Simulation results of CTM.

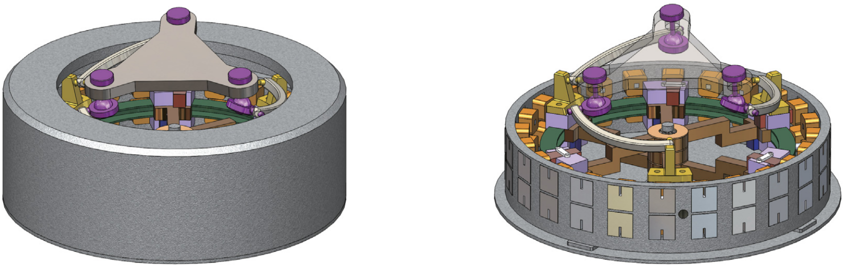

(a) Overall design.

(b) Internal view with housing removed.

Fig. 20. An embodiment of SMG.

the developed kinematics and dynamics models. A co-simulation Matlab Simulink/ADAMS model is developed shown as Fig. 18. The simplified mechanical structure is developed in Solidworks 3D, and then imported to the ADAMS model. The desired trajectory is defined in Simulink, the controlled torques from the control system are treated as the inputs of the ADAMS model and the trajectory of the mobile platform is then used as the feedback for the control. By using the co-simulation techniques efficiently [30], the whole virtual prototype is tested.

The simulation results of CTM are compared with the desired and CTM results in Fig. 19(a)–(c), and the tracking errors of the CTM results are shown in Fig. 19(d). The maximum state error of CTM is 0.65%, which is nearly equal to zero.

7. Design of SMG

A design of the SMG is depicted in Fig. 20. In the embodiment, three slide units are connected to the circular guide of the stator by using three identical links. The circular guide is constructed by two sets of HCR guides from THK, which can obtain the slide units' circular motion with high precision. To keep the balance of the rotor slide unit, a symmetric layout is adopted.

The control system consists of a PC, a digital signal processor (DSP), a field programmable gate array (FPGA), a current output device, a current output device, a current sampling device and an orientation measurement module, which is shown in Fig. 21. The DSP is responsible for task scheduling, algorithm computing

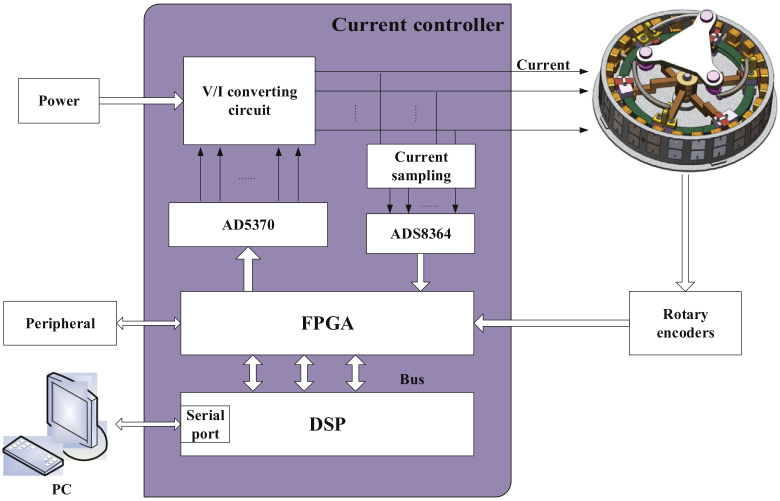

Fig. 21. Block diagram of control system.

and communicating with the host computer. The FPGA performs the task of handing the data obtained from three uniformed rotary encoders ECI 119 from Heidenhain and driving the AD5370 and ADS8364 chips. The AD5370 is a D/A chip containing digital-to-analog converts with 40 channels and 16-bit resolution. The OPA549 (a power amplifier) is chosen to achieve V/I conversion, which can convert the analog voltage signals from AD5370 into current signal. An A/D chip ADS8364 offers 6-channel output with a 16-bit A/D converting resolution. The whole system of the prototype and control system is being constructed for further experiments.

8. Conclusion

This paper presents a new design of an integrated SMG driven by electromagnetics. The new design features with a simple structure and low inertia. In addition, the SMG uses only two layers of the stator coils, which makes the structure more compact and light-weight. In this work, the inverse kinematics and dynamics are studied. The model of output torque is developed by analytical model based on the calculated 3D magnetic field distribution of the rotor. The current inputs are optimized based on the principle of the energy minimization. A dynamic control algorithm, computed torque method, is used for the trajectory tracking in task space. Finally, simulations are built to show the validity of all the developed models.

A major contribution of the work is the development of an integrated model of the new SMG, which combines the kinematics of the SPM and the electromagnetic driven principle of the PMSM. The analytical models allow us for more comprehensive design analysis and motion control development. The included trajectory tracking by computed torque method illustrated the application of the model developed.

While the new SMG brings the above advantageous features over PMSM and SPMs, it also shows some limitations that could be improved. First, though the singularity-free workspace of the SMG is within a cone of 120° theoretically, some mechanical constraints will influence the real workspace. Second, the resolution of the electromagnetic actuation is decided by the distribution of the stator coils. The resolution will be improved with increasing the number of stator coils. In addition, the output torque of the new SMG is determined by the electromagnetic force and the generator dimension. Hence, optimum design for the SMG, including both the mechanical parameters and the design of the PM and stator coils, could be considered in the future. Currently, a prototype is being developed. Furthermore testing will be conducted upon the available prototype.

Acknowledgments

This work is partially supported by National Nature Science Foundation of China under Grant No. 51475033. The first author acknowledges the CSC scholarship (File No. 201506020021) for her study at Aalborg University, Denmark.

Appendix

The orientation of the mobile platform is described with the orientation representation of X–Y–Z Euler Angles ($\phi - \theta - \sigma$), for which the rotation matrix $\mathbf{Q}$ is defined by Eq. (A.1), where $s(\cdot) = \sin(\cdot)$ and $c(\cdot) = \cos(\cdot)$.

$$\mathbf{Q} = \begin{bmatrix} c(\theta)c(\sigma) & -c(\theta)s(\sigma) & s(\theta) \\ c(\phi)s(\sigma) + s(\phi)s(\theta)c(\sigma) & c(\phi)c(\sigma) - s(\phi)s(\theta)s(\sigma) & -s(\phi)c(\theta) \\ s(\phi)s(\sigma) - c(\phi)s(\theta)c(\sigma) & s(\phi)c(\sigma) + c(\phi)s(\theta)s(\sigma) & c(\phi)c(\theta) \end{bmatrix} \tag{A.1}$$

Unit vector $\mathbf{u}_i$ is derived as

$$\mathbf{u}_i = [0 \quad 0 \quad -1]^T \tag{A.2}$$

The unit vector $\mathbf{w}_i$ of the axis of the intermediate revolute joint of the ith leg is expressed as

$$\mathbf{w}_i = \begin{bmatrix} (c\eta_i s\theta_i - s\eta_i c\theta_i)s\alpha_1 \\ (s\eta_i s\theta_i + c\eta_i c\theta_i)s\alpha_1 \\ -c\alpha_1 \end{bmatrix} \tag{A.3}$$

where $\eta_i = 2(i-1)\pi/3, i = 1, 2, 3$. The unit vector $\mathbf{v}_i$ of the top revolute joint is a function of the orientation of the mobile platform, which is described as

$$\mathbf{v}_i = \mathbf{Q}\mathbf{v}_i^* \tag{A.4}$$

where $\mathbf{v}_i^*$ is the unit vector for the axis of the top revolute joint of the ith leg when the mobile platform is in its reference orientation, which is given as

$$\mathbf{v}_i^* = [-s\eta_i s\beta \quad c\eta_i s\beta \quad c\beta]^T \tag{A.5}$$

Let $\boldsymbol{\omega} = [\omega_x \quad \omega_y \quad \omega_z]^T$ be the angular velocity of the mobile platform, then the joint velocity $\dot{\boldsymbol{\theta}} = [\dot{\theta}_1 \quad \dot{\theta}_2 \quad \dot{\theta}_3]^T$ can be obtained by

$$\mathbf{A_1}\omega = \mathbf{A_2}\dot{\theta} \tag{A.6}$$

with $\mathbf{A_1} = \left[\mathbf{a}_1 \quad \mathbf{a}_2 \quad \mathbf{a}_3\right]^T$, $\mathbf{a}_i = \mathbf{w}_i \times \mathbf{v}_i$ and $\mathbf{A_2} = diag\left[\mathbf{b}_1 \quad \mathbf{b}_2 \quad \mathbf{b}_3\right]$, $\mathbf{b}_i = (\mathbf{u}_i \times \mathbf{w}_i) \cdot \mathbf{v}_i$, $i = 1, 2, 3$. The Jacobian is finally obtained as

$$\mathbf{J_a} = \mathbf{A_1}^{-1}\mathbf{A_2} = [\mathbf{J}_1 \quad \mathbf{J}_2 \quad \mathbf{J}_3]^T \tag{A.7}$$

with $\mathbf{J}_i = \frac{\mathbf{w}_i \times \mathbf{v}_i}{(\mathbf{u}_i \times \mathbf{w}_i) \cdot \mathbf{v}_i}$.

References

[1] D. Kang, J. Lee, Analysis of electric machine charateristics for robot eyes using analytical electromagnetic field computation method, IEEE Trans. Magn. 50 (2) (2014) 785–788. http://dx.doi.org/10.1109/TMAG.2013.2278937.

[2] C.M. Gosselin, J.F. Hamel, The agile eye: a high-performance three-degree-of-freedom camera-orienting device, in: IEEE International Conference on Robotics and Automation, 1994, pp. 781–786. http://dx.doi.org/10.1109/ROBOT.1994.351393.

[3] T. Li, S. Payandeh, Design of spherical parallel mechanisms for application to laparoscopic surgery, Robotica 20 (2) (2002) 133–138. http://dx.doi.org/10.1017/S0263574701003873.

[4] T. Mashimo, K. Awaga, S. Toyama, Development of a spherical ultrasonic motor with an attitude sensing system using optical fibers, in: IEEE International Conference on Robotics and Automation, 2007, pp. 4466–4471. http://dx.doi.org/10.1109/ROBOT.2007.364167.

[5] S. Toyama, A. Kobayashi, Development of spherical ultrasonic motor, CIRP Ann.-Manuf. Technol. 45 (1) (1996) 27–30. http://dx.doi.org/10.1016/S0007-8506(07)63010-8.

[6] T. Yano, T. Suzuki, Basic characteristics of the small spherical stepping motor, in: IEEE/RSJ International Conference on Intelligent Robots and Systems, Vol. 2, 2002, pp. 1980–1985. http://dx.doi.org/10.1109/IRDS.2002.1044046.

[7] B. Dehez, D. Grenier, B. Raucent, Two-degree-of-freedom spherical actuator for omnimobile robot, in: IEEE International Conference on Robotics and Automation, 2002, pp. 2381–2386. http://dx.doi.org/10.1109/ROBOT.2002.1013588.

[8] L. Rossini, S. Mingard, A. Boletis, E. Forzani, E. Onillon, Y. Perriard, Rotor design optimization for a reaction sphere actuator, IEEE Trans. Ind. Appl. 50 (3) (2014) 1706–1716. http://dx.doi.org/10.1109/TIA.2013.2282660.

[9] M. Strumik, R. Wawrzaszek, M. Banaszkiewicz, K. Seweryn, M. Sidz, E. Onillon, L. Rossini, Analytical model of eddy currents in a reaction sphere actuator, IEEE Trans. Magn. 50 (6) (2014) 1–7. http://dx.doi.org/10.1109/TMAG.2014.2298215.

[10] J. Liu, H. Deng, C. Hu, Z. Hua, W. Chen, Adaptive backstepping sliding mode control for 3-dof permanent magnet spherical actuator, Aerosp. Sci. Technol. 67 (2017) 62–71. http://dx.doi.org/10.1016/j.ast.2017.03.032.

[11] W. Chen, L. Zhang, L. Yan, J. Liu, Design and control of a three degree-of-freedom permanent magnet spherical actuator, Sensors Actuators A 180 (2012) 75–86. http://dx.doi.org/10.1016/j.sna.2012.04.010.

[12] W. Chen, L. Zhang, F. Guo, J. Liu, Design and modeling of a spherical actuator with three dimensional orientation measurement system, in: Advanced Materials Research, Vol. 317, 2011, pp. 1088–1097. http://dx.doi.org/10.4028/www.scientific.net/AMR.317-319.1088.

[13] M.A. González-Palacios, C.J. Ortega-Alvarez, J.G. Sandoval-Castillo, S.M. Cuevas-Ledesma, F.J. Mendoza-Patiño, The generalized architecture of the spherical serial manipulator, Adv. Robot. Autom. 05 (2) (2016). http://dx.doi.org/10.4172/2168-9695.1000148.

[14] S. Bai, J. Angeles, The design of spherical multilobe-cam mechanisms, Proc. Inst. Mech. Eng. C 223 (2) (2009) 473–482. http://dx.doi.org/10.1243/09544062JMES1154.

[15] S. Bai, Optimum design of spherical parallel manipulators for a prescribed workspace, Mech. Mach. Theory 45 (2) (2010) 200–211. http://dx.doi.org/10.1016/j.mechmachtheory.2009.06.007.

[16] G. Wu, S. Caro, S. Bai, J. Kepler, Dynamic modeling and design optimization of a 3-DOF spherical parallel manipulator, Robot. Auton. Syst. 62 (10) (2014) 1377–1386. http://dx.doi.org/10.1016/j.robot.2014.06.006.

[17] B. Sudki, M. Lauria, F. Noca, Marine propulsor based on a three-degree-of-freedom actuated spherical joint, in: Proceedings of the 3rd International Symposium on Marine Propulsors, 2013, pp. 481–485.

[18] W.H. Yuan, M.S. Tsai, A novel approach for forward dynamic analysis of 3-prs parallel manipulator with consideration of friction effect, Robot. Comput.-Integr. Manuf. 30 (3) (2014) 315–325. http://dx.doi.org/10.1016/j.rcim.2013.10.009.

[19] H.R.M. Daniali, P.J. Zsombor-Murray, J. Angeles, The kinematics of 3-DOF planar and spherical double-triangular parallel manipulators, in: J. Angeles, G. Hommel, P. Kovács (Eds.), Computational Kinematics, Kluwer Academic Publishers, Dordrecht, 1993, pp. 153–164. http://dx.doi.org/10.1007/978-94-015-8192-9_14.

[20] C. Gosselin, J. Angeles, Singularity analysis of closed-loop kinematic chains, IEEE Trans. Robot. Autom. 6 (3) (1990) 281–290. http://dx.doi.org/10.1109/70.56660.

[21] D.W. Kang, W.H. Kim, S.C. Go, C.S. Jin, S.H. Won, D.H. Koo, J. Lee, Method of current compensation for reducing error of holding torque of permanent-magnet spherical wheel motor, IEEE Trans. Magn. 45 (6) (2009) 2819–2822. http://dx.doi.org/10.1109/TMAG.2009.2018676.

[22] B. vanNinhuijs, T.E. Motoasca, B.L.J. Gysen, E.A. Lomonova, Modeling of spherical magnet arrays using the magnetic charge model, IEEE Trans. Magn. 49 (7) (2013) 4109–4112. http://dx.doi.org/10.1109/TMAG.2012.2235411.

[23] E.P. Furlani, Permanent Magnet and Electromechanical Devices: Materials, Analysis, and Applications, Academic Press, 2001.

[24] L. Yan, I.-M. Chen, G. Yang, K.-M. Lee, Analytical and experimental investigation on the magnetic field and torque of a permanent magnet spherical actuator, IEEE/ASME Trans. Mechatronics 11 (4) (2006) 409–419. http://dx.doi.org/10.1109/TMECH.2006.878545.

[25] Y. Nakamura, Advanced Robotics: Redundancy and Optimization, Addison-Wesley Longman Publishing Co., Inc., 1990.

[26] Q. Li, F. Wu, Control performance improvement of a parallel robot via the design for control approach, Mechatronics 14 (8) (2004) 947–964. http://dx.doi.org/10.1016/j.mechatronics.2004.04.002.

[27] J. Alvarez-Ramirez, I. Cervantes, R. Kelly, PID regulation of robot manipulators: stability and performance, Systems Control Lett. 41 (2) (2000) 73–83. http://dx.doi.org/10.1016/S0167-6911(00)00038-4.

[28] X. Li, S. Bai, W. Chen, J. Liu, Integrated design and modelling of an electromagnets driven spherical parallel manipulator, in: IEEE International Conference on Advanced Intelligent Mechatronics (AIM), 2017, pp. 1209–1214. http://dx.doi.org/10.1109/AIM.2017.8014183.

[29] J. Lofberg, YALMIP: a toolbox for modeling and optimization in MATLAB, in: IEEE International Symposium on Computer Aided Control Systems Design, 2004, pp. 284–289. http://dx.doi.org/10.1109/CACSD.2004.1393890.

[30] S. Mohan, B. Corves, Inverse dynamics and trajectory tracking control of a new six degrees of freedom spatial 3-RPRS parallel manipulator, Mech. Sci. 8 (2) (2017) 235–248. http://dx.doi.org/10.5194/ms-8-235-2017.

Xuerong Li received the B.S. degree from China Agricultural University, China, in 2012. She finished her Master study in Automation Science in 2015 at Beihang University, Beijing, China. Her current research interests include parallel robots, actuators and control systems.

Jingmeng Liu received the B.S. degree from Anhui Polytechnic University, China, in 1991, and the M.S. and Ph.D. degrees from Beihang University, China, in 2000 and 2004 respectively. He is currently an Associate Professor in the school of Automation Science and Electrical Engineering, Beihang University, China. His current research interests include actuators, precision control, and mechatronics.

Weihai Chen received the B.S. degree from Zhejiang University, China, in 1982, and the M.S. and Ph.D. degrees from Beihang University, China, in 1988 and 1996 respectively. He is currently a Professor in the school of Automation Science and Electrical Engineering, Beihang University, China. His current research interests include modular robots, actuators, automation, and control.

Shaoping Bai received the Ph.D. Degree in Mechanical and Production Engineering from the Nanyang Technological University, Singapore in 2001, the M.Eng. Degree from Tsinghua University and B.S. Degree from Harbin Institute of Technology in 1993 and 1988, respectively. He is currently an Associate Professor at the Department of Materials and Production, Aalborg University (AAU), Denmark. His research interests include dynamics and design, assistive exoskeletons, parallel manipulators, and walking robots.

Chapter 4

Paper II

Dynamic modeling and trajectory tracking control of an electromagnetic direct driven spherical motion generator

Xuerong Li, Shaoping Bai and Ole Madsen

The paper has been published in the
Robotics and Computer-Integrated Manufacturing Vol. 59(2019), pp. 201–212,
2019.

Robotics and Computer Integrated Manufacturing 59 (2019) 201–212

Contents lists available at ScienceDirect

Robotics and Computer Integrated Manufacturing

journal homepage: www.elsevier.com/locate/rcim

Full length Article

Dynamic modeling and trajectory tracking control of an electromagnetic direct driven spherical motion generator

Xuerong Li, Shaoping Bai*, Ole Madsen

Department of Materials and Production, Aalborg University, Aalborg 9220, Denmark

ARTICLE INFO

Keywords:
Spherical motion generator
Dynamic modeling
Robust adaptive switching learning control
Spherical parallel manipulator
Trajectory tracking

ABSTRACT

As the demands for multi-degree-of-freedom actuators increase, novel mechanical-electrical integrated designs of motion generator are required for robotic applications. In this work, a spherical motion generator integrating electromagnetic actuators with a 3-RRR spherical parallel manipulator is introduced. The design allows to generate 3-DOF rotations in a compact structure. In this paper, a complete dynamic model in the task space is built for the integrated system, with consideration of uncertainties such as modeling errors and external disturbances. Addressing the uncertainties in the model, a robust adaptive switching learning control algorithm is developed, which can improve its trajectory tracking performance. The stability of the proposed method is analyzed by using Lyapunov method. A co-simulation platform by Matlab/Simulink and ADAMS was developed, with simulations conducted. The results show that the proposed control algorithm has better trajectory tracking performance and robustness to uncertainties.

1. Introduction

A spherical motion generator (SMG) is a type of devices which can produce 3-degree-of-freedom (3-DOF) rotational motions. The SMGs have potential applications in machine tools, solar panels, orientating devices [1,2] and medical instruments [3].

Up to date, SMGs with various structures and working principles have been investigated. One type of the SMG is the 3-DOF permanent magnet spherical motor (PMSM) [4,5]. A PMSM consists of a rotor constructed by spherical permanent magnet array and a set of stator windings distributed uniformly in a spherical shape, which offers advantages of compact structure, high energy density and rapid response [6,7]. Another type of the SMG is in the form of spherical parallel manipulators (SPM) which are actuated by separate motors. SPMs have many advantages in terms of accuracy, high stiffness and large load capacity [8]. A well-known SPM is the Agile Eye developed by Gosselin et. which is applied for camera orienting [9]. SPMs which can achieve unlimited rolling rotation were designed in [8,10]. Various problems of the SPM have been studied including singularity analysis [11], dexterity evaluation [12] and design optimization [13,14]. In a recent work, an electromagnetic direct driven SMG was designed [15,16], which integrates the parallel mechanism and electromagnetic actuation in a more compact and simple structure. The integrated design takes both advantages of the electromagnetic driving principle of PMSMs and the parallel kinematics of SPM. In addition, the non-contact electromagnetic driven principle eliminates the use of motors and gears, which leads to no backlash and less mechanical wear. The mechanical and electromagnetic models have been developed [16]. The dynamic modeling and trajectory tracking control of the integrated SMG is the focus of this work.

In trajectory tracking, due to the uncertainties and nonlinear behavior of the dynamic system, accurate tracking is a challenging task to implement. Many control methods have been developed in this regard. One of the most popular controllers is the classic proportional-derivative (PD) controller. PD control scheme can be used for trajectory tracking with the asymptotic stability with appropriate control gains [17]. However, PD control scheme is not satisfactory in high accuracy demanded applications without the compensation for the modeling uncertainties and external disturbances in the dynamics, and it cannot guarantee the stability at a high speed [18]. To linearize and decouple the strongly nonlinear coupling manipulator system, a model-based control scheme, namely, computed torque method (CTM), can be employed [19,20]. Nonetheless, the CTM is prone to external disturbance and cannot obtain good trajectory tracking performance [21]. In recent years, intelligent control schemes such as neural networks control, adaptive control, robust control [22,23] and etc. are proposed as well. The neural networks control and adaptive control can cope with the parameter uncertainties [24,25], however, they both require extensive computation and have

---

* Corresponding author.
E-mail address: shb@mp.aau.dk (S. Bai).

https://doi.org/10.1016/j.rcim.2019.04.009
Received 22 August 2018; Received in revised form 23 February 2019; Accepted 9 April 2019

limitations to real-time control applications. Iterative learning control (ILC) is applied for robot manipulators of repetitive tasks due to its simplicity and robustness to modeling uncertainties [26,27]. Hybrid control schemes which merge ILC with other control schemes are studied [28,29]. One of hybrid controllers is the adaptive switching learning PD (ASL-PD) controller which takes advantages of combined control methods [30]. In this method, a PD control law plus a feedforward learning control law with the input torque from the previous iteration is used to compensate for modeling errors and repetitive disturbances. Furthermore, the gains in the PD feedback law are adapted using the switching control technique to ensure the fast convergence. In [31], this method was applied to the control of a spherical motor to deal with random and nonrepetitive noise.

The objective of this work is to develop a high-accuracy trajectory tracking control scheme for the novel electromagnetic driven SMG which is able to compensate for model uncertainties and external disturbances. The dynamic model of SMG is established in task space with modeling errors and disturbances considered. Based on the dynamic model, a robust adaptive switching learning PD (RASL-PD) control algorithm is proposed. The control method combines ASL-PD controller with a robust term to decouple the nonlinear dynamic model of SMG and to compensate for various modeling uncertainties and external disturbances in real time. An accurate trajectory tracking can thus be achieved.

The rest of paper is organized as follows. Section 2 describes the mechanical structure and working principle of the spherical motion generator. Section 3 depicts dynamic model of the SMG in task space. Section 4 introduces the proposed trajectory tracking control, RASL-PD algorithm, in task space and analyzes its stability based on Lyapunov's method. Co-simulations built in Matlab/Simulink and ADAMS are conducted and the trajectory tracking performances are discussed in Section 5. Finally, conclusions are made in Section 6.

2. Mechanical structure and working principle

An embodiment of the integrated SMG is depicted in Fig. 1. The SMG is composed of two parts, a spherical parallel manipulator (SPM) and an electromagnetic driver. The SPM of the SMG is built on a conceptual design in [14]. As shown in Fig. 2, the SMG is made of three identical serial chains connecting the mobile platform to the fixed base circular guide. Each leg is composed of one curve link and a sliding unit which can rotate independently around the circular guide. All the joints between the links are revolute, and all the axes of the revolute joints intersect at a center point. The electromagnetic driven part consists of permanent magnet rotors and a stator. The rotor structure is constructed by three sliding units. Fig. 3 shows the construction of a sliding unit. Each sliding unit consists of two PM poles in two layers, namely, a lower and an upper layer. The two PM poles are of parallel magnetization. In Fig. 3, the blue arrow presents the magnetization direction of the upper PM, and the red arrow presents the magnetization direction of the lower PM. The PM poles are set in the rotor shell which can smoothly move around circular guide with the rotation center **O** through ceramic bearings. The circular guide is constructed by two sets of HCR guides from THK, which can also guarantee that the sliding units' high-precise rotation. There are 48 coils distributed in two layers symmetrically about the equatorial plane of the stator.

Fig. 4 shows the working principle of SMG. When the currents of the stator coils are activated, the three sliding units will be driven by the electromagnetic force between the PM poles and stator coils to realize different spherical motion at the end-effector. When all the sliding units are actuated with equal torques continuously,[1] the sliding units can move coherently and the end-effector can spin about its own axis. Alternatively, the sliding units can be driven with different torques, the SMG will produce 3D motion at the end-effector.

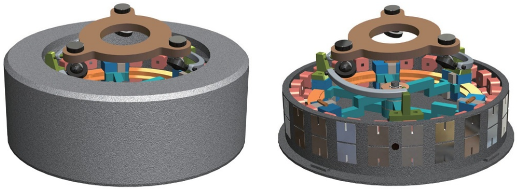

(a) Overall design (b) Internal view with housing removed

Fig. 1. Embodiment of SMG.

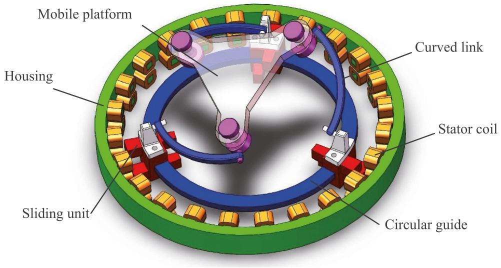

Fig. 2. Conceptual model of SMG.

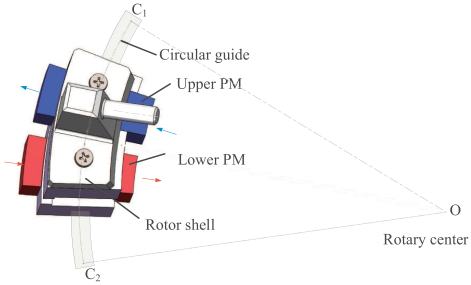

Fig. 3. Construction of the sliding unit.

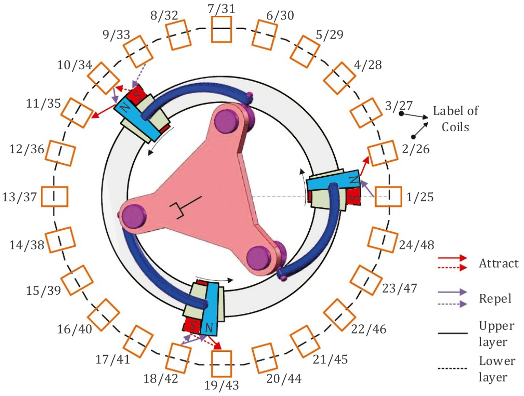

Fig. 4. Working principle of integrated electromagnetic driven SMG.

---

[1] The sliding unit is a spherical prismatic joint which is a special form of revolute joint with rotation center at the sphere center, analog to the planar prismatic joint, which can be considered as a special form of revolute joint with rotation center at the infinity [32]. Thus torque can be applied.

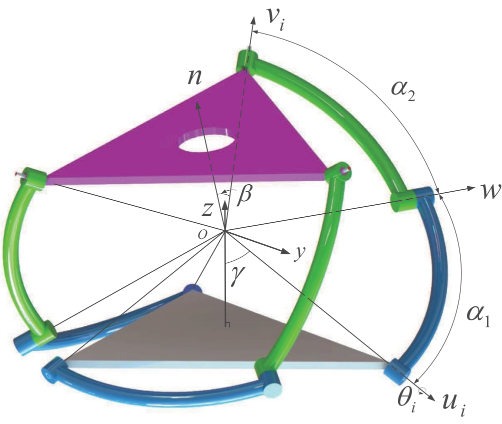

Fig. 5. Kinematic model of SPM.

3. SMG kinematics and dynamics

3.1. Inverse kinematics

The kinematics of SMG can be modeled as a 3-RRR SPM with coaxial shafts. The SPM has three revolute joints whose axes are denoted by unit vectors $\mathbf{u}_i$, $\mathbf{v}_i$ and $\mathbf{w}_i$, $i = 1, 2, 3$. All three links that are connected to the base platform and mobile platform have identical dimensions of α_1 and α_2, respectively. Furthermore, β defines the geometry of the regular pyramid of the mobile platform and γ defines the geometry of the regular pyramid of base platform. A general spherical parallel manipulator is shown in Fig. 5. The SMG kinematics pertains to a special case of general SPMs for which $\gamma = 0$.

The kinematic model has been documented in [16], therefore, the details will not be repeated. In this work, we define that $\mathbf{q} = [\mathbf{q}_a^{\mathrm{T}} \quad \mathbf{q}_e^{\mathrm{T}}]^{\mathrm{T}}$ is the generalized coordinates of the manipulator, with $\mathbf{q}_a = [\theta_1 \quad \theta_2 \quad \theta_3]^{\mathrm{T}}$ being the vector of actuated joint angles, and $\mathbf{q}_e = [\phi \quad \theta \quad \sigma]^{\mathrm{T}}$ being the vector of X-Y-Z Euler angles of the mobile platform. Let $\boldsymbol{\omega} = [\omega_x \quad \omega_y \quad \omega_z]^{\mathrm{T}}$ denote the angular velocity of the mobile platform, the relationship between the angular velocity $\boldsymbol{\omega}$ and input joint velocity $\dot{\mathbf{q}}_a = [\dot{\theta}_1 \quad \dot{\theta}_2 \quad \dot{\theta}_3]^{\mathrm{T}}$ can be stated as

$$\mathbf{B}\dot{\mathbf{q}}_a = \mathbf{A}\boldsymbol{\omega} \tag{1}$$

with

$$\mathbf{A} = \begin{bmatrix} (\mathbf{w}_1 \times \mathbf{v}_1)^{\mathrm{T}} \\ (\mathbf{w}_2 \times \mathbf{v}_2)^{\mathrm{T}} \\ (\mathbf{w}_3 \times \mathbf{v}_3)^{\mathrm{T}} \end{bmatrix} \tag{2}$$

$$\mathbf{B} = \mathrm{diag}\{(\mathbf{u}_1 \times \mathbf{w}_1)\cdot\mathbf{v}_1,\ (\mathbf{u}_2 \times \mathbf{w}_2)\cdot\mathbf{v}_2,\ (\mathbf{u}_3 \times \mathbf{w}_3)\cdot\mathbf{v}_3\} \tag{3}$$

where matrix $\mathbf{A}$ is the forward Jacobian matrix of the manipulator, and $\mathbf{B}$ is the inverse Jacobian matrix. In addition, the transformation matrix between the angular velocity $\boldsymbol{\omega}$ and the angle rates of mobile platform $\dot{\mathbf{q}}_e = [\dot{\phi} \quad \dot{\theta} \quad \dot{\sigma}]^{\mathrm{T}}$ can be described as

$$\dot{\omega} = \boldsymbol{\Phi}\dot{\mathbf{q}}_e \tag{4}$$

with

$$\boldsymbol{\Phi} = \begin{bmatrix} 1 & 0 & s(\theta) \\ 0 & c(\phi) & -s(\phi)c(\theta) \\ 0 & s(\phi) & c(\phi)c(\theta) \end{bmatrix}$$

and $s(\cdot) = \sin(\cdot)$ and $c(\cdot) = \cos(\cdot)$. If $\mathbf{B}$ is nonsingular, the kinematic Jacobian matrix $\mathbf{J}$ is obtained as

$$\mathbf{J} = \mathbf{B}^{-1}\mathbf{A}\Phi \tag{5}$$

The velocity relations of the manipulator can be obtained with the help of the inverse Jacobian matrix,

$$\begin{aligned} \dot{\mathbf{q}}_a &= \mathbf{J}\dot{\mathbf{q}}_e \\ \dot{\mathbf{q}} &= \begin{bmatrix} \dot{\mathbf{q}}_a \\ \dot{\mathbf{q}}_e \end{bmatrix} = \begin{bmatrix} \mathbf{J}\dot{\mathbf{q}}_e \\ \dot{\mathbf{q}}_e \end{bmatrix} = \mathbf{S}\dot{\mathbf{q}}_e \end{aligned} \tag{6}$$

where $\mathbf{S} = [\mathbf{J}^{\mathrm{T}} \quad \mathbf{I}]^{\mathrm{T}}$, $\mathbf{I}$ is the 3×3 identity matrix.

3.2. Dynamic model in task space

The mechanical structure of a SMG is shown in Fig. 2. The rotation is generated by the electromagnetic forces between the coils and the PM poles. By varying the current inputs of the stator coils, the desired 3-DOF motion can be achieved within the workspace.

The dynamic model of the SMG with constraints can be obtained by Lagrange equations as follows

$$\begin{aligned} \mathbf{M}_t(\mathbf{q})\ddot{\mathbf{q}} + \mathbf{N}_t(\mathbf{q}, \dot{\mathbf{q}})\dot{\mathbf{q}} + \mathbf{G}_t(\mathbf{q}, \dot{\mathbf{q}}) + \mathbf{C}_q^{\mathrm{T}}\boldsymbol{\lambda} &= \tau \\ \mathbf{C}_q^{\mathrm{T}}\dot{\mathbf{q}} &= \mathbf{0} \end{aligned} \tag{7}$$

where $\mathbf{M}_t(\mathbf{q})$ is the inertial matrix of the system; $\mathbf{N}_t(\mathbf{q}, \dot{\mathbf{q}})$ is the centripetal-Coriolis matrix; $\mathbf{G}_t(\mathbf{q}, \dot{\mathbf{q}})$ is the gravity term. $\mathbf{C}_q = [\mathbf{B} \quad -\mathbf{A}\Phi]$ is the constraint Jacobian and $\boldsymbol{\lambda} = [\lambda_1 \quad \lambda_2 \quad \lambda_3]^{\mathrm{T}}$ is a vector of Lagrange multipliers. $\tau = [\tau_a^{\mathrm{T}} \quad \mathbf{0}_3]^{\mathrm{T}}$ are the generalized forces of the SMG, and the vector $\tau_a = [\tau_1 \quad \tau_2 \quad \tau_3]^{\mathrm{T}}$ presents the input actuator torques.

In general, the motion of the SMG is specified with reference to the end-effector, namely, the trajectory of $\mathbf{q}_e$. Therefore, it is better to derive the control algorithm directly in the task space than the joint space. The dynamic model established in task space can be rewritten as following

$$\mathbf{M}(\mathbf{q})\ddot{\mathbf{q}}_e + \mathbf{N}(\mathbf{q}, \dot{\mathbf{q}})\dot{\mathbf{q}}_e + \mathbf{G}(\mathbf{q}, \dot{\mathbf{q}}) = \tau_a \tag{8}$$

where

$$\begin{aligned} \mathbf{M}(\mathbf{q}) &= \mathbf{J}^{-\mathrm{T}}(\mathbf{q})\mathbf{S}^{\mathrm{T}}(\mathbf{q})\mathbf{M}_t(\mathbf{q})\mathbf{S}(\mathbf{q}) \\ \mathbf{N}(\mathbf{q}, \dot{\mathbf{q}}) &= \mathbf{J}^{-\mathrm{T}}(\mathbf{q})\mathbf{S}^{\mathrm{T}}(\mathbf{q})(\mathbf{N}_t(\mathbf{q}, \dot{\mathbf{q}})\mathbf{S}(\mathbf{q}) + \mathbf{M}_t(\mathbf{q})\dot{\mathbf{S}}(\mathbf{q})) \\ \mathbf{G}(\mathbf{q}, \dot{\mathbf{q}}) &= \mathbf{J}^{-\mathrm{T}}(\mathbf{q})\mathbf{S}^{\mathrm{T}}\mathbf{G}_t(\mathbf{q}, \dot{\mathbf{q}}) \end{aligned}$$

$\mathbf{M}(\mathbf{q})$ is the inertial matrix in task space; $\mathbf{N}(\mathbf{q}, \dot{\mathbf{q}})$ is the centripetal-Coriolis matrix, and $\mathbf{G}(\mathbf{q}, \dot{\mathbf{q}})$ is the gravity term in task space. It can be seen that the dynamic model contains nonlinear terms. Furthermore, modeling errors cannot be avoided during the dynamic modeling process. Considering the effects of the dynamic modeling uncertainties, the dynamic model in task space is rewritten as

$$\hat{\mathbf{M}}(\mathbf{q})\ddot{\mathbf{q}}_e + \hat{\mathbf{N}}(\mathbf{q}, \dot{\mathbf{q}})\dot{\mathbf{q}}_e + \hat{\mathbf{G}}(\mathbf{q}, \dot{\mathbf{q}}) = \tau_a - \tau_{d1} - \tau_{d2} \tag{9}$$

where $\hat{\mathbf{M}}(\mathbf{q})$, $\hat{\mathbf{N}}(\mathbf{q}, \dot{\mathbf{q}})$ and $\hat{\mathbf{G}}(\mathbf{q}, \dot{\mathbf{q}})$ are the actual inertial matrix, centripetal-Coriolis matrix and gravity term, respectively, which are expressed as

$$\begin{aligned} \hat{\mathbf{M}}(\mathbf{q}) &= \mathbf{M}(\mathbf{q}) + \Delta\mathbf{M}(\mathbf{q}) \\ \hat{\mathbf{N}}(\mathbf{q}, \dot{\mathbf{q}}) &= \mathbf{N}(\mathbf{q}, \dot{\mathbf{q}}) + \Delta\mathbf{N}(\mathbf{q}, \dot{\mathbf{q}}) \\ \hat{\mathbf{G}}(\mathbf{q}, \dot{\mathbf{q}}) &= \mathbf{G}(\mathbf{q}, \dot{\mathbf{q}}) + \Delta\mathbf{G}(\mathbf{q}, \dot{\mathbf{q}}) \end{aligned}$$

$\Delta\mathbf{M}(\mathbf{q})$, $\Delta\mathbf{N}(\mathbf{q}, \dot{\mathbf{q}})$ and $\Delta\mathbf{G}(\mathbf{q}, \dot{\mathbf{q}})$ are the modeling errors, τ_{d1} is the repetitive disturbance and τ_{d2} represents the nonrepetitive disturbance. We define

$$\mathbf{n}(\mathbf{q}, \dot{\mathbf{q}}, \ddot{\mathbf{q}}) = \Delta\mathbf{M}(\mathbf{q})\ddot{\mathbf{q}}_e + \Delta\mathbf{N}(\mathbf{q}, \dot{\mathbf{q}})\dot{\mathbf{q}}_e + \Delta\mathbf{G}(\mathbf{q}, \dot{\mathbf{q}})$$

Eq. (9) becomes

$$\mathbf{M}(\mathbf{q})\ddot{\mathbf{q}}_e + \mathbf{N}(\mathbf{q}, \dot{\mathbf{q}})\dot{\mathbf{q}}_e + \mathbf{G}(\mathbf{q}, \dot{\mathbf{q}}) + \mathbf{n}(\mathbf{q}, \dot{\mathbf{q}}, \ddot{\mathbf{q}}) = \tau_a - \tau_{d1} - \tau_{d2} \tag{10}$$

4. Robust adaptive switching learning PD algorithm

4.1. Controller design

The dynamic equation in Eq. (10) has the following properties which can be exploited to design the controller in this section:

Property 1. *The inertial matrix* $\mathbf{M}(\mathbf{q})$ *is symmetric, bounded and positive definite.*

Property 2. $\dot{\mathbf{M}}(\mathbf{q}) - 2\mathbf{N}(\mathbf{q}, \dot{\mathbf{q}})$ *is a skew symmetric matrix. Therefore,* $\mathbf{x}^{\mathrm{T}}(\dot{\mathbf{M}}(\mathbf{q}) - 2\mathbf{N}(\mathbf{q}, \dot{\mathbf{q}}))\mathbf{x} = 0$ *holds for any n-dimensional nonzero vector* $\mathbf{x}$.

Following assumptions are made:

Assumption 1. The given desired trajectory $\mathbf{q}_d(t)$ has the third-order continuity for $t \in [0, t_f]$.

Assumption 2. The initial conditions are $\mathbf{q}_e(0) = \mathbf{q}_{ed}(0)$ and $\dot{\mathbf{q}}_e(0) = \dot{\mathbf{q}}_{ed}(0)$.

Without losing of generality, we consider the controller processes the trajectory tracking in its k^{th} iteration. We linearize the system Eq. (10) along the desired trajectory $(\mathbf{q}_{ed}(t), \dot{\mathbf{q}}_{ed}(t), \ddot{\mathbf{q}}_{ed}(t))$ and obtain

$$\begin{aligned} &\mathbf{M}(t)\ddot{\mathbf{e}}^k(t) + (\mathbf{N}(t) + \mathbf{N}_1(t))\dot{\mathbf{e}}^k(t) + \mathbf{F}(t)\mathbf{e}^k(t) + \boldsymbol{\Psi}(t) \\ &\quad = \mathbf{H}(t) - \tau_a^k(t) + \tau_{d1}(t) + \tau_{d2}^k(t) + \mathbf{n}(t) \end{aligned} \tag{11}$$

where k denotes the iteration number, $\mathbf{e}^k(t)$ is the position error, $\dot{\mathbf{e}}^k(t)$ is the velocity error and

$$\begin{aligned} \mathbf{M}(t) &= \mathbf{M}(\mathbf{q}_d(t)) \\ \mathbf{N}(t) &= \mathbf{N}(\mathbf{q}_d(t), \dot{\mathbf{q}}_d(t)) \\ \mathbf{N}_1(t) &= \frac{\partial \mathbf{N}}{\partial \dot{\mathbf{q}}_e}\Big|_{\mathbf{q}_d(t),\dot{\mathbf{q}}_d(t)} \dot{\mathbf{q}}_{ed}(t) + \frac{\partial \mathbf{G}}{\partial \dot{\mathbf{q}}_e}\Big|_{\mathbf{q}_d(t),\dot{\mathbf{q}}_d(t)} \\ \mathbf{F}(t) &= \frac{\partial \mathbf{M}}{\partial \dot{\mathbf{q}}_e}\Big|_{\mathbf{q}_d(t)} \ddot{\mathbf{q}}_{ed}(t) + \frac{\partial \mathbf{N}}{\partial \dot{\mathbf{q}}_e}\Big|_{\mathbf{q}_d(t),\dot{\mathbf{q}}_d(t)} \dot{\mathbf{q}}_{ed}(t) \\ &\quad + \frac{\partial \mathbf{G}}{\partial \dot{\mathbf{q}}_e}\Big|_{\mathbf{q}_d(t),\dot{\mathbf{q}}_d(t)} \\ \mathbf{H}(t) &= \mathbf{M}(t)\ddot{\mathbf{q}}_{ed}(t) + \mathbf{N}(t)\dot{\mathbf{q}}_{ed}(t) + \mathbf{G}(\mathbf{q}_d(t), \dot{\mathbf{q}}_d(t)) \\ \mathbf{n}(t) &= \mathbf{n}(\mathbf{q}_d(t), \dot{\mathbf{q}}_d(t), \ddot{\mathbf{q}}_d(t)) \\ \mathbf{e}^k(t) &= \mathbf{q}_{ed}(t) - \mathbf{q}_e^k(t) \\ \dot{\mathbf{e}}^k(t) &= \dot{\mathbf{q}}_{ed}(t) - \dot{\mathbf{q}}_e^k(t) \end{aligned}$$

The term $\boldsymbol{\Psi}(t)$ consists the higher order terms $\ddot{\mathbf{e}}^k(t)$, $\dot{\mathbf{e}}^k(t)$, $\mathbf{e}^k(t)$. For the k^{th} and $(k+1)^{\text{th}}$ iterations, Eq. (11) can be rewritten as follows, respectively:

$$\begin{aligned} &\mathbf{M}(t)\ddot{\mathbf{e}}^k(t) + (\mathbf{N}(t) + \mathbf{N}_1(t))\dot{\mathbf{e}}^k(t) + \mathbf{F}(t)\mathbf{e}^k(t) + \boldsymbol{\Psi}^k(t) \\ &\quad = \mathbf{H}(t) - \tau_a^k(t) + \tau_{d1}(t) + \tau_{d2}^k(t) + \mathbf{n}(t) \end{aligned} \tag{12}$$

$$\begin{aligned} &\mathbf{M}(t)\ddot{\mathbf{e}}^{k+1}(t) + (\mathbf{N}(t) + \mathbf{N}_1(t))\dot{\mathbf{e}}^{k+1}(t) + \mathbf{F}(t)\mathbf{e}^{k+1}(t) + \boldsymbol{\Psi}^{k+1}(t) \\ &\quad = \mathbf{H}(t) - \tau_a^{k+1}(t) + \tau_{d1}(t) + \tau_{d2}^{k+1}(t) + \mathbf{n}(t) \end{aligned} \tag{13}$$

To find a control law for the nonlinear SMG system with uncertainties, we construct the robust adaptive switching learning PD algorithm as follows:

$$\tau_a^k(t) = \tau_f^k + \tau_r^k + \tau_a^{k-1} \tag{14}$$

with

$$\begin{aligned} \tau_f^k &= \mathbf{K}_p^k\mathbf{e}^k(t) + \mathbf{K}_d^k\dot{\mathbf{e}}^k(t) \\ \tau_r^k &= f \cdot \mathrm{sgn}((\Delta\mathbf{y}^{k-1})^{\mathrm{T}}) \end{aligned} \tag{15}$$

where τ_f^k is the PD feedback control term, τ_r^k is the robust control term and τ_a^{k-1} is the feedforward control term which satisfies the condition $\tau_a^k(t)|_{k=-1} = 0$.

In Eq. (15), matrices $\mathbf{K}_p^k$ and $\mathbf{K}_d^k$ are the control gains of k^{th} iteration which are updated by

$$\begin{cases} \mathbf{K}_p^k = \beta(k)\mathbf{K}_p^0 \\ \mathbf{K}_d^k = \beta(k)\mathbf{K}_d^0 \end{cases} k = 1, 2, \ldots, N \tag{16}$$

where $\beta(k)$ is the gain switching factor which is a function of the iteration number, satisfying the conditions $\beta(k+1) > \beta(k)$ and $\beta(k) > 1$ for $k = 1, 2, \ldots, N$. We define that $\mathbf{K}_p^0$ and $\mathbf{K}_d^0$ are the initial proportional and derivative control gain matrices which are both diagonal positive definite. Let $\mathbf{K}_p^0 = \Lambda\mathbf{K}_d^0$ for the initial iteration, $\mathbf{y}^k(t)$ is defined as

$$\mathbf{y}^k(t) = \dot{\mathbf{e}}^k(t) + \Lambda\mathbf{e}^k(t) \tag{17}$$

where Λ is the PD control gain. Defining $\Delta\mathbf{y}^k = \mathbf{y}^{k+1} - \mathbf{y}^k$ and $\Delta\mathbf{e}^k = \mathbf{e}^{k+1} - \mathbf{e}^k$, Eq. (17) becomes

$$\Delta\mathbf{y}^k = \Delta\dot{\mathbf{e}}^k + \Lambda\Delta\mathbf{e}^k \tag{18}$$

4.2. Convergence analysis

The convergence property of the tracking error with the proposed controller is guaranteed as proved presently.

Proposition 1. *Suppose the SMG in Eq. (11) satisfies Properties 1, 2 and Assumptions 1, 2. Consider the SMG with repetitive tasks under the controller (Eq. (14)) and the gain switching rule (Eq. (16)). Then for all* $t \in [0, t_f]$, *the following should hold* $\mathbf{q}^k(t) \overset{k\to\infty}{\to} \mathbf{q}_d(t)$ *and* $\dot{\mathbf{q}}^k(t) \overset{k\to\infty}{\to} \dot{\mathbf{q}}_d(t)$.

If the controller gains are selected properly, the following relationships hold:

$$\lambda_{\min}(\mathbf{K}_d^0 + 2\mathbf{N}_1 - 2\mathbf{M}\Lambda) \equiv l_1 > 0 \tag{19}$$

$$\lambda_{\min}(\mathbf{K}_d^0 + 2\mathbf{N} + 2\mathbf{F}/\Lambda - 2\dot{\mathbf{N}}_1/\Lambda) \equiv l_2 > 0 \tag{20}$$

$$\|\mathbf{F}/\Lambda - (\mathbf{N} + \mathbf{N}_1 - \Lambda\mathbf{M})\|_{\max}^2 \le l_1 l_2 \tag{21}$$

$$f - \|\mathbf{d}^k\| \ge 0 \tag{22}$$

where $\Delta\mathbf{d}^k = \mathbf{d}^{k+1} - \mathbf{d}^k$, $\mathbf{d}^k = \tau_{d2}^k - \Psi^k$, $\lambda_{\min}(\cdot)$ is the minimum eigenvalue of matrix $(\cdot)$, and $\|(\cdot)\|$ is the Euclidean norm.

It is noted that the inertia matrix $\mathbf{M}(\mathbf{q})$, centripetal-Coriolis matrix $\mathbf{N}(\mathbf{q}, \dot{\mathbf{q}})$, gravity matrix $\mathbf{G}(\mathbf{q}, \dot{\mathbf{q}})$, matrix $\mathbf{N}_1(t)$ and $\mathbf{F}(t)$ are all bounded, and there is no conflict among the conditions in Eqs. (19)–(21). Thus, the control parameters in $\mathbf{K}_d^0$ and f can be easily chosen to satisfy these conditions.

Define a Lyapunov function as

$$\mathbf{V}^k = \int_0^t \mathbf{e}^{-\rho\mu}(\mathbf{y}^k)^{\mathrm{T}}\mathbf{K}_d^0\mathbf{y}^k d\mu \ge \mathbf{0} \tag{23}$$

where ρ is a positive constant. It can be shown that $\mathbf{V}^{k+1} < \mathbf{V}^k$ in Eq. (23), as derived in Appendix A. Because $\mathbf{K}_d^0$ is a positive definite matrix, when $k \to 0$, $\mathbf{y}^k \to 0$. $\mathbf{e}^k(t)$ and $\dot{\mathbf{e}}^k(t)$ are two independent variables, and Λ is a positive constant. Thus, we can obtain

$$\lim_{k\to\infty}\mathbf{e}^k(t) = \mathbf{0},\ \lim_{k\to\infty}\dot{\mathbf{e}}^k(t) = \mathbf{0},\ \forall\ t \in [0, t_f] \tag{24}$$

Finally, for $t \in [0, t_f]$ the following conclusion holds

$$\begin{aligned} \mathbf{q}^k(t) &\overset{k\to\infty}{\to} \mathbf{q}_d(t) \\ \dot{\mathbf{q}}^k(t) &\overset{k\to\infty}{\to} \dot{\mathbf{q}}_d(t) \end{aligned} \tag{25}$$

It can be seen that as the number of iterations approaches infinity, the robust ASL-PD control method can guarantee that the tracking errors converge to zero.

As a matter of fact, the RASL-PD controller can converge to a very small error just in a few iterations. This can be observed from the simulations in the following section.

Table 1
Dimensions of the SMG.

Parameter	Value
Link dimension α_1	$\frac{\pi}{2}$ rad
Link dimension α_2	$\frac{\pi}{2}$ rad
Geometry of mobile platform β	$\frac{\pi}{3}$ rad
Radius of mid-curve R_c	100 mm

Table 2
Mass and inertia properties of the SMG.

Parameter	Mass (kg)	Inertia property [I_{xx} I_{yy} I_{zz}] (10^{-4}kg m^2)
Mobile platform	0.3972	[3.8511 3.8511 3.8511]
Curve link	0.361	[6.0480 0.1449 6.1665]
Sliding unit	0.94	[0.3527 0.3496 0.5182]

5. Co-simulations

In this section, a co-simulation platform is implemented by Matlab/Simulink and ADAMS.

5.1. Model implementation

The co-simulation platform of SMG can be realized by introducing Simulink module into the virtual ADAMS prototype in virtue of ADAMS/Controls module. The simplified components of SPM are first built in Solidworks 3D, and the dimensions are listed in Table 1. By importing the Solidworks files into ADAMS/View and specifying the connectors of various types, the virtual mechanical prototype is then established as shown in Fig. 6(a). The mass and inertial properties are specified in Table 2.

By defining the inputs and outputs of SPM in ADAMS, the variables of SMG can be transfered to control process by ADAMS/Control module. The calculated torques from the controller are the inputs of the ADAMS model, and the position and velocity outputs of ADAMS model

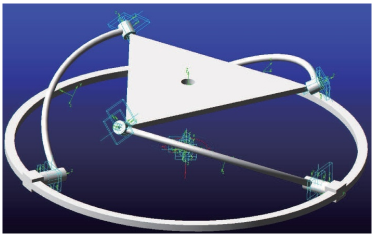

(a) ADAMS model

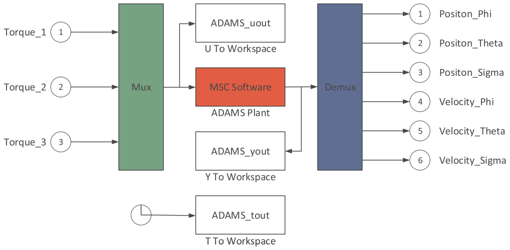

(b) Specification of Adams_sub

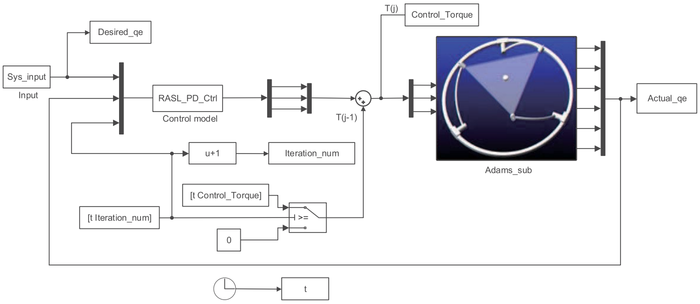

(c) Simulink model

Fig. 6. Block diagram of co-simulation platform by Matlab/Simulink and ADAMS.

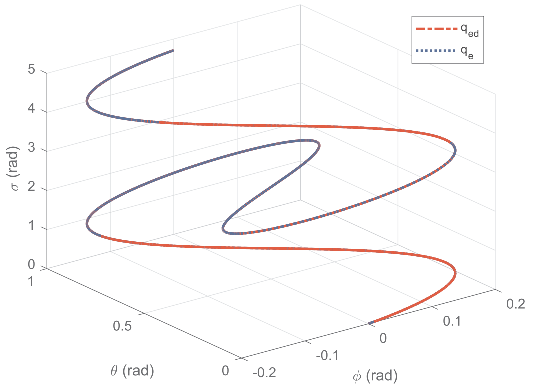

Fig. 7. Trajectory tracking with RASL-PD control at 4th iteration.

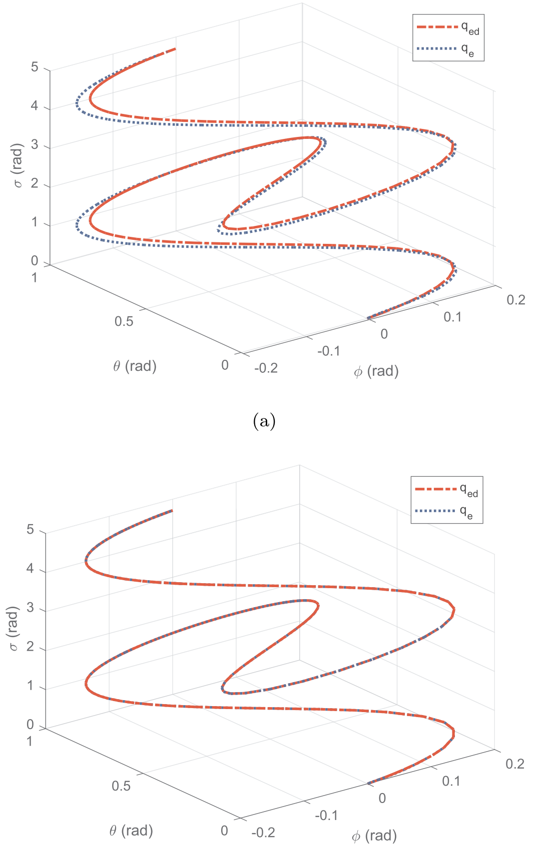

(a)

(b)

Fig. 8. Trajectory tracking with other algorithms, (a) PD control, (b) iterative learning control at 4th iteration.

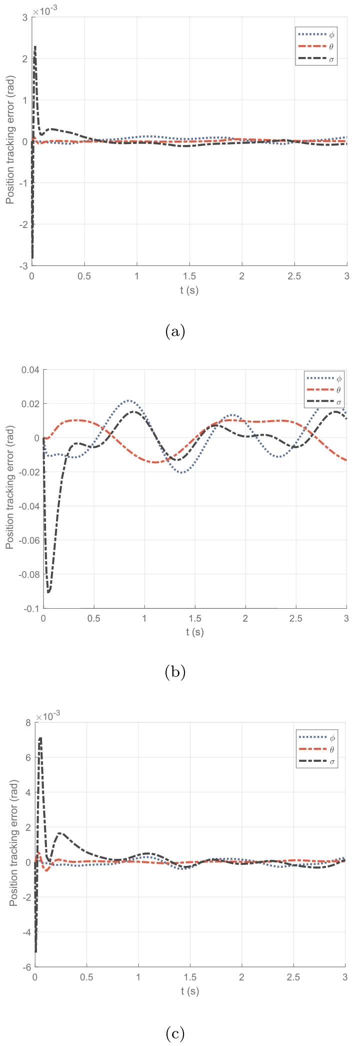

(a)

(b)

(c)

Fig. 9. Position tracking errors, (a) with RASL-PD control, (b) with PD control, (c) with iterative learning control.

are the actual motion information used as the feedback for the control, which is exported in block form of Simulink shown in the block *adams_sub* in Fig. 6(b). The desired trajectory of SMG and the proposed controller are designed in Matlab/Simulink, as shown in Fig. 6(c). The desired trajectory of the mobile platform in terms of X-Y-Z Euler angles is designed as

$$\phi = \frac{\pi}{18}\sin(\pi t),\ \theta = 0.5 - 0.5\cos\left(\frac{\pi}{2}t\right),\ \sigma = 0.5\pi t \tag{26}$$

all with unit (rad). The modeling errors are set as follows

Table 3
Position tracking errors.

Control algorithm	Maximum position tracking errors of [ϕ, θ, σ] (rad)
RASL-PD control	[1.2498×10^{-4}, 5.0300×10^{-5}, 0.0011]
PD control	[0.09, 0.01, 0.02]
Iterative learning control	[2.83×10^{-4}, 5.46×10^{-4}, 0.0072]

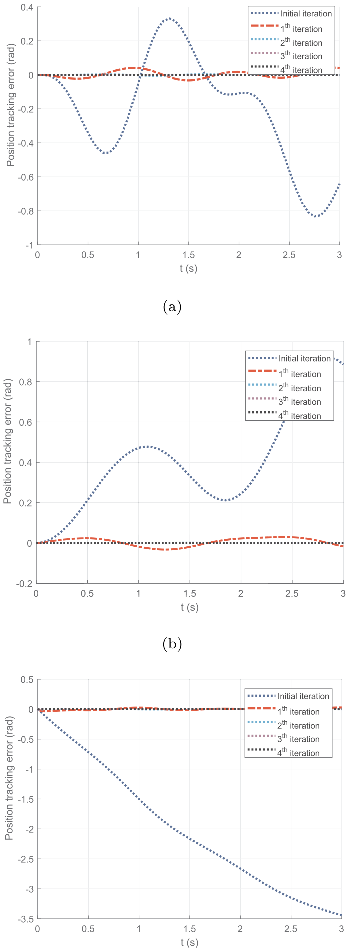

(a)

(b)

(c)

Fig. 10. Position tracking performance improvement over iterations, (a) e_ϕ, (b) e_θ, (c) e_σ.

$$\Delta\mathbf{M}(\mathbf{q}) = \zeta\mathbf{M}(\mathbf{q}), \quad \Delta\mathbf{N}(\mathbf{q}, \dot{\mathbf{q}}) = \zeta\mathbf{N}(\mathbf{q}, \dot{\mathbf{q}})$$
$$\Delta\mathbf{G}(\mathbf{q}, \dot{\mathbf{q}}) = \zeta\mathbf{G}(\mathbf{q}, \dot{\mathbf{q}})$$

where $\zeta = 0.2$ is the coefficient of the modeling error, which indicates the level of uncertainty. The external disturbance is set as

$$\tau_d = r\,[\cos(\pi t);\ \ \exp(-\pi t);\ \ \sin(2\pi t)]$$

where r is the coefficient of external disturbance which is randomly distributed in $(-0.01, 0.01)$.

The gain switching rule is set to be

$$\mathbf{K}_p^k = 2k\mathbf{K}_p^0, \quad \mathbf{K}_d^k = 2k\mathbf{K}_d^0 \quad \text{for } k = 1, 2, \ldots, N$$

The initial control gains are selected as

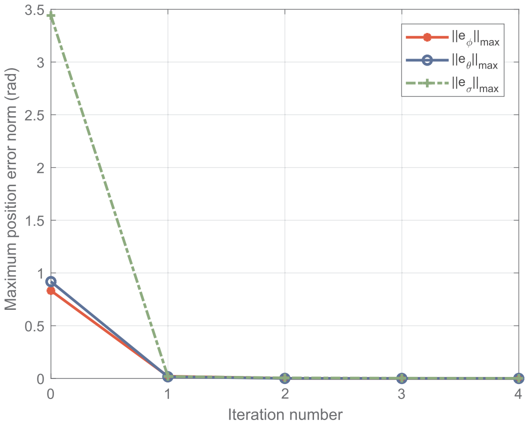

Fig. 11. Position tracking convergence during the iterative procedure.

$$\mathbf{K}_d^0 = \mathrm{diag}\{0.1, 0.1, 0.1\}, \quad \mathbf{K}_p^0 = \Lambda\mathbf{K}_d^0$$

where $\Lambda = 15$. The robust coefficient f is set as 0.02.

5.2. Results and discussion

Fig. 7 shows the tracking performance of the proposed algorithm at the 4th iteration. It can be seen that the actual trajectory tracking result of the proposed algorithm fits well with the desired trajectory. For comparison, simulations with two other methods, namely, PD control and iterative learning control [33] are included in this work. The trajectory tracking performance under the classic PD control with the same gains is displayed in Fig. 8(a). The results follow the desired trajectory with noticeable errors. Fig. 8(b) shows the tracking performance of the iterative learning control with the same initial gains. A better trajectory is obtained than the trajectory with PD method, but the performance of the algorithm is less better than that of the proposed RASL-PD control. Fig. 9 shows the position tracking errors of SMG using RASL-PD control, PD control and iterative learning control, respectively. The maximum position tracking errors of the three control algorithms are presented in Table 3. The maximum position tracking errors of PD and iterative learning control are 0.09 rad and 0.0072 rad, respectively. The maximum position tracking error of the proposed algorithm is 0.0011 rad, which is the smallest. Compared with PD and iterative learning control algorithms, the RASL-PD algorithm can obtain much better performance in the presence of model uncertainties and random external disturbances.

Fig. 10 shows the position tracking performance improvement over iterations. It can be seen that, at the initial iteration, the position tracking errors are not converging. However, with the increase of the iteration number, the proposed algorithm shows a fast convergence. The position tracking convergence with the iterative process is shown in Fig. 11, where the maximum position error norm is the maximum norm of each Euler angle's position tracking error. At the initial iteration, the maximum position error norms of e_ϕ, e_θ and e_σ are 0.8326, 0.9181, and 3.4412 rad, respectively. After the initial iteration, the maximum position error norms decrease rapidly, and at the 4th iteration, they have been reduced to 9.3445×10^{-5}, 4.9286×10^{-5}, and 0.0014 rad, respectively. It's noted that the position tracking performance improves as the iteration number increases.

The actuation torques required are illustrated in Fig. 12. It can be

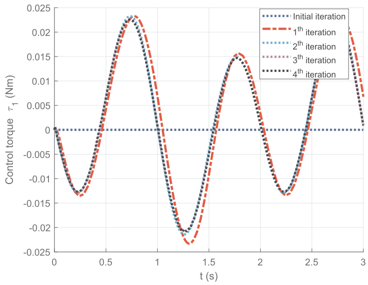

(a) Control torque τ_1

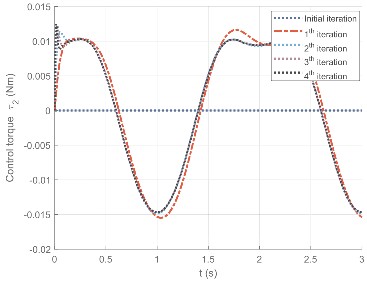

(b) Control torque τ_2

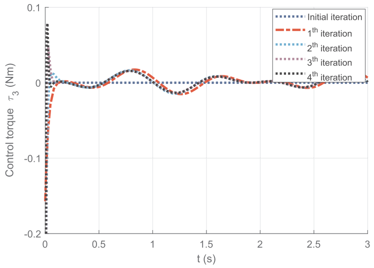

(c) Control torque τ_3

Fig. 12. Control torque variation over iterations.

noted that the torques are nearly the same from iteration to iteration after a few iterations. In this example, the torques vary smoothly and approach to the same from the second iteration to the fourth iteration. Above all, the effectiveness and robustness of the algorithm are verified.

In the presented work, we address the dynamics and control issues from the control aspect. It is noted that the problem can also be addressed by means of design to reduce the influence of nonlinear terms in the dynamic model, which can ease the challenges of control and improve the performance of an integrated system. Examples include the so-called design for control (DFC) [34], and adjustment of kinematic parameters (AKP) for real-time controllable robotic mechanisms [35], etc.

6. Conclusion

This paper presents a dynamic model for an integrated SMG driven by electromagnetics. The nonlinear dynamic model is established in task space with model uncertainties considered. A robust adaptive switching learning PD control scheme is investigated to control the position of end-effector for high trajectory tracking performance in the presence of uncertainties including the modeling errors and external disturbances. The convergence of the control system is also guaranteed by applying Lyapunov theorem. A co-simulation by Matlab/Simulink and ADAMS was developed, with results showing that the proposed algorithm can effectively deal with the modeling errors and disturbances. The significance of the proposed control algorithm is that it can achieve a fast convergence with easy implementation and good trajectory tracking performance.

A contribution of the work is the establishment of a dynamic model in the task space for the SMG, with which the model uncertainty and external disturbances are duly considered. This model enables further a robust adaptive switching learning PD control method. In the work, a co-simulation platform was developed, with which both dynamic model and control algorithms can be simulated. With the co-simulation platform, three control methods, including the one developed in this work, are simulated and compared, which justified the performance of the new control algorithm. This composes another contribution of the work.

The new motion generator can be used for many potential applications as pointing and orientating devices. It can also be considered for vector thrusting systems. In future work, a prototype is being developed and the proposed algorithm will be applied to the dynamic control of the prototype. Furthermore, the integrated design of the mechanical structure and control algorithms will be utilized for depth-study.

Acknowledgments

The first author acknowledges the financial support from the China Scholarship Council for her study at Aalborg University, Denmark.

Appendix A

The stability of the system is proved based on the Lyapunov function defined as Eq. (23).

From Eq. (14), we know

$$\boldsymbol{\tau}_a^{k+1} = \mathbf{K}_p^{k+1}\mathbf{e}^{k+1}(t) + \mathbf{K}_d^{k+1}\dot{\mathbf{e}}^{k+1}(t) + f\cdot\mathrm{sgn}((\Delta\mathbf{y}^k)^{\mathrm{T}}) + \boldsymbol{\tau}_a^k \tag{27}$$

From Eqs. (17) and (27), we have

$$\begin{aligned}\boldsymbol{\tau}_a^{k+1} - \boldsymbol{\tau}_a^k &= \mathbf{K}_p^{k+1}\mathbf{e}^{k+1}(t) + \mathbf{K}_d^{k+1}\dot{\mathbf{e}}^{k+1}(t) + f\cdot\mathrm{sgn}((\Delta\mathbf{y}^k)^{\mathrm{T}})\\ &= \mathbf{K}_d^{k+1}\mathbf{y}^{k+1} + f\cdot\mathrm{sgn}((\Delta\mathbf{y}^k)^{\mathrm{T}})\end{aligned} \tag{28}$$

Eqs. (12) and (13) lead to

$$\begin{aligned}&\mathbf{M}(\ddot{\mathbf{e}}^{k+1}-\ddot{\mathbf{e}}^{k})+(\mathbf{N}+\mathbf{N}_1)(\dot{\mathbf{e}}^{k+1}-\dot{\mathbf{e}}^{k})+\mathbf{F}(\mathbf{e}^{k+1}-\mathbf{e}^{k})\\&\quad=-(\tau_a^{k+1}-\tau_a^{k})+(\mathbf{d}^{k+1}-\mathbf{d}^{k})\end{aligned}\tag{29}$$

On the other hand, Eqs. (17), (18) and (29) yield

$$\begin{aligned}\mathbf{M}\Delta\dot{\mathbf{y}}^k &= \mathbf{M}(\ddot{\mathbf{e}}^{k+1}-\ddot{\mathbf{e}}^{k})+\mathbf{M}\Lambda(\dot{\mathbf{e}}^{k+1}-\dot{\mathbf{e}}^{k})\\&=-(\mathbf{N}+\mathbf{N}_1)(\dot{\mathbf{e}}^{k+1}-\dot{\mathbf{e}}^{k})-\mathbf{F}(\mathbf{e}^{k+1}-\mathbf{e}^{k})-(\tau_a^{k+1}-\tau_a^{k})\\&\quad+(\mathbf{d}^{k+1}-\mathbf{d}^{k})+\mathbf{M}\Lambda(\dot{\mathbf{e}}^{k+1}-\dot{\mathbf{e}}^{k})\end{aligned}\tag{30}$$

Substituting Eqs. (18) and (28) into Eq. (30), we have

$$\begin{aligned}\mathbf{K}_d^{k+1}\mathbf{y}^k &= \mathbf{K}_d^{k+1}\mathbf{y}^{k+1}-\mathbf{K}_d^{k+1}\Delta\mathbf{y}^k\\&=-(\mathbf{N}+\mathbf{N}_1)\Delta\dot{\mathbf{e}}^k-\mathbf{F}\Delta\mathbf{e}^k+\Delta\mathbf{d}^k+\mathbf{M}\Lambda\Delta\dot{\mathbf{e}}^k-\mathbf{M}\Delta\dot{\mathbf{y}}^k\\&\quad-f\cdot\mathrm{sgn}((\Delta\mathbf{y}^k)^{\mathrm{T}})-\mathbf{K}_d^{k+1}\Delta\mathbf{y}^k\\&=-(\mathbf{N}+\mathbf{N}_1-\mathbf{M}\Lambda+\mathbf{K}_d^{k+1})\Delta\mathbf{y}^k-(\mathbf{F}-\Lambda(\mathbf{N}+\mathbf{N}_1-\mathbf{M}\Lambda))\Delta\mathbf{e}^k\\&\quad-\mathbf{M}\Delta\dot{\mathbf{y}}^k-f\cdot\mathrm{sgn}((\Delta\mathbf{y}^k)^{\mathrm{T}})+\Delta\mathbf{d}^k\end{aligned}\tag{31}$$

Define $\Delta\mathbf{V}^k=\mathbf{V}^{k+1}-\mathbf{V}^k$. From Eqs. (18) and (23), we obtain

$$\begin{aligned}\Delta\mathbf{V}^k &= \int_0^t \mathbf{e}^{-\rho\mu}[(\mathbf{y}^{k+1})^{\mathrm{T}}\mathbf{K}_d^0\mathbf{y}^{k+1}-(\mathbf{y}^k)^{\mathrm{T}}\mathbf{K}_d^0\mathbf{y}^k]d\mu\\&=\int_0^t \mathbf{e}^{-\rho\mu}[(\Delta\mathbf{y}^k)^{\mathrm{T}}\mathbf{K}_d^0\Delta\mathbf{y}^k+2(\Delta\mathbf{y}^k)^{\mathrm{T}}\mathbf{K}_d^0\mathbf{y}^k]d\mu\\&=\frac{1}{\beta(k+1)}\int_0^t \mathbf{e}^{-\rho\mu}[(\Delta\mathbf{y}^k)^{\mathrm{T}}\mathbf{K}_d^{k+1}\Delta\mathbf{y}^k+2(\Delta\mathbf{y}^k)^{\mathrm{T}}\mathbf{K}_d^{k+1}\mathbf{y}^k]d\mu\end{aligned}\tag{32}$$

Substituting Eq. (31) into Eq. (32), we have Eq. (33).

$$\begin{aligned}\Delta\mathbf{V}^k &= \frac{1}{\beta(k+1)}\int_0^t \mathbf{e}^{-\rho\mu}[(\Delta\mathbf{y}^k)^{\mathrm{T}}\mathbf{K}_d^{k+1}\Delta\mathbf{y}^k+2(\Delta\mathbf{y}^k)^{\mathrm{T}}\mathbf{K}_d^{k+1}\mathbf{y}^k]d\mu\\&=\frac{1}{\beta(k+1)}\left\{\int_0^t \mathbf{e}^{-\rho\mu}(\Delta\mathbf{y}^k)^{\mathrm{T}}\mathbf{K}_d^{k+1}\Delta\mathbf{y}^kd\mu-2\int_0^t \mathbf{e}^{-\rho\mu}(\Delta\mathbf{y}^k)^{\mathrm{T}}\mathbf{M}\Delta\dot{\mathbf{y}}^kd\mu\right.\\&\quad-2\int_0^t e^{-\rho\mu}(\Delta\mathbf{y}^k)^{\mathrm{T}}[(\mathbf{N}+\mathbf{N}_1-\mathbf{M}\Lambda+\mathbf{K}_d^{k+1})\Delta\mathbf{y}^k\\&\quad+(F-\Lambda(\mathbf{N}+\mathbf{N}_1-\mathbf{M}\Lambda))\Delta\mathbf{e}^k+f\cdot\mathrm{sgn}((\Delta\mathbf{y}^k)^{\mathrm{T}})-\Delta\mathbf{d}^k]d\mu\}\end{aligned}\tag{33}$$

Applying the integration by parts and from Assumption 2, one can get

$$\begin{aligned}&\int_0^t \mathbf{e}^{-\rho\mu}(\Delta\mathbf{y}^k)^{\mathrm{T}}\mathbf{M}\Delta\dot{\mathbf{y}}^kd\mu\\&\quad=\mathbf{e}^{-\rho\mu}(\Delta\mathbf{y}^k)^{\mathrm{T}}\mathbf{M}\Delta\mathbf{y}^k|_0^t-\int_0^t(\mathbf{e}^{-\rho\mu}(\Delta\mathbf{y}^k)^{\mathrm{T}}\mathbf{M})'\Delta\mathbf{y}^kd\mu\\&\quad=\mathbf{e}^{-\rho t}(\Delta\mathbf{y}^k)^{\mathrm{T}}\mathbf{M}\Delta\mathbf{y}^k+\rho\int_0^t \mathbf{e}^{-\rho\mu}(\Delta\mathbf{y}^k)^{\mathrm{T}}\mathbf{M}\Delta\mathbf{y}^kd\mu\\&\qquad-\int_0^t \mathbf{e}^{-\rho\mu}(\Delta\dot{\mathbf{y}}^k)^{\mathrm{T}}\mathbf{M}\Delta\mathbf{y}^kd\mu-\int_0^t \mathbf{e}^{-\rho\mu}(\Delta\mathbf{y}^k)^{\mathrm{T}}\dot{\mathbf{M}}\Delta\mathbf{y}^kd\mu\end{aligned}\tag{34}$$

Substituting Eq. (34) into Eq. (33) and from Property 2, we obtain Eq. (35).

$$\begin{aligned}\Delta\mathbf{V}^k &= \frac{1}{\beta(k+1)}\left\{-\mathbf{e}^{-\rho t}(\Delta\mathbf{y}^k)^{\mathrm{T}}\mathbf{M}\Delta\mathbf{y}^k-\rho\int_0^t \mathbf{e}^{-\rho\mu}(\Delta\mathbf{y}^k)^{\mathrm{T}}\mathbf{M}\Delta\mathbf{y}^kd\mu\right.\\&\quad-\int_0^t \mathbf{e}^{-\rho\mu}(\Delta\mathbf{y}^k)^{\mathrm{T}}(\mathbf{K}_d^{k+1}+2\mathbf{N}_1-2\mathbf{M}\Lambda)\Delta\mathbf{y}^kd\mu\\&\quad-2\int_0^t \mathbf{e}^{-\rho\mu}(\Delta\mathbf{y}^k)^{\mathrm{T}}(\mathbf{F}-\Lambda(\mathbf{N}+\mathbf{N}_1-\mathbf{M}\Lambda))\Delta\mathbf{e}^kd\mu\\&\quad\left.-2\int_0^t \mathbf{e}^{-\rho\mu}(\Delta\mathbf{y}^k)^{\mathrm{T}}[f\cdot\mathrm{sgn}((\Delta\mathbf{y}^k)^{\mathrm{T}})-\Delta\mathbf{d}^k]d\mu\right\}\end{aligned}\tag{35}$$

From Eq. (16), we have

$$\begin{aligned}\int_0^t \mathbf{e}^{-\rho\mu}(\Delta\mathbf{y}^k)^{\mathrm{T}}\mathbf{K}_d^{k+1}\Delta\mathbf{y}^kd\mu &= \beta(k+1)\int_0^t \mathbf{e}^{-\rho\mu}(\Delta\mathbf{y}^k)^{\mathrm{T}}\mathbf{K}_d^0\Delta\mathbf{y}^kd\mu\\&\geq\int_0^t \mathbf{e}^{-\rho\mu}(\Delta\mathbf{y}^k)^{\mathrm{T}}\mathbf{K}_d^0\Delta\mathbf{y}^kd\mu\end{aligned}\tag{36}$$

Substituting Eq. (18) into Eq. (35) and using Eq. (36), we get Eq. (37)

$$\begin{aligned}\Delta\mathbf{V}^k \le \frac{1}{\beta(k+1)}\Bigg\{&-\mathbf{e}^{-\rho t}(\Delta\mathbf{y}^k)^{\mathrm{T}}\mathbf{M}\Delta\mathbf{y}^k-\rho\int_0^t \mathbf{e}^{-\rho\mu}(\Delta\mathbf{y}^k)^{\mathrm{T}}\mathbf{M}\Delta\mathbf{y}^k d\mu\\
&-\int_0^t \mathbf{e}^{-\rho\mu}(\Delta\dot{\mathbf{e}}^k)^{\mathrm{T}}(\mathbf{K}_d^0+2\mathbf{N}_1-2\mathbf{M}\Lambda)\Delta\dot{\mathbf{e}}^k d\mu\\
&-2\Lambda\int_0^t \mathbf{e}^{-\rho\mu}(\Delta\mathbf{e}^k)^{\mathrm{T}}(\mathbf{K}_d^0+2\mathbf{N}_1-2\mathbf{M}\Lambda)\Delta\dot{\mathbf{e}}^k d\mu\\
&-\Lambda^2\int_0^t \mathbf{e}^{-\rho\mu}(\Delta\mathbf{e}^k)^{\mathrm{T}}(\mathbf{K}_d^0+2\mathbf{N}_1-2\mathbf{M}\Lambda)\Delta\mathbf{e}^k d\mu\\
&-2\Lambda\int_0^t \mathbf{e}^{-\rho\mu}(\Delta\mathbf{e}^k)^{\mathrm{T}}(\mathbf{F}-\Lambda(\mathbf{N}+\mathbf{N}_1-\mathbf{M}\Lambda))\Delta\mathbf{e}^k d\mu\\
&-2\int_0^t \mathbf{e}^{-\rho\mu}(\Delta\dot{\mathbf{e}}^k)^{\mathrm{T}}(\mathbf{F}-\Lambda(\mathbf{N}+\mathbf{N}_1-\mathbf{M}\Lambda))\Delta\mathbf{e}^k d\mu\\
&-2\int_0^t \mathbf{e}^{-\rho\mu}(\Delta\mathbf{y}^k)^{\mathrm{T}}[f\cdot\mathrm{sgn}((\Delta\mathbf{y}^k)^{\mathrm{T}})-\Delta\mathbf{d}^k]d\mu\Bigg\}\end{aligned} \tag{37}$$

Using the integration by parts, we obtain

$$\begin{aligned}&\int_0^t \mathbf{e}^{-\rho\mu}(\Delta\mathbf{e}^k)^{\mathrm{T}}(\mathbf{K}_d^0+2\mathbf{N}_1-2\mathbf{M}\Lambda)\Delta\dot{\mathbf{e}}^k d\mu\\
&\quad=\mathbf{e}^{-\rho\mu}(\Delta\mathbf{e}^k)^{\mathrm{T}}(\mathbf{K}_d^0+2\mathbf{N}_1-2\mathbf{M}\Lambda)\Delta\mathbf{e}^k|_0^t\\
&\qquad-\int_0^t(\mathbf{e}^{-\rho\mu}(\Delta\mathbf{e}^k)^{\mathrm{T}}(\mathbf{K}_d^0+2\mathbf{N}_1-2\mathbf{M}\Lambda))'\Delta\mathbf{e}^k d\mu\\
&\quad=\mathbf{e}^{-\rho t}(\Delta\mathbf{e}^k)^{\mathrm{T}}(\mathbf{K}_d^0+2\mathbf{N}_1-2\mathbf{M}\Lambda)\Delta\mathbf{e}^k\\
&\qquad+\rho\int_0^t \mathbf{e}^{-\rho\mu}(\Delta\mathbf{e}^k)^{\mathrm{T}}(\mathbf{K}_d^0+2\mathbf{N}_1-2\mathbf{M}\Lambda)\Delta\mathbf{e}^k d\mu\\
&\qquad-\int_0^t \mathbf{e}^{-\rho\mu}(\Delta\dot{\mathbf{e}}^k)^{\mathrm{T}}(\mathbf{K}_d^0+2\mathbf{N}_1-2\mathbf{M}\Lambda)\Delta\mathbf{e}^k d\mu\\
&\qquad-\int_0^t \mathbf{e}^{-\rho\mu}(\Delta\mathbf{e}^k)^{\mathrm{T}}(2\dot{\mathbf{N}}_1-2\dot{\mathbf{M}}\Lambda)\Delta\mathbf{e}^k d\mu\end{aligned} \tag{38}$$

Substituting Eq. (38) into Eq. (37), we have Eq. (39)

$$\begin{aligned}\Delta\mathbf{V}^k \le \frac{1}{\beta(k+1)}\Bigg\{&-\mathbf{e}^{-\rho t}(\Delta\mathbf{y}^k)^{\mathrm{T}}\mathbf{M}\Delta\mathbf{y}^k-\rho\int_0^t \mathbf{e}^{-\rho\mu}(\Delta\mathbf{y}^k)^{\mathrm{T}}\mathbf{M}\Delta\mathbf{y}^k d\mu\\
&-\Lambda\mathbf{e}^{-\rho t}(\Delta\mathbf{e}^k)^{\mathrm{T}}(\mathbf{K}_d^0+2\mathbf{N}_1-2\mathbf{M}\Lambda)\Delta\mathbf{e}^k\\
&-\rho\Lambda\int_0^t \mathbf{e}^{-\rho\mu}(\Delta\mathbf{e}^k)^{\mathrm{T}}(\mathbf{K}_d^0+2\mathbf{N}_1-2\mathbf{M}\Lambda)\Delta\mathbf{e}^k d\mu\\
&-\Lambda\int_0^t \mathbf{e}^{-\rho\mu}(\Delta\mathbf{e}^k)^{\mathrm{T}}(2\mathbf{F}+2\mathbf{N}\Lambda+\mathbf{K}_d^0\Lambda-2\dot{\mathbf{N}}_1)\Delta\mathbf{e}^k d\mu\\
&-\int_0^t \mathbf{e}^{-\rho\mu}(\Delta\dot{\mathbf{e}}^k)^{\mathrm{T}}(\mathbf{K}_d^0+2\mathbf{N}_1-2\mathbf{M}\Lambda)\Delta\dot{\mathbf{e}}^k d\mu\\
&-2\int_0^t \mathbf{e}^{-\rho\mu}(\Delta\dot{\mathbf{e}}^k)^{\mathrm{T}}(\mathbf{F}-\Lambda(\mathbf{N}+\mathbf{N}_1-\mathbf{M}\Lambda))\Delta\mathbf{e}^k d\mu\\
&-2\int_0^t \mathbf{e}^{-\rho\mu}(\Delta\mathbf{y}^k)^{\mathrm{T}}[f\cdot\mathrm{sgn}((\Delta\mathbf{y}^k)^{\mathrm{T}})-\Delta\mathbf{d}^k]d\mu\Bigg\}\end{aligned} \tag{39}$$

From Eqs. (19) and (20),

$$\begin{aligned}\Delta\mathbf{V}^k \le \frac{1}{\beta(k+1)}\{&-\mathbf{e}^{-\rho t}(\Delta\mathbf{y}^k)^{\mathrm{T}}\mathbf{M}\Delta\mathbf{y}^k\\
&-\rho\int_0^t \mathbf{e}^{-\rho\mu}(\Delta\mathbf{y}^k)^{\mathrm{T}}\mathbf{M}\Delta\mathbf{y}^k d\mu-\Lambda\mathbf{e}^{-\rho t}(\Delta\mathbf{e}^k)^{\mathrm{T}}l_1\Delta\mathbf{e}^k\\
&-\rho\Lambda\int_0^t \mathbf{e}^{-\rho\mu}(\Delta\mathbf{e}^k)^{\mathrm{T}}l_1\Delta\mathbf{e}^k d\mu-\mathbf{W}\\
&-2\int_0^t \mathbf{e}^{-\rho\mu}(\Delta\mathbf{y}^k)^{\mathrm{T}}[f\cdot\mathrm{sgn}((\Delta\mathbf{y}^k)^{\mathrm{T}})-\Delta\mathbf{d}^k]d\mu\Bigg\}\end{aligned} \tag{40}$$

where

$$\begin{aligned}\mathbf{W} = &\ \Lambda\int_0^t \mathbf{e}^{-\rho\mu}(\Delta\mathbf{e}^k)^{\mathrm{T}}(2\mathbf{F}+2\mathbf{N}\Lambda+\mathbf{K}_d^0\Lambda-2\dot{\mathbf{N}}_1)\Delta\mathbf{e}^k d\mu\\
&+\int_0^t \mathbf{e}^{-\rho\mu}(\Delta\dot{\mathbf{e}}^k)^{\mathrm{T}}(\mathbf{K}_d^0+2\mathbf{N}_1-2\mathbf{M}\Lambda)\Delta\dot{\mathbf{e}}^k d\mu\\
&+2\int_0^t \mathbf{e}^{-\rho\mu}(\Delta\dot{\mathbf{e}}^k)^{\mathrm{T}}(\mathbf{F}-\Lambda(\mathbf{N}+\mathbf{N}_1-\mathbf{M}\Lambda))\Delta\mathbf{e}^k d\mu\end{aligned}$$

Let $\mathbf{P}=\mathbf{F}-\Lambda(\mathbf{N}+\mathbf{N}_1-\mathbf{M}\Lambda)$, therefore

$$\mathbf{W} \geq \int_0^t \mathbf{e}^{-\rho\mu}(l_1\|\dot{\mathbf{e}}^k\|^2 + 2(\dot{\mathbf{e}}^k)^{\mathrm{T}}\mathbf{P}\mathbf{e}^k + l_2\|\mathbf{e}^k\|^2)d\mu \tag{41}$$

Applying the Cauchy–Schwartz inequality gives

$$(\dot{\mathbf{e}}^k)^{\mathrm{T}}\mathbf{P}\mathbf{e}^k \geq -\|\dot{\mathbf{e}}^k\|\cdot\|\mathbf{P}\|_{\max}\cdot\|\mathbf{e}^k\| \tag{42}$$

Utilizing Eqs. (19)–(21), we got

$$\begin{aligned}\mathbf{W} &\geq \int_0^t \mathbf{e}^{-\rho\mu}(l_1\|\dot{\mathbf{e}}^k\|^2 - 2\|\dot{\mathbf{e}}^k\|\cdot\|\mathbf{P}\|_{\max}\cdot\|\mathbf{e}^k\| + l_2\|\mathbf{e}^k\|^2)d\mu\\ &= \int_0^t \mathbf{e}^{-\rho\mu}\left[l_1\left(\|\dot{\mathbf{e}}^k\| - \frac{1}{l_1}\|\mathbf{P}\|_{\max}\|\mathbf{e}^k\|\right)^2 + \left(l_2 - \frac{1}{l_1}\|\mathbf{P}\|_{\max}^2\right)\|\mathbf{e}^k\|^2\right]d\mu\\ &\geq 0\end{aligned} \tag{43}$$

From Eq. (22), we can obtain $(\Delta\mathbf{y}^k)^{\mathrm{T}}\Delta\mathbf{d}^k \leq \|(\Delta\mathbf{y}^k)^{\mathrm{T}}\|\cdot\|\Delta\mathbf{d}^k\|$, therefore,

$$(\Delta\mathbf{y}^k)^{\mathrm{T}}(f\cdot\mathrm{sgn}((\Delta\mathbf{y}^k)^{\mathrm{T}}) - \Delta\mathbf{d}^k) \geq \|(\Delta\mathbf{y}^k)^{\mathrm{T}}\|\cdot(f - \|\Delta\mathbf{d}^k\|) \tag{44}$$

From Eqs. (40), (43) and (44), we have

$$\Delta\mathbf{V}^k < 0, \quad \text{i. e. ,} \quad \mathbf{V}^{k+1} < \mathbf{V}^k \tag{45}$$

Supplementary material

Supplementary material associated with this article can be found, in the online version, at 10.1016/j.rcim.2019.04.009

References

[1] D. Kang, J. Lee, Analysis of electric machine charateristics for robot eyes using analytical electromagnetic field computation method, IEEE Trans. Magn. 50 (2) (2014) 785–788, https://doi.org/10.1109/TMAG.2013.2278937.

[2] J. Enferadi, A. Shahi, On the position analysis of a new spherical parallel robot with orientation applications, Robot. Comput.-Integr. Manuf. 37 (2016) 151–161, https://doi.org/10.1016/j.rcim.2015.09.004.

[3] T. Li, S. Payandeh, Design of spherical parallel mechanisms for application to laparoscopic surgery, Robotica 20 (02) (2002) 133–138, https://doi.org/10.1017/S0263574701003873.

[4] H.-J. Park, H.-J. Lee, S.-Y. Cho, H.-W. Ahn, K.-D. Lee, C.-Y. Park, S.-H. Won, J. Lee, A performance study on a permanent magnet spherical motor, IEEE Trans. Magn. 49 (5) (2013) 2307–2310, https://doi.org/10.1109/TMAG.2013.2238616.

[5] L. Yan, Z. Wu, Z. Jiao, C.-Y. Chen, I.-M. Chen, Equivalent energized coil model for magnetic field of permanent-magnet spherical actuators, Sens. Actuators A 229 (2015) 68–76, https://doi.org/10.1016/j.ast.2015.11.021.

[6] J. Liu, H. Deng, C. Hu, Z. Hua, W. Chen, Adaptive backstepping sliding mode control for 3-DOF permanent magnet spherical actuator, Aerosp. Sci. Technol. 67 (2017) 62–71, https://doi.org/10.1016/j.ast.2017.03.032.

[7] W. Chen, L. Zhang, L. Yan, J. Liu, Design and control of a three degree-of-freedom permanent magnet spherical actuator, Sens. Actuators A 180 (2012) 75–86, https://doi.org/10.1016/j.sna.2012.04.010.

[8] G. Wu, S. Caro, S. Bai, J. Kepler, Dynamic modeling and design optimization of a 3-DOF spherical parallel manipulator, Robot. Auton. Syst. 62 (10) (2014) 1377–1386, https://doi.org/10.1016/j.robot.2014.06.006.

[9] C.M. Gosselin, J.-F. Hamel, The agile eye: a high-performance three-degree-of-freedom camera-orienting device, Proceedings of the 1994 IEEE International Conference on Robotics and Automation, (1994), pp. 781–786 vol.1, https://doi.org/10.1109/ROBOT.1994.351393.

[10] B. Sudki, M. Lauria, F. Noca, Marine propulsor based on a three-degree-of-freedom actuated spherical joint, Proceedings of the 3rd International Symposium on Marine Propulsors, (2013), pp. 481–485.

[11] C.M. Gosselin, W. Jing, Singularity loci of a special class of spherical three-degree-of-freedom parallel mechanisms with revolute actuators, Int. J. Robot. Res. 21 (7) (2002) 649–660, https://doi.org/10.1177/027836402322023231.

[12] H. Saafi, M.A. Laribi, S. Zeghloul, Redundantly actuated 3-rrr spherical parallel manipulator usedas a haptic device: improving dexterity and eliminating singularity, Robotica 33 (5) (2015) 1113–1130, https://doi.org/10.1017/S0263574714001751.

[13] S. Leguay-Durand, C. Reboulet, Optimal design of a redundant spherical parallel manipulator, Robotica 15 (4) (1997) 399–405, https://doi.org/10.1017/S0263574797000490.

[14] S. Bai, Optimum design of spherical parallel manipulators for a prescribed workspace, Mech. Mach. Theory 45 (2) (2010) 200–211, https://doi.org/10.1016/j.mechmachtheory.2009.06.007.

[15] X. Li, S. Bai, W. Chen, J. Liu, Integrated design and modelling of an electro-magnets driven spherical parallel manipulator, 2017 IEEE International Conference on Advanced Intelligent Mechatronics (AIM), (2017), pp. 1209–1214, https://doi.org/10.1109/AIM.2017.8014183.

[16] X. Li, J. Liu, W. Chen, S. Bai, Integrated design, modeling and analysis of a novel spherical motion generator driven by electromagnetic principle, Robot. Auton. Syst. 106 (2018) 69–81, https://doi.org/10.1016/j.robot.2018.04.006.

[17] H. Son, K.M. Lee, Open-loop controller design and dynamic characteristics of a spherical wheel motor, IEEE Transactions on Industrial Electronics 57 (10) (2010) 3475–3482, https://doi.org/10.1109/TIE.2009.2039454.

[18] Q. Chen, H. Chen, Y. Wang, P.-Y. Woo, Global stability analysis for some trajectory-tracking control schemes of robotic manipulators, J. Robot. Syst. 18 (2) (2001) 69–75 https://10.1002/(SICI)1097-4563(199701)14:1%3C9::AID-ROB2%3E3.0.CO;2-X.

[19] X. Wang, B. Hou, Trajectory tracking control of a 2-dof manipulator using computed torque control combined with an implicit lyapunov function method, J. Mech. Sci. Technol. 32 (6) (2018) 2803–2816, https://doi.org/10.1007/s12206-018-0537-6.

[20] M.I. Ullah, S.A. Ajwad, R.U. Islam, U. Iqbal, J. Iqbal, Modeling and computed torque control of a 6 degree of freedom robotic arm, 2014 International Conference on Robotics and Emerging Allied Technologies in Engineering (iCREATE), (2014), pp. 133–138, https://doi.org/10.1109/iCREATE.2014.6828353.

[21] M. Asgari, M.A. Ardestani, Dynamics and improved computed torque control of a novel medical parallel manipulator: applied to chest compressions to assist in cardiopulmonary resuscitation, J. Mech. Med. Biol. 15 (04) (2015) 1550051, https://doi.org/10.1142/S0219519415500517.

[22] Y. Jia, Robust control with decoupling performance for steering and traction of 4WS vehicles under velocity-varying motion, IEEE Trans. Control Syst. Technol. 8 (3) (2000) 554–569, https://doi.org/10.1109/87.845885.

[23] X. Yin, L. Pan, Enhancing trajectory tracking accuracy for industrial robot with robust adaptive control, Robot. Comput.-Integrated Manuf. 51 (2018) 97–102, https://doi.org/10.1016/j.rcim.2017.11.007.

[24] C. Xia, C. Guo, T. Shi, A neural-network-identifier and fuzzy-controller-based algorithm for dynamic decoupling control of permanent-magnet spherical motor, IEEE Trans. ind. Electron. 57 (8) (2010) 2868–2878, https://doi.org/10.1109/TIE.2009.2036030.

[25] J. Cazalilla, M. Vallés, V. Mata, M. Díaz-Rodríguez, A. Valera, Adaptive control of a 3-DOF parallel manipulator considering payload handling and relevant parameter models, Robot. Comput.-Integr. Manuf. 30 (5) (2014) 468–477, https://doi.org/10.1016/j.rcim.2014.02.003.

[26] X. Wang, H. Deng, Q. Wang, Research of manipulator trajectory tracking based on adaptive robust iterative learning control, Cluster Comput. (2018), https://doi.org/10.1007/s10586-018-1919-3.

[27] T.O. Andersen, H.C. Pedersen, M.R. Hansen, Discrete learning control with application to hydraulic actuators, Model. Identif. Control 36 (4) (2015) 215–224, https://doi.org/10.4173/mic.2015.4.2.

[28] T. Ngo, M.H. Nguyen, Y. Wang, J. Ge, S. Wei, T.L. Mai, An adaptive iterative learning control for robot manipulator in task space, Int. J. Comput. Commun. Control 7 (3) (2012) 518–529, https://doi.org/10.15837/ijccc.2012.3.1392.

[29] C.-J. Chien, A combined adaptive law for fuzzy iterative learning control of nonlinear systems with varying control tasks, IEEE Trans. Fuzzy Syst. 16 (1) (2008) 40–51, https://doi.org/10.1109/TFUZZ.2007.902021.

[30] P.R. Ouyang, W.J. Zhang, M.M. Gupta, An adaptive switching learning control method for trajectory tracking of robot manipulators, Mechatronics 16 (1) (2006) 51–61, https://doi.org/10.1016/j.mechatronics.2005.08.002.

[31] L. Zhang, W. Chen, J. Liu, C. Wen, A robust adaptive iterative learning control for

trajectory tracking of permanent-magnet spherical actuator, IEEE Trans. Ind. Electron. 63 (1) (2016) 291–301, https://doi.org/10.1109/TIE.2015.2464186.

[32] J. Angeles, S. Bai, Some special cases of the Burmester problem for four and five poses, ASME 2005 International Design Engineering Technical Conferences and Computers and Information in Engineering Conference, American Society of Mechanical Engineers, 2005, pp. 307–314, https://doi.org/10.1115/DETC2005-84871.

[33] S.-K. Wang, J.-Z. Wang, J. Zhao, Application of PD-type iterative learning control in hydraulically driven 6-DOF parallel platform, Trans. Inst. Meas. Control 35 (5) (2013) 683–691, https://doi.org/10.1177/0142331212469538.

[34] W.J. Zhang, Q. Li, L.S. Guo, Integrated design of mechanical structure and control algorithm for a programmable four-bar linkage, IEEE/ASME Trans. Mechatron. 4 (4) (1999) 354–362, https://doi.org/10.1109/3516.809514.

[35] P.R. Ouyang, W.J. Zhang, Force balancing of robotic mechanisms based on adjustment of kinematic parameters, J. Mech. Des. 127 (3) (2005) 433–440, https://doi.org/10.1115/1.1864116.

Chapter 5

Paper III

Analytical magnetics and torque modeling of a multi-layer electromagnetic driven spherical motion generator

Xuerong Li, Jingmeng Liu, Weihai Chen and Shaoping Bai

The paper has been published in the
Journal of Magnetism and Magnetic Materials Vol. 493(2020), pp. 165707 1–11,
2020.

Journal of Magnetism and Magnetic Materials 493 (2020) 165707

Contents lists available at ScienceDirect

Journal of Magnetism and Magnetic Materials

journal homepage: www.elsevier.com/locate/jmmm

Research articles

Analytical magnetics and torque modeling of a multi-layer electromagnetic driven spherical motion generator

Xuerong Li[a,b], Jingmeng Liu[b], Weihai Chen[b], Shaoping Bai[a,*]

[a] Department of Materials and Production, Aalborg University, 9220 Aalborg, Denmark
[b] School of Automation Science and Electrical Engineering, Beihang University, 100191 Beijing, China

ARTICLE INFO

Keywords:
Spherical motion generator
Electromagnetic driving system
Magnetic modeling
Torque modeling
Spherical parallel manipulator

ABSTRACT

This paper presents modeling of an integrated design of an electromagnetic driven spherical motion generator with multi-layer structure. An analytical method to calculate the complex magnetic field distribution of the rotor array by combining the equivalent charge model and transformation method is developed, upon which torque model is further established analytically by using the moment principle. Both the analytical magnetic model and torque model are validated with the numerical finite element method by Ansoft Maxwell and experimental measurements. With the model, two different designs of the electromagnetic driven SMGs are analyzed to illustrate the application of the developed model.

1. Introduction

Spherical motion generators (SMG) which can generate multi-degree-of-freedom (DOF) pure rotations are greatly required in many areas such as robot manipulators [1], orientating devices [2,3] and aerospace [4].

So far, various designs of the SMGs have been proposed [5–8], among which spherical parallel manipulators (SPM) and spherical actuators are two typical structures. SPM is a kind of closed-loop mechanism that is consisting of a fixed base and a mobile platform connected by several serial links. SPM is well known for the Agile Eye developed by Gosselin et al. which is first applied in camera orienting devices [9]. SPMs with unlimited rotations were designed with coaxial shafts [10,11]. Compared with the serial mechanism, SPMs have the advantages of higher rigidity, better accuracy and larger load capacity. However, the SPMs are usually actuated by separate motors, which leads to the increment of inertia and the reduction of the feasibility. Another type is the spherical actuator which can generate 3-DOF rotations in one joint [12,13], in particular, the permanent magnet spherical actuator (PMSA). A PMSA composes of a spherical permanent magnet array and a number of stator coils distributed evenly in a spherical shell. By energizing the stator coils with appropriate current control strategies [14], the rotor can be actuated to implement a 3-DOF motion on the sphere. It offers advantages of compact structure, non-contact and gear-less actuation and rapid response, however, the applications of PMSAs are limited by the relatively heavy mass and large size of the rotor arrays. To utilize the mechanical structure of the SPM and the actuating principle of the PMSA, new integrated designs of electromagnetic driven SMG have been proposed. Recently, an electromagnetic driven SMG was introduced in [15,16]. This design has a more compact and light-weight structure with the advantages of no backlash, high stiffness and low inertia. However, the integrated 3-DOF actuation brings in a complicated control system. In this work, an alternative design is proposed, which features with a multi-layer electromagnetic actuation, comparing the single-layer actuation in [15]. The multi-layer design simplifies the control system by separating 3-DOF actuation into three single-axial electromagnetic drive unit. Moreover, the torque output is enhanced due to the introduction of more permanent magnets. On the one hand, the 3-DOF spherical motion within a large workspace can be used for panorama head, gyroscope and so on. On the other hand, the 360° rotational motion can provide rotary propulsion which is required in applications such as propulsion devices [17]. To investigate the structure optimization and further real-time control [18–20], analytical magnetic and torque modeling of the electromagnetic driven SMG with better precision is highly necessary and is also a challenging work.

Analytical magnetic modeling has been investigated adopting methods including spherical harmonics, magnetic equivalent circuit, distributed multipole and charge models. Spherical harmonics (SH) is a method for analyzing the magnetic field distribution of permanent magnet arrays in 3D spherical coordinate [21–23]. Magnetic equivalent circuit (MEC) is employed by meshing the geometry into elements [24].

---

[*] Corresponding author.
E-mail address: shb@mp.aau.dk (S. Bai).

https://doi.org/10.1016/j.jmmm.2019.165707
Received 25 June 2019; Received in revised form 12 August 2019; Accepted 13 August 2019

Distributed multipole (DMP) developed by Lee and Son et al. is applied for rotor array with cylindrical permanent magnets [25,26]. The charge and current models are another type of analytical methods to analyze the air-gap magnetic field of the permanent magnets, in which the PMs are equivalent to a distribution of “magnetic charge” or “current” [27,28].

The electromagnetic torque model is established analytically based on the analytical magnetic distribution results [29]. There are also various approaches that are used for torque analysis. The torque model can be formulated by the conventional Lorentz force law, however, the multiple integration increases the calculation complexity seriously [30]. The virtual-work method analyzes the torque by evaluating the magnetic potential energy of the system [31]. Lim et al. introduce a dipole moment principle to describe and determine resultant torque, which greatly simplifies the computing process [32].

This paper proposes an electromagnetic driven SMG with multi-layer structure that integrates the mechanical structure of SPM and the actuating principle of the PMSAs. The actuating part is constructed by three-layer rotor arrays with 12 tile-shaped PMs in total, and 18 surrounding stator coils. The objective of this paper is to develop analytical magnetic field and torque models for design analysis of the SMG. The proposed magnetic modeling method is based on the equivalent charge model. The torque performance is analyzed by the dipole moment principle. Compared with the conventional Lorentz force law, the moment analysis reduces the computational complexity of the integral function.

The rest of the paper is organized as follows. Section 2 presents the design and working principle of the SMG. Section 3 formulates the analytical model of the magnetic field distribution of PM rotor array in the air gap. Section 4 presents the torque model that is formulated using the moment principle. Section 5 describes the simulation and experimental results on magnetic field distribution and torque model to validate the analytical models. The validated models are used to compare and analyze the performance of the two designs of SMGs. Finally, the paper is concluded in Section 6.

2. Two designs of SMGs

2.1. Conceptual design of a multi-layer SMG

The conceptual design of multi-layer SMG is shown in Fig. 1. It is mainly constructed in two parts: a spherical parallel kinematic mechanism (SPKM) and an electromagnetic driver. The SPKM is a type of spherical parallel manipulators with coaxial shafts which is first developed by Asada [6]. It is a closed loop mechanism consisting of three serial chains with coaxial input shafts and an output mobile platform. Each serial chain that is connected to the mobile platform has three revolute joints whose axe are denoted by unit vectors $\mathbf{u}_i$, $\mathbf{v}_i$ and $\mathbf{w}_i$, $i = 1, 2, 3$. All the joints intersect at the spherical center **O** as shown in Fig. 2. The kinematics and dynamics of the spherical parallel manipulator that have been well-documented in [15,33] will not be repeated in detail in this section.

We define the generalized coordinates of the manipulator:

$$\mathbf{q} = \begin{bmatrix} \mathbf{q}_a \\ \mathbf{q}_e \end{bmatrix} \tag{1}$$

where $\mathbf{q}_a = [\theta_1 \ \ \theta_2 \ \ \theta_3]^{\mathrm{T}}$ is the vector of the actuated joint angles and $\mathbf{q}_e = [\phi \ \ \theta \ \ \sigma]^{\mathrm{T}}$ is the vector of X-Y-Z Euler angles of the mobile platform. By actuating the three proximal links with different input joint angles $\mathbf{q}_a$, a 3-DOF rotation will be generated at the end-effector of the mobile platform with $\mathbf{q}_e$. The actuation of the input joint angles is implemented by the electromagnetic driving system.

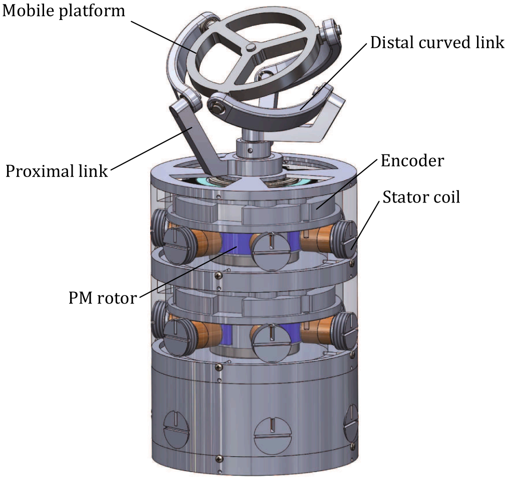

(a) CAD model

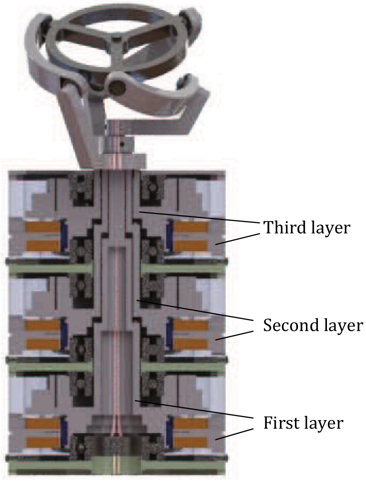

(b) Cross-section view

Fig. 1. Conceptual design of multi-layer SMG.

The electromagnetic driven part consists of permanent magnet rotor arrays and stators in three layers as illustrated in Fig. 1(b), which are used for actuating three proximal links, respectively. The actuating principle of the SMG is shown as Fig. 3. For each layer, the rotor array is constructed by four tile-shaped PMs that are symmetrically distributed on the rotor surface and there are six stator coils mounted on the outer stator shell. The proximal link’s rotational motion around the shaft is generated by the repelling and attracting electromagnetic forces between the rotor PM poles and the stator coils. When all the proximal links are actuated with equal torques continuously, the end-effector can spin about its own axis. Alternatively, the proximal links can be driven with different torques, the SMG will produce 3D motion at the end-effector.

2.2. Single-layer SMG design

We briefly describe the design presented in [15]. As shown in Fig. 4,

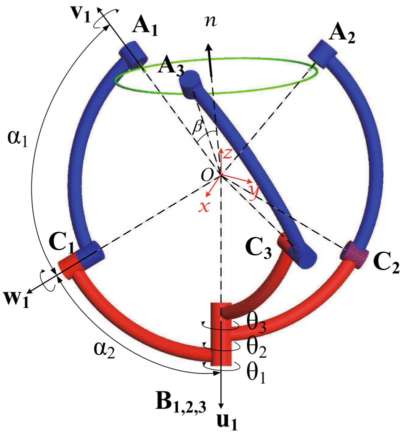

Fig. 2. Kinematics of spherical parallel manipulator with coaxial shafts.

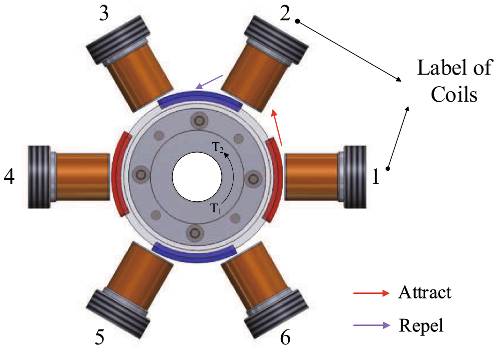

Fig. 3. Actuating principle of multi-layer SMG.

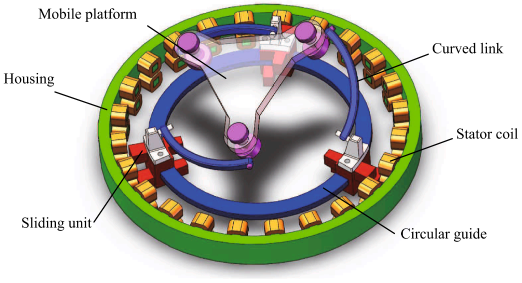

Fig. 4. Integrated design of single-layer SMG.

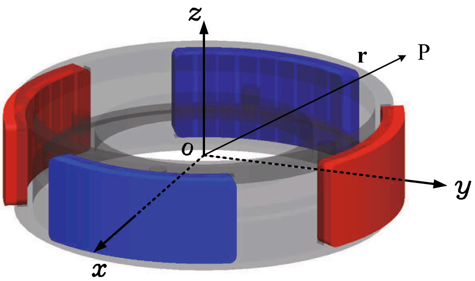

Fig. 5. Permanent magnet rotor array.

the SMG is a single-layer electromagnetic driven spherical motor. For clarity, we refer hereafter to the two designs with single and multi-layers as O- and I-shape SMGs, respectively. The SPKM is a special case of the kinematics in Fig. 2, which is based on the design in [33]. Three proximal links are replaced by three identical sliding units which can move smoothly around the fixed circular guide. Generally, the sliding units are actuated by three attached motors and the motion is transmitted by the gear drive. In our study, every sliding unit is constructed by PM poles, and double-layer stator coils are distributed equally on the cylindrical housing. Through varying the current inputs of the stator coils, the sliding units are actuated separately by the shared stator coils.

The multi-layer design of SMG proposed in this work, compared with the single-layer one, allows higher torque outputs and simpler control of system. A more detailed comparison can be found in Section 5.3.

3. Magnetic field distribution

The rotor structure is constructed by three layers' permanent magnet arrays. Each PM array consists of four tile-shaped permanent magnets that are distributed equally. The PMs are uniformly magnetized with alternative variation of N and S poles as shown in Fig. 5. The specific magnetization axis of l^{th} PM pole in the global rotor coordinate is given by the unit vector

$$\mathbf{r}_l = \begin{bmatrix} x_l \\ y_l \\ z_l \end{bmatrix} = (-1)^l \begin{bmatrix} \cos(\phi_l) \\ \sin(\phi_l) \\ 0 \end{bmatrix} \tag{2}$$

where $\phi_l = \frac{2\pi}{\text{L}}(l-1),\quad l = 1, 2, \ldots, \text{L}$ and L is the number of PM poles. To analyze the air-gap magnetic field distribution of the rotor array at point **P** in the global rotor coordinate, every PM pole is modeled separately in its local coordinate system first.

3.1. The equivalent magnetic charge model

The magnetic field of a single PM pole is modeled analytically using the equivalent magnetic charge method. The derivation of the charge model starts with the magnetostatic field equations for current-free regions,

$$\nabla \times \mathbf{H} = \mathbf{0} \tag{3}$$

$$\nabla \cdot \mathbf{B} = 0 \tag{4}$$

where **H** is the magnetic field strength and **B** is the magnetic flux density. The magnetic field strength, **H** in Eq. (3) can be expressed as the divergence of the magnetic scalar potential φ

$$\mathbf{H} = -\nabla \cdot \varphi \tag{5}$$

The constitutive relation is

$$\mathbf{B} = \mu_0(\mathbf{H} + \mathbf{M}) \tag{6}$$

Substituting Eqs. (5) and (6) into Eq. (4)

$$\nabla^2 \cdot \varphi = \nabla \cdot \mathbf{M} \tag{7}$$

Eq. (7) can be formulated in integral form by using the free space Green's function

$$\mathbf{G}(\mathbf{r}, \mathbf{r}') = -\frac{\mathbf{1}}{\mathbf{4}\pi|\mathbf{r} - \mathbf{r}'|} \tag{8}$$

Then, we obtain

$$\varphi(\mathbf{r}) = -\frac{1}{4\pi}\int \frac{\nabla\cdot\mathbf{M}}{|\mathbf{r}-\mathbf{r}'|}dV' \tag{9}$$

where $\mathbf{r}'$ and $\mathbf{r}$ represent the position vector of the source point $\mathbf{P}'$ and the observation point $\mathbf{P}$, respectively. If the magnetization $\mathbf{M}$ is confined to a volume V (of permeability μ_0), and falls abruptly to zero outside of V, then Eq. (9) reduces to

$$\varphi(\mathbf{r}) = \frac{1}{4\pi}\int_V \frac{\mathbf{J}_m(\mathbf{r}')}{|\mathbf{r}-\mathbf{r}'|}dV' + \frac{1}{4\pi}\oint_s \frac{\mathbf{j}_m(\mathbf{r}')}{|\mathbf{r}-\mathbf{r}'|}ds' \tag{10}$$

where S is the surface of the magnet, and $\mathbf{J}_m$ and $\mathbf{j}_m$ are equivalent volume and surface current densities

$$\mathbf{J}_m = -\nabla'\cdot\mathbf{M}\,(\mathrm{A/m^2}),\ \mathbf{j}_m = \mathbf{M}\cdot\hat{\mathbf{d}}\,(\mathrm{A/m}) \tag{11}$$

where $\hat{\mathbf{d}}$ is the unit surface normals. The magnet is in free space, $\mathbf{B} = \mu_0\mathbf{H}$ and from Eqs. (5) and (10), we have

$$\mathbf{B}(\mathbf{r}) = \frac{\mu_0}{4\pi}\int_V \frac{\mathbf{J}_m(\mathbf{r}')(\mathbf{r}-\mathbf{r}')}{|\mathbf{r}-\mathbf{r}'|^3}dV' + \frac{\mu_0}{4\pi}\oint_s \frac{\mathbf{j}_m(\mathbf{r}')(\mathbf{r}-\mathbf{r}')}{|\mathbf{r}-\mathbf{r}'|^3}ds' \tag{12}$$

3.2. Magnetic field analysis of a single tile-shaped PM pole with parallel magnetization

The single permanent magnet of the rotor is analyzed using equivalent charge magnetic method first. To simplify the magnetic modeling of tile-shaped permanent magnets, an equivalent subdivision method is introduced. The tile-shaped magnet can be divided into numerous small tile-shaped permanent magnet poles of circumferential arrangement in space. Each small tile-shaped permanent magnet pole can be equivalent as two cuboid magnets. Then the magnetic field distribution of one tile-shaped magnet is obtained by superposition of magnetic field generated by all the equivalent cuboid PM poles.

The tile-shaped PM poles with parallel magnetization ${}^{(l)}\mathbf{M}$ along x_l-axis in its local coordinate is shown in Fig. 6(a), and the magnetization is formulated as follows:

$${}^{(l)}\mathbf{M} = (-1)^{l-1}M_s\cdot\hat{\mathbf{x}}_l,\quad l = 1,\ 2\ldots,4 \tag{13}$$

From Eq. (11), we obtain that the volume current density is

$${}^{(l)}\mathbf{J}_m = -\nabla'\cdot{}^{(l)}\mathbf{M} = \mathbf{0} \tag{14}$$

Then the charge model of the PM pole Eq. (12) in l^{th} local coordinate can be reformulated as

$${}^{(l)}\mathbf{B}({}^{(l)}\mathbf{r}) = \frac{\mu_0}{4\pi}\oint_s \frac{{}^{(l)}\mathbf{j}_m(\mathbf{r}')({}^{(l)}\mathbf{r}-\mathbf{r}')}{|{}^{(l)}\mathbf{r}-\mathbf{r}'|^3}ds' \tag{15}$$

The PM pole is subdivided uniformly into $2N+1$ small tile-shaped PM elements, with the specific subdivision schematic shown in Fig. 6(b). Every PM element is also modeled analytically in its subordinative frame $O - xyz_{l,n}$. For simplifying the calculation, the tile-shaped PM element can be equivalent to cuboid magnets which is easy to be analyzed using the equivalent charge method. For any PM element, it is polarized with the magnetization along x_l-axis. When the PM is transformed to its subordinate frame, the magnetization along the x-axis of the l^{th} local coordinate can be decomposed into longitudinal magnetization along $x_{l,n}$-axis and lateral magnetization along $y_{l,n}$-axis based on the subordinate frame, which is shown in Fig. 7.

In the subordinate frame, the longitudinal and lateral magnetizations are defined as

$$\begin{aligned}{}^{(l,n)}\mathbf{M}_r &={}^{(l)}\ \mathbf{M}\cos(\phi_{l,n}) = (-1)^{(l-1)}\cdot M_s\cos(\phi_{l,n})\cdot\hat{\mathbf{x}}_{l,n} ={}^{(l,n)}\ M_r\hat{\mathbf{x}}_{l,n}\\ {}^{(l,n)}\mathbf{M}_e &= -{}^{(l)}\mathbf{M}\sin(\phi_{l,n}) = (-1)^{l}\cdot M_s\sin(\phi_{l,n})\cdot\hat{\mathbf{y}}_{l,n} ={}^{(l,n)}\ M_e\hat{\mathbf{y}}_{l,n}\end{aligned} \tag{16}$$

To evaluate the surface term ${}^{(l,n)}\mathbf{j}_m$, we first evaluate the unit surface normals

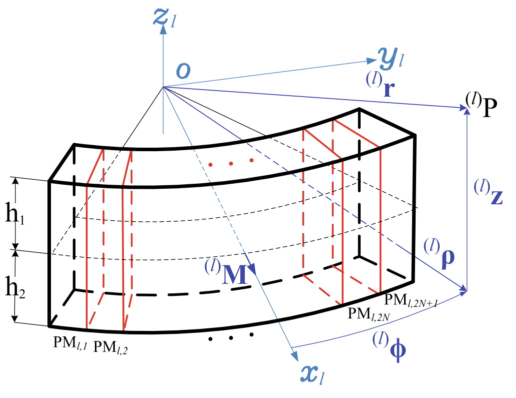

(a) Tile-shaped PM pole in its local coordinate

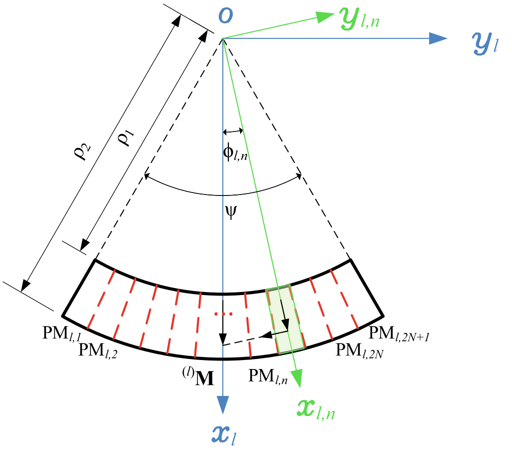

(b) View of the PM pole from XY-plane

Fig. 6. A single PM in l^{th} local coordinate.

$$\hat{\mathbf{d}}' = \begin{cases}\mathbf{d}_1 = -\hat{\mathbf{x}}_{l,n}, & x' = \rho_1\\ \mathbf{d}_2 = \hat{\mathbf{x}}_{l,n}, & x' = \rho_2\\ \mathbf{d}_3 = \hat{\mathbf{y}}_{l,n}, & x' = b_1\\ \mathbf{d}_4 = -\hat{\mathbf{y}}_{l,n}, & x' = b_2\\ \mathbf{d}_5 = \hat{\mathbf{z}}_{l,n}, & z' = h_1\\ \mathbf{d}_6 = -\hat{\mathbf{z}}_{l,n}, & z' = h_2\end{cases} \tag{17}$$

From Eq. (17) and the fact that $\mathbf{j}_m = \mathbf{M}\cdot\hat{\mathbf{d}}$, we have the longitudinal surface density ${}^{(l,n)}\mathbf{j}_{mr} = (-1)^{(l-1)}\cdot M_s\cos(\phi_{l,n})\hat{\mathbf{x}}_{l,n}$ on the front surface ($\mathbf{x}_{l,n} = \rho_2$), ${}^{(l,n)}\mathbf{j}_{mr} = (-1)^{l}\cdot M_s\cos(\phi_{l,n})\hat{\mathbf{x}}_{l,n}$ from the back surface ($\mathbf{x}_{l,n} = \rho_1$). Furthermore, we have the lateral surface density ${}^{(l,n)}\mathbf{j}_{me} = (-1)^{(l-1)}\cdot M_s\sin(\phi_{l,n})\hat{\mathbf{y}}_{l,n}$ on the left surface ($\mathbf{y}_{l,n} = b_2$), and ${}^{(l,n)}\mathbf{j}_{me} = (-1)^{l}\cdot M_s\sin(\phi_{l,n})\hat{\mathbf{y}}_{l,n}$ on the right surface ($\mathbf{y}_{l,n} = b_1$). In the subordinate frame $O - (xyz)_{l,n}$, the distance between the source point $\mathbf{P}'$ and the observation point ${}^{(l,n)}\mathbf{P}$ is given by

$${}^{(l,n)}\mathbf{r}_p - \mathbf{r}' = ({}^{(l,n)}X_p - x')\hat{\mathbf{x}}_{l,n} + ({}^{(l,n)}Y_p - y')\hat{\mathbf{y}}_{l,n} + ({}^{(l,n)}Z_p - z')\hat{\mathbf{z}}_{l,n} \tag{18}$$

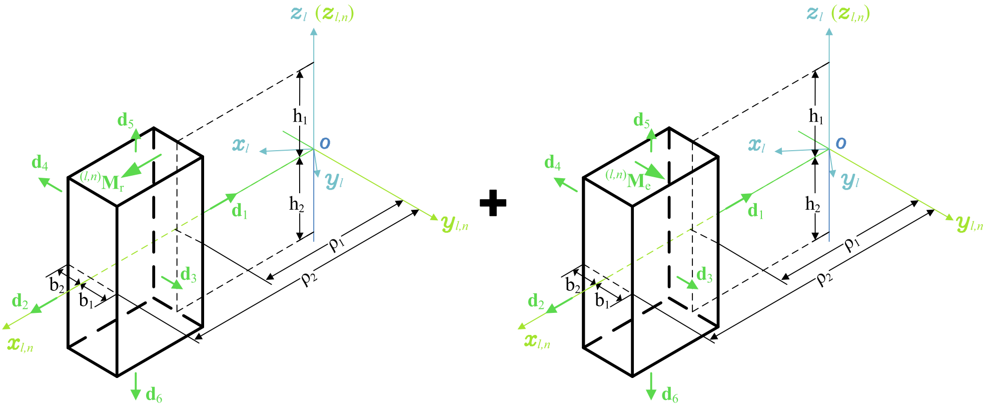

Fig. 7. Equivalent model of a small tile-shaped PM element.

According to Eq. (15), the magnetic field distribution in the air gap can be obtained:

$$
{}^{(l,n)}\mathbf{B}({}^{(l,n)}\mathbf{r}_p) = \frac{\mu_0}{4\pi}\oint_s \left[\frac{{}^{(l,n)}\mathbf{j}_{mr}(\mathbf{r}')({}^{(l,n)}\mathbf{r}_p - \mathbf{r}')}{|{}^{(l,n)}\mathbf{r}_p - \mathbf{r}'|^3} + \frac{{}^{(l,n)}\mathbf{j}_{me}(\mathbf{r}')({}^{(l,n)}\mathbf{r}_p - \mathbf{r}')}{|{}^{(l,n)}\mathbf{r}_p - \mathbf{r}'|^3} \right] ds' \tag{19}
$$

which is further expanded as

$$
\begin{aligned}
&{}^{(l,n)}\mathbf{B}({}^{(l,n)}\mathbf{r}_p) \\
&= \sum_{k=1}^{2} \frac{\mu_0}{4\pi} \int_{h_2}^{h_1} \int_{b_2}^{b_1} \frac{(-1)^{k}\cdot {}^{(l,n)}M_r \mathbf{Q}_{rk}}{[({}^{(l,n)}X_p - \rho_k)^2 + ({}^{(l,n)}Y_p - y')^2 + ({}^{(l,n)}Z_p - z')^2]^{\frac{3}{2}}} \\
&\quad dy'dz' - \sum_{k=1}^{2} \frac{\mu_0}{4\pi} \int_{h_2}^{h_1} \\
&\quad \int_{\rho_2}^{\rho_1} \frac{(-1)^{k}\cdot {}^{(l,n)}M_e \mathbf{Q}_{ek}}{[({}^{(l,n)}X_p - x')^2 + ({}^{(l,n)}Y_p - b_k)^2 + ({}^{(l,n)}Z_p - z')^2]^{\frac{3}{2}}} dx'dz'
\end{aligned} \tag{20}
$$

where $\mathbf{Q}_{rk} = ({}^{(l,n)}X_p - \rho_k)\cdot {}^{(l,n)}\hat{\mathbf{x}} + ({}^{(l,n)}Y_p - y')\cdot {}^{(l,n)}\hat{\mathbf{y}} + ({}^{(l,n)}Z_p - z')\cdot {}^{(l,n)}\hat{\mathbf{z}}$ and $\mathbf{Q}_{ek} = ({}^{(l,n)}X_p - x')\cdot {}^{(l,n)}\hat{\mathbf{x}} + ({}^{(l,n)}Y_p - b_k)\cdot {}^{(l,n)}\hat{\mathbf{y}} + ({}^{(l,n)}Z_p - z')\cdot {}^{(l,n)}\hat{\mathbf{z}}$. By calculation, the magnetic flux density of the equivalent cuboid PM poles in the l^{th} coordinate are obtained:

$$
{}^{(l)}\mathbf{B}_x = {}^{(l)}\hat{\mathbf{x}} \sum_{n=0}^{2N+1} [{}^{(l,n)}B_x({}^{(l,n)}\mathbf{r}_p)\cos(\phi_l) + {}^{(l,n)}B_y({}^{(l,n)}\mathbf{r}_p)\sin(\phi_l)] \tag{21}
$$

$$
{}^{(l)}\mathbf{B}_y ={}^{(l)} \hat{\boldsymbol{y}} \sum_{n=0}^{2N+1} [-{}^{(l,n)} B_x({}^{(l,n)}\mathbf{r}_p)\sin(\phi_l) +{}^{(l,n)} B_y({}^{(l,n)}\mathbf{r}_p)\cos(\phi_l)] \tag{22}
$$

$$
{}^{(l)}\mathbf{B}_z = {}^{(l)}\hat{\mathbf{z}} \sum_{n=0}^{2N+1} {}^{(l,n)}B_z({}^{(l,n)}\mathbf{r}_p) \tag{23}
$$

3.3. Magnetic field distribution of rotor structure in global coordinate system

The complete magnetic field distribution of the 3D magnetic array in global rotor coordinate is obtained by superposition of all PM poles that are rotated and transformed from corresponding local coordinate system. The computation of the 3D magnetic flux density in global coordinate system are described as follows.

First, the position of a point **P** in global Cartesian coordinate system is expressed as

$$
\mathbf{r}_p = \begin{bmatrix} X_p \\ Y_p \\ Z_p \end{bmatrix} = \begin{bmatrix} \rho_p\cos(\phi_p) \\ \rho_p\sin(\phi_p) \\ Z_p \end{bmatrix} \tag{24}
$$

Afterwards, the global coordinates of **P** are transformed into the local coordinate system of the l^{th} permanent magnet by rotation matrix from global frame to l^{th} local frame ${}^{(l)}\mathbf{R}$ which is given by

$$
{}^{(l)}\mathbf{R} = \mathbf{R}_z(\phi_l) = \begin{bmatrix} \cos(\phi_l) & \sin(\phi_l) & 0 \\ -\sin(\phi_l) & \cos(\phi_l) & 0 \\ 0 & 0 & 1 \end{bmatrix} \tag{25}
$$

The local coordinates of **P** expressed in the l^{th} local coordinate system is obtained

$$
{}^{(l)}\mathbf{r} = \begin{bmatrix} {}^{(l)}X_p \\ {}^{(l)}Y_p \\ {}^{(l)}Z_p \end{bmatrix} = {}^{(l)}\mathbf{R}\cdot{}^{(l)}\mathbf{r}_p = \begin{bmatrix} \cos(\phi_l) & \sin(\phi_l) & 0 \\ -\sin(\phi_l) & \cos(\phi_l) & 0 \\ 0 & 0 & 1 \end{bmatrix} \begin{bmatrix} X_p \\ Y_p \\ Z_p \end{bmatrix} \tag{26}
$$

The magnetic field distribution of the point **P** in l^{th} local Cartesian coordinate system are formulated according to Eqs. (21)–(23). After that, we calculate the magnetic field distribution of point **P** in l^{th} local cylindrical coordinate system

$$
\begin{aligned}
{}^{(l)}\mathbf{B}({}^{(l)}\mathbf{r}) &= \begin{bmatrix} {}^{(l)}B_\rho \\ {}^{(l)}B_\phi \\ {}^{(l)}B_z \end{bmatrix} = {}^{\text{c}}\mathbf{M}_C({}^{(l)}\phi) \begin{bmatrix} {}^{(l)}B_x \\ {}^{(l)}B_y \\ {}^{(l)}B_z \end{bmatrix} \\
&= \begin{bmatrix} \cos({}^{(l)}\phi) & \sin({}^{(l)}\phi) & 0 \\ -\sin({}^{(l)}\phi) & \cos({}^{(l)}\phi) & 0 \\ 0 & 0 & 1 \end{bmatrix} \begin{bmatrix} {}^{(l)}B_x \\ {}^{(l)}B_y \\ {}^{(l)}B_z \end{bmatrix}
\end{aligned} \tag{27}
$$

where ${}^{\text{c}}\mathbf{M}_C$ is the transformation matrix from the Cartesian coordinate system to cylindrical coordinate system.

The magnetic field distribution of the point **P** by the l^{th} PM is presented in global Cartesian coordinate system

$$
\mathbf{B}_l = \begin{bmatrix} B_{l\rho} \\ B_{l\phi} \\ B_{lz} \end{bmatrix} = {}^{(l)}\mathbf{R}^{\text{T}(l)}\mathbf{B} = \mathbf{R}_z^{\text{T}}(\phi_l)^{(l)}\mathbf{B} = \begin{bmatrix} \cos(\phi_l) & -\sin(\phi_l) & 0 \\ \sin(\phi_l) & \cos(\phi_l) & 0 \\ 0 & 0 & 1 \end{bmatrix} \begin{bmatrix} {}^{(l)}B_\rho \\ {}^{(l)}B_\phi \\ {}^{(l)}B_z \end{bmatrix} \tag{28}
$$

Finally, the magnetic field distribution at the point **P** is obtained by all the permanent magnets in global spherical coordinate system

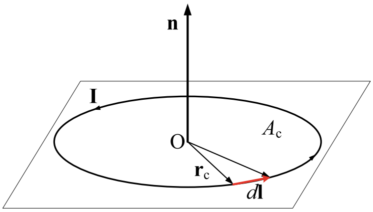

Fig. 8. Current loop for moment calculation.

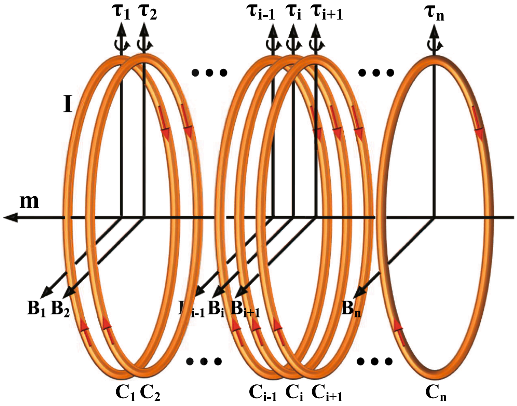

Fig. 9. Superposition of resultant torque of a solenoid.

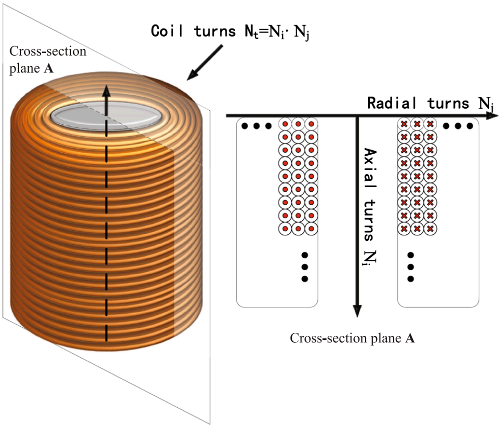

Fig. 10. Torque calculation by a single coil.

$$\mathbf{B}_\rho = \hat{\rho} \sum_{l=1}^{L} B_{l\rho} \tag{29}$$

$$\mathbf{B}_\phi = \hat{\phi} \sum_{l=1}^{L} B_{l\phi} \tag{30}$$

$$\mathbf{B}_z = \hat{z} \sum_{l=1}^{L} B_{lz} \tag{31}$$

Above all, the complete magnetic field distribution of each layer's rotor array is obtained.

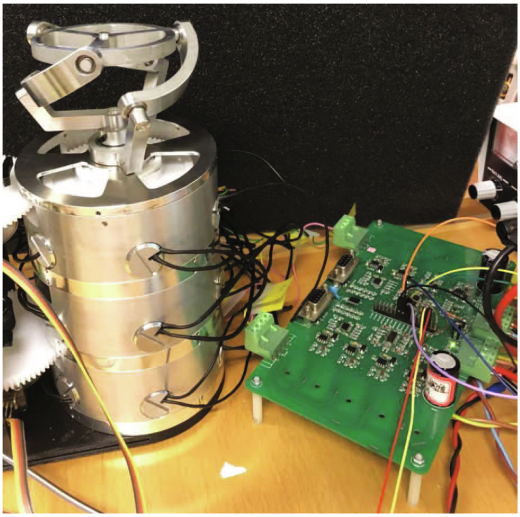

Fig. 11. A SMG prototype at AAU.

Table 1
Specifications of the SMG's electromagnetic driver.

Parameter	Value
Outer/inner stator radius	R_{os} = 45 mm, R_{is} = 28 mm
tile-shaped PM	ρ_1 = 24.5 mm, ρ_2 = 27.5 mm, Ψ = 60°
PM material	NdFe35
Number of PM poles	N_p = 12/3 layers
Subdivision number	N = 30
Outer/inner coil radius	R_{oc} = 7.5 mm, R_{ic} = 2 mm
Height of the coil	H_c = 16.5 mm
Number of coil turns	N_t = 380
Number of coils	N_c = 18/3 layers
Maximum driving current	I_m = 3 A

4. Torque modeling

The moment principle is applied to establish the torque model of spherical motion generator, which has been verified effectively in [32]. The magnetic dipole moment of a planar wire loop C with current value of I in Fig. 8, can be defined as

$$\mathbf{m} = I \oint_C \frac{1}{2} \mathbf{r}_c \times d\mathbf{l} \tag{32}$$

where $\mathbf{r}_c$ is the source point on the wire loop. It can be seen from Fig. 8 that the vector $\frac{1}{2}\mathbf{r}_c \times d\mathbf{l}$ is equal to an infinitesimal triangular area that is bounded by $\mathbf{r}_c$, $\mathbf{r}_c + d\mathbf{l}$ and $d\mathbf{l}$, with the direction perpendicular to its plane. Then the magnetic dipole moment of a wire loop is obtained

$$\mathbf{m} = IA_c\hat{\mathbf{n}} \tag{33}$$

where A_c is the area of the wire loop and $\hat{\mathbf{n}}$ is the unit vector normal to the wire plane. Considering the wire loop in an external magnetic field $\mathbf{B}$, the generated torque on account of the magnetic-dipole phenomenon can be expressed as

$$\tau = \oint_C \mathbf{r}_c \times (Id\mathbf{r}_c \times \mathbf{B}) \tag{34}$$

where $d\mathbf{r}_c$ is an infinitely small segment along the curve $\mathbf{r}_c$. If the magnetic field $\mathbf{B}$ is assumed to be constant and uniform, the torque is as follows

$$\tau = \mathbf{m} \times \mathbf{B} \tag{35}$$

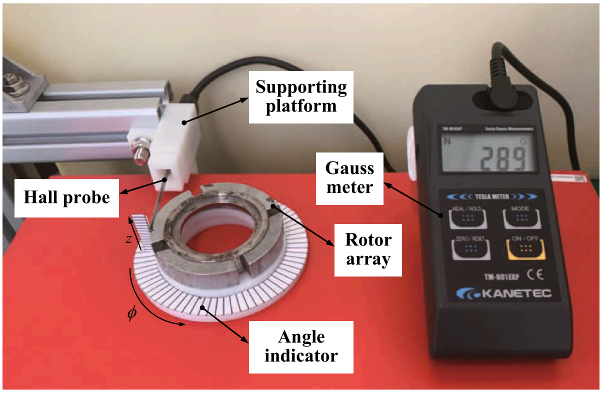

(a) Magnetic field platform

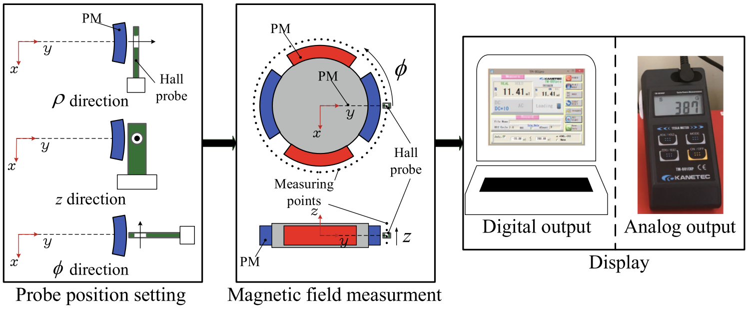

(b) Measuring scheme

Fig. 12. Magnetic field measurement.

Therefore, applying this principle to a solenoid constructed with a series of current loops, we can calculate the resultant torque by superposition of all the individual loops as shown in Fig. 9. Based on the dipole moment method and the superposition principle, the torque acting on a stator coil with N_t turn loops ($N_t = N_i{\cdot}N_j$) as shown in Fig. 10 is computed by the following:

$$\tau = \tau_{(1,1)} + \tau_{(1,2)} + \ldots + \tau_{(i,j)} = \sum_{j=1}^{N_j} \sum_{i=1}^{N_i} \tau_{(i,j)} = \sum_{j=1}^{N_j} \sum_{i=1}^{N_i} \mathbf{m}_{(i,j)} \times \mathbf{B}_{(i,j)} \tag{36}$$

Above all, the model of the torque generated by one stator coil and one-layer rotor array is obtained.

5. Model validation

In this section, FEM approach and experiments are employed to validate the analytical model of the magnetic field distribution and the torque output. The numerical model is established by using FEM software Maxwell Ansoft. A prototype of the SMG is developed as shown in Fig. 11, and the specification is presented in Table 1. The experimental platforms are designed based on the prototype.

5.1. Analytical magnetic field distribution validation

A measuring platform is built as illustrated in Fig. 12(a) to measure the air-gap magnetic field distribution of the 3D PM array. A Gauss meter (TM-801) produced by KANETEC with a measuring ragne of 0–3000 mT and a resolution of 0.01 mT is applied. A Hall probe is connected to the Gauss meter and it is fixed by a supporting platform. The rotor array is set on an angle indicator platform. The measuring scheme is designed as shown in Fig. 12(b). To measure the three components of the magnetic field, B_ρ, B_ϕ and B_z, respectively, the Hall probe is positioned at different directions. For any component of the magnetic field, the Hall probe is positioned at $\rho = 28$ mm. Then, by rotating the rotor, the probe can measure the points along the ϕ-direction of PM array in the air gap. Varying the z-directional position of the probe, a series of points that are evenly distributed on the surface outside the rotor array are measured. Finally, the value of magnetic flux density can be directly displayed on the Gauss meter panel or transmitted to the computer through USB interface.

The 3D magnetic field distribution calculated by the analytical method is compared with the numerical model and the experimental results, which are shown in Figs. 13–15. The comparison shows that the analytical results agree with the numerical and experimental results well. As shown in Fig. 13, the radial magnetic flux density B_ρ in the air gap has four peaks in accordance with the PM arrangement at the same latitude, and it achieves the peak value around the magnetization axis of the PM pole in global coordinate system. When flux density is measured at a point in the air gap along the longitudinal direction that goes through the center of PM, that is, $\phi = \frac{\pi \cdot k}{2} (k = 0, 1, 2, 3)$ with varying z, B_ϕ is equal to zero. As the measurement points get far from the PM center along the latitudinal direction, the magnitude of B_ϕ becomes larger and reaches its maximum at the edge of PM as shown in Fig. 14. Similarly, when flux density is measured in the gap at a point

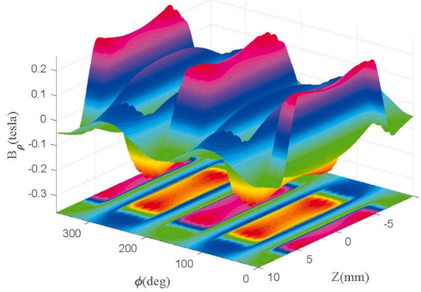

(a) Analytical results

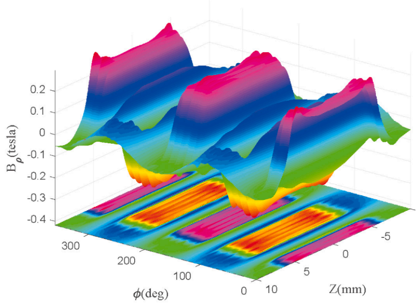

(b) Numerical results

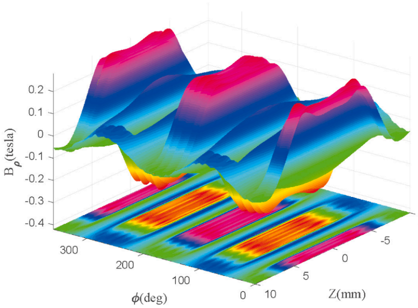

(c) Experimental results

Fig. 13. Comparison of the measured radial flux component B_ρ at $\rho = 28$ mm with results obtained from analytical method and numerical method.

along the latitudinal direction that goes through center of the PM, that is, $z = 0$ with varying ϕ, B_z is equal to zero. As the measurement points get far from the PM center, the magnitude of B_z becomes larger along the longitudinal direction, and reaches its maximum at the edge of the PM pole as shown in Fig. 15.

To evaluate the accuracy of the model, the normalized root-mean-square deviation (NRMSD) is applied, which is defined as

$$\mathrm{NRMSD} = \frac{1}{|u_{\max} - u_{\min}|}\sqrt{\frac{\sum_{j=1}^{\mathrm{N}} (u_j - v_j)^2}{\mathrm{N}}} \times 100\% \tag{37}$$

where u_j is an experimental value, $u_{\max}$ and $u_{\min}$ are the maximum and minmum of u_j, respectively, v_j is a calculated result, and N is the number of the data. The NRMSD of the three components of magnetic flux density B_ρ, B_ϕ and B_z are 3.04%, 3.43% and 3.17%, respectively. Regarding efficiency, the computing with numerical model takes more than 10 min each time, nevertheless, it only takes about 1 s to obtain results by using the analytical method. The comparisons with the numerical model and experimental data further validate the analytical magnetic model, which implies that the complete magnetic field distribution can be directly used for torque calculation.

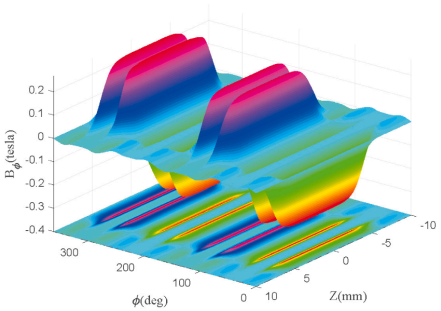

(a) Analytical results

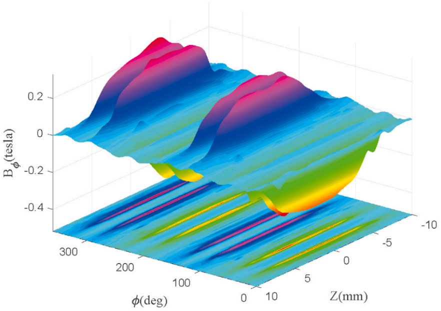

(b) Numerical results

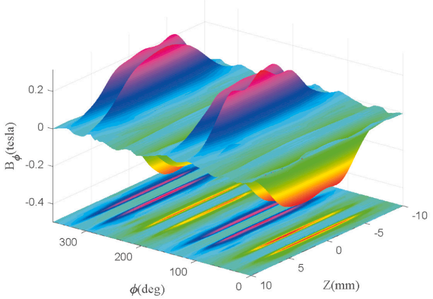

(c) Experimetal results

Fig. 14. Comparison of the measured azimuthal flux component B_ϕ at $\rho = 28$ mm with results obtained from analytical method and numerical method.

5.2. *Analytical torque model validation*

In this section, the analytical torque model is verified by numerical

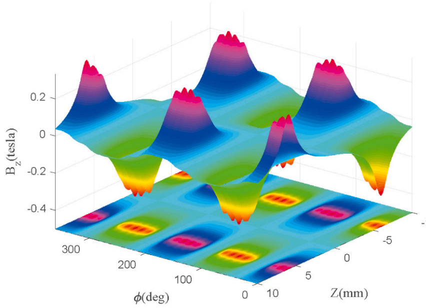

(a) Analytical results

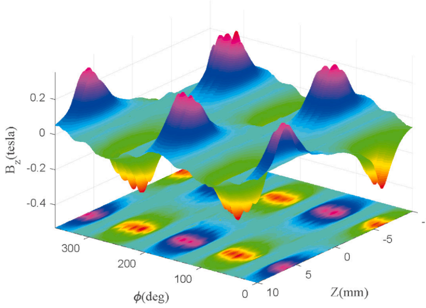

(b) Numerical results

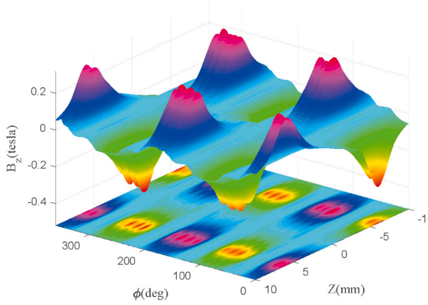

(c) Experimental results

Fig. 15. Comparison of the measured axial flux component B_z at ρ = 28 mm with results obtained from analytical method and numerical method.

FEM and the experiments. In this light, a measuring platform is constructed, as illustrated in Fig. 16(a). A miniature torque sensor FTE by Forsentek is selected with range of 0-0.1NM to conduct the experiment. The stator is installed and can rotate around a scale plate. One of the rotor array is fixed under a torque sensor. The measuring scheme is illustrated as Fig. 16(b). By rotating the stator along scale plate from P_1 to P_2 with different input currents, the torque is measured by the torque sensor. A series of experiments are designed to validate the torque model. First, the torque output is measured by only actuating Coil 1 with current value of 1 A to evaluate the analytical torque model. Then, the torque output is measured by actuating Coil 1 and 4 with input current 1 A to evaluate the superposition principle of the torque model. Finally, the torque is measured again with energizing Coil 1, 2, 4 and 5 with current 1 A simultaneously. All the values of the torque output can be displayed on the display screen.

Fig. 17 shows the torque generated by energizing Coil 1 with input current 1 A, referring to Fig. 3. All analytical, numerical and experimental results are displayed. It can be seen that the analytical torque model fits with both the numerical and the experimental results well. Fig. 18 shows the torque produced by energizing Coils 1 and 4 with input current 1 A. The results illustrate that the validity of the superposition principle of the torque model.

By energyzing Coils 1, 2, 4 and 5 with input current 1 A simultaneously, the analytical torque output is the summation of the torques generated by all the coils. The results fit well with experimental results as shown in Fig. 19.

The NRMSD values of the torques from Figs. 17–19 are 4.07%, 2.98% and 2.73%, respectively, which shows that the analytical model has a reasonable accuracy.

5.3. Result analysis

The comparisons between the I-shape and O-shape SMGs are listed in Table 2. The rotor of the O-shape SMG is the sliding unit with two tile-shape PMs. The parameters of the PM with the inner radius ρ_1 = 18 mm and the central angle Ψ = 20°. The outer radius of the PM and the parameters of the stator are the same with the parameters of the I-shape SMG.

The O-shape SMG is highly symmetrical and integrated, which is more light-weight and simple in structure and manufacturing. It is equivalent to one integrated motor which can actuate the three separate sliding units simultaneously. In comparison, the I-shape SMG is constructed by three non-identical coaxial shafts and the actuation can be considered as three monoaxial motors in three layers, which is a more complex structure. However, the I-shape SMG utilizes much less stator coils and decreases the complexity of the control system. Due to that the electromagnetic torque by the sliding unit is only generated by two PMs and their adjacent stator coils, the magnetic distribution of the sliding unit should be stronger than that of the I-shape rotor array.

To evaluate the torque output, the rotor moves by a certain angle from point T_1 to point T_2 as shown in Fig. 3. For the O-shape SMG, the torque is evaluated by the interaction between one sliding unit and one stator coil, and it reaches the maximum value 19.6211 mNM under the maximum current 3 A. For the I-shape SMG, the rotor array is mainly driven by two stator coils in the opposite position simultaneously, i.e. Coil 1 and Coil 4 in Fig. 3, and the maximum torque output is 24.6256 mNM under the current 3 A. Thus, the I-shape SMG can generate higher torque output than the O-shape one. Above all, the O-shape SMG is more suitable for the applications in flexible spherical movement and the I-shape SMG can be applied in area requiring large torque output such as vectored thrust technologies.

6. Conclusion

This paper presents an analytical model to formulate the complex 3D magnetic field distribution of the SMG in global coordinate. In this work, an integrated SMG is designed with a three-layer PM rotor array and a number of stator coils to improve the system performance. The model of magnetic field is developed analytically based on the combination of the equivalent charge model and transformation method. Firstly, the analytical model of a single PM is proposed, and then the complete analytical magnetic field model for the rotor array is formulated by superposition of all single poles with different magnetization. Upon the analytical magnetic model developed, the analytical torque model is obtained using the moment principle. Finally, both simulations and experiments are carried out to validate the analytical model.

The contribution of this paper is the experimentally validated magnetic field distribution and the torque models of the SMG. The analytical models can be used in the structure optimization and

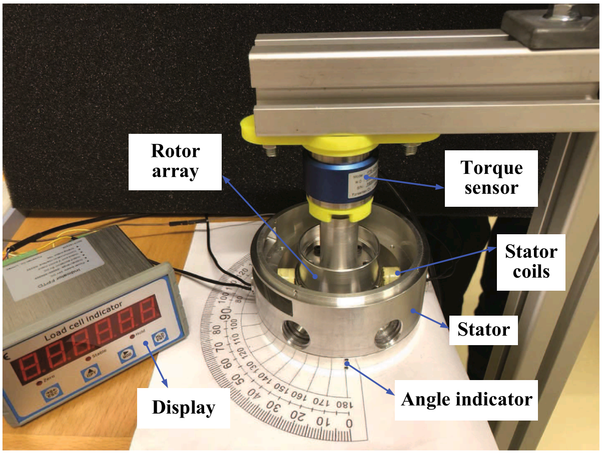

(a) Torque platform

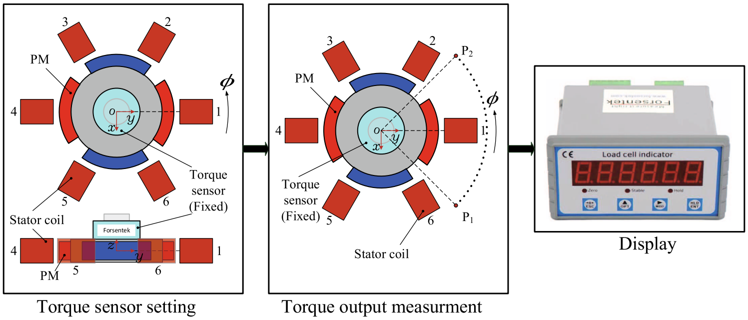

(b) Measuring scheme

Fig. 16. Torque measurement.

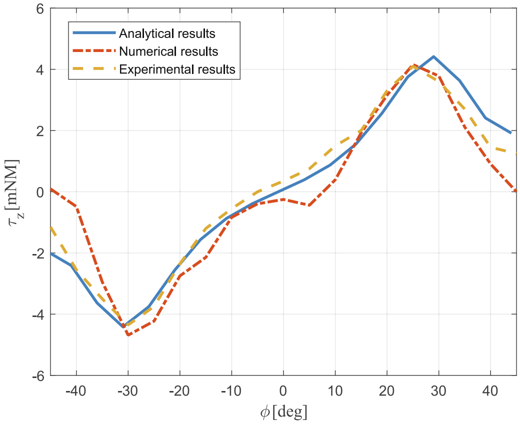

Fig. 17. Comparison of the torque generated by Coil 1 between analytical method and experimental results.

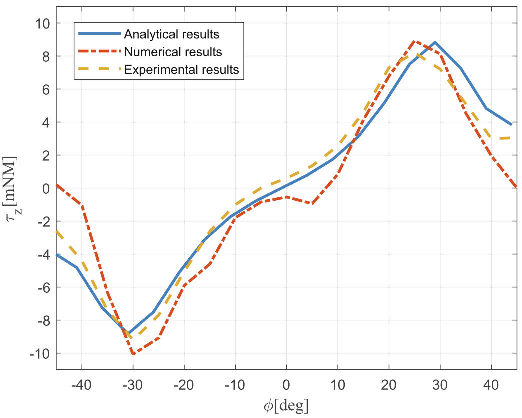

Fig. 18. Comparison of the torque generated by Coils 1 and 4 between analytical method and experimental results.

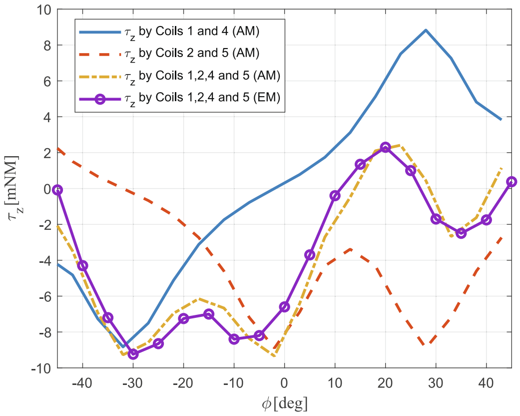

Fig. 19. Comparison of the torque generated by Coils 1, 2, 4 and 5 simultaneously between analytical method (AM) and experimental method (EM).

Table 2
Comparison between O-shape and I-shape SMGs.

Property	O-shape	I-shape
Symmetry	Highly symmetrical	Asymmetrical
Number of coils	48/2 layers	18/3 layers
Number of PM poles	6/2 layers	12/3 layers
control system	Complex	Simple
Weight of single rotor (g)	88.26	159.53
Maximum magnetic flux density (tesla)	0.4499	0.3458
Maximum torque output (mNewtonMeter)	19.6211	24.6256

employed for further study of real-time control implementation. Control strategies that combine the analytical expression will be the subject of future work.

Acknowledgments

The first author acknowledges the CSC scholarship for her study at Aalborg University, Denmark. The second and the third authors acknowledge the National Natural Science Foundation of China under Grant No. 51975029 and 51475033.

References

[1] S. Ahmadi, J.S. Moghani, M. Mirsalim, Simulation and analysis of a novel PM spherical 3-DOF actuator with E-shaped stator and blade-shaped rotor structure, Power Electronics, Drives, Systems and Technologies Conference (PEDSTC), 2018 9th Annual, IEEE, 2018, pp. 59–64, , https://doi.org/10.1109/PEDSTC.2018.8343772.

[2] D. Kang, J. Lee, Analysis of electric machine charateristics for robot eyes using analytical electromagnetic field computation method, IEEE Trans. Magn. 50 (2) (2014) 785–788, https://doi.org/10.1109/TMAG.2013.2278937.

[3] J. Enferadi, A. Shahi, On the position analysis of a new spherical parallel robot with orientation applications, Robotics Computer-Integrated Manuf. 37 (2016) 151–161, https://doi.org/10.1016/j.rcim.2015.09.004.

[4] J. Chabot, H. Schaub, Spherical magnetic dipole actuator for spacecraft attitude control, J. Guidance, Control, Dyn. (2016) 911–915, https://doi.org/10.2514/1.G001471.

[5] S. Bai, X. Li, J. Angeles, A review of spherical motion generation using either spherical parallel manipulators or spherical motors, Mech. Mach. Theory 140 (2019) 377–388, https://doi.org/10.1016/j.mechmachtheory.2019.06.012.

[6] H. Asada, J. Granito, Kinematic and static characterization of wrist joints and their optimal design, Proceedings. 1985 IEEE International Conference on Robotics and Automation, vol. 2, 1985, pp. 244–250, , https://doi.org/10.1109/ROBOT.1985.1087324.

[7] A. Chaker, A. Mlika, M. Laribi, L. Romdhane, S. Zeghloul, Accuracy analysis of non-overconstrained spherical parallel manipulators, Eur. J. Mech. A. Solids 47 (2014) 362–372, https://doi.org/10.1016/j.euromechsol.2014.06.005.

[8] H.Y. Kim, H. Kim, D. Gweon, J. Jeong, Development of a novel spherical actuator with two degrees of freedom, IEEE/ASME Trans. Mechatron. 20 (2) (2015) 532–540, https://doi.org/10.1109/TMECH.2014.2308417.

[9] C.M. Gosselin, J.-F. Hamel, The agile eye: a high-performance three-degree-of-freedom camera-orienting device, Proceedings of the 1994 IEEE International Conference on Robotics and Automation, vol 1, 1994, pp. 781–786, , https://doi.org/10.1109/ROBOT.1994.351393.

[10] G. Wu, S. Caro, S. Bai, J. Kepler, Dynamic modeling and design optimization of a 3-DOF spherical parallel manipulator, Robotics Autonomous Syst. 62 (10) (2014) 1377–1386, https://doi.org/10.1016/j.robot.2014.06.006.

[11] B. Sudki, M. Lauria, F. Noca, Marine propulsor based on a three-degree-of-freedom actuated spherical joint, Proceedings of the 3rd International Symposium on Marine Propulsors, 2013, pp. 481–485.

[12] L. Rossini, S. Mingard, A. Boletis, E. Forzani, E. Onillon, Y. Perriard, Rotor design optimization for a reaction sphere actuator, IEEE Trans. Ind. Appl. 50 (3) (2014) 1706–1716, https://doi.org/10.1109/TIA.2013.2282660.

[13] M. Strumik, R. Wawrzaszek, M. Banaszkiewicz, K. Seweryn, M. Sidz, E. Onillon, L. Rossini, Analytical model of eddy currents in a reaction sphere actuator, IEEE Trans. Magn. 50 (6) (2014) 1–7, https://doi.org/10.1109/TMAG.2014.2298215.

[14] L. Zhang, L. Yan, W. Chen, J. Liu, Current optimization of 3-DOF permanent magnet spherical motor, 6th IEEE Conference on Industrial Electronics and Applications, 2011, pp. 1111–1116, , https://doi.org/10.1109/ICIEA.2011.5975753.

[15] X. Li, J. Liu, W. Chen, S. Bai, Integrated design, modeling and analysis of a novel spherical motion generator driven by electromagnetic principle, Robotics Autonomous Syst. 106 (2018) 69–81, https://doi.org/10.1016/j.robot.2018.04.006.

[16] X. Li, S. Bai, O. Madsen, Dynamic modeling and trajectory tracking control of an electromagnetic direct driven spherical motion generator, Robotics Computer-Integrated Manuf. 59 (2019) 201–212, https://doi.org/10.1016/j.rcim.2019.04.009.

[17] K. Ma, M. Ghasemi Nejhad, Precision positioning of a parallel manipulator for spacecraft thrust vector control, J. Guidance Control Dyn. 28 (2005) 185–188, https://doi.org/10.2514/1.11112.

[18] F. Fortkamp, J. Lozano, J. Barbosa, Analytical solution of concentric two-pole halbach cylinders as a preliminary design tool for magnetic refrigeration systems, J. Magn. Magn. Mater. 444 (2017) 87–97, https://doi.org/10.1016/j.jmmm.2017.07.072.

[19] T. Taniguchi, An analytical computation of magnetic field generated from a cylinder ferromagnet, J. Magn. Magn. Mater. 452 (2018) 464–472, https://doi.org/10.1016/j.jmmm.2017.11.078.

[20] Y. Jia, Robust control with decoupling performance for steering and traction of 4ws vehicles under velocity-varying motion, IEEE Trans. Control Syst. Technol. 8 (3) (2000) 554–569, https://doi.org/10.1109/87.845885.

[21] L. Yan, I.-M. Chen, G. Yang, K.-M. Lee, Analytical and experimental investigation on the magnetic field and torque of a permanent magnet spherical actuator, IEEE/ASME Trans. Mechatron. 11 (4) (2006) 409–419, https://doi.org/10.1109/TMECH.2006.878545.

[22] C. Xia, J. Xin, H. Li, T. Shi, Design and analysis of a variable arc permanent magnet array for spherical motor, IEEE Trans. Magn. 49 (4) (2013) 1470–1478, https://doi.org/10.1109/TMAG.2012.2231092.

[23] L. Rossini, O. Chetelat, E. Onillon, Y. Perriard, Force and torque analytical models of a reaction sphere actuator based on spherical harmonic rotation and decomposition, IEEE/ASME Trans. Mechatron. 18 (3) (2013) 1006–1018, https://doi.org/10.1109/TMECH.2012.2195501.

[24] B. Li, G.D. Li, H.F. Li, Magnetic field analysis of 3-DOF permanent magnetic spherical motor using magnetic equivalent circuit method, IEEE Trans. Magn. 47 (8) (2011) 2127–2133, https://doi.org/10.1109/TMAG.2011.2123102.

[25] K.M. Lee, H. Son, Distributed multipole model for design of permanent-magnet-based actuators, IEEE Trans. Magn. 43 (10) (2007) 3904–3913, https://doi.org/10.1109/tmag.2007.904709.

[26] H. Son, K.M. Lee, Two-DOF magnetic orientation sensor using distributed multipole models for spherical wheel motor, Mechatronics 21 (1) (2011) 156–165, https://doi.org/10.1016/j.mechatronics.2010.10.001.

[27] H.Y. Kim, H.C. Kim, D.G. Gweon, Magnetic field analysis of a VCM spherical actuator, Sensors, Actuators A Phys. 195 (6) (2013) 38–49, https://doi.org/10.1016/j.sna.2013.02.024.

[28] X. Li, S. Bai, W. Chen, J. Liu, Torque modelling and current optimization of a spherical actuator built as an electro-magnets driven spherical parallel manipulator, 2017 IEEE International Conference on Cybernetics and Intelligent Systems (CIS) and IEEE Conference on Robotics, Automation and Mechatronics (RAM), 2017, pp. 626–631, , https://doi.org/10.1109/ICCIS.2017.8274850.

[29] J. Li, E.S. Barjuei, G. Ciuti, Y. Hao, P. Zhang, A. Menciassi, Q. Huang, P. Dario, Magnetically-driven medical robots: an analytical magnetic model for endoscopic capsules design, J. Magn. Magn. Mater. 452 (2018) 278–287, https://doi.org/10.1016/j.jmmm.2017.12.085.

[30] C.I. Yang, Y.S. Baek, Design and control of the 3 D.O.F. actuators by controlling the electromagnetic force, IEEE Trans. Magn. 35 (5) (1999) 3607–3609, https://doi.org/10.1109/INTMAG.1999.838034.

[31] K.M. Lee, C.K. Kwan, Design concept development of a spherical stepper for robotics applications, IEEE Trans. Robotics Autom. 7 (1) (1991) 175–181, https://doi.org/10.1109/70.68082.

[32] C.K. Lin, I.-M. Chen, L. Yan, G. Yang, Electromechanical modeling of a permanent-magnet spherical actuator based on magnetic-dipole-moment principle, IEEE Trans. Industr. Electron. 56 (5) (2009) 1640–1648, https://doi.org/10.1109/TIE.2008.2009526.

[33] S. Bai, Optimum design of spherical parallel manipulators for a prescribed workspace, Mech. Mach. Theory 45 (2) (2010) 200–211, https://doi.org/10.1016/j.mechmachtheory.2009.06.007.

Chapter 6

Conclusions

The main scope of this work is the integrated design, analytical modeling and controlling of an electromagnetic driven spherical motion generator. The new spherical motion generator is designed and constructed by combining the spherical parallel kinematic mechanism and multi-dof electromagnetic actuation in one device. To investigate the kinematic performance of the novel integrated system, kinematics and dynamics are analyzed. Analytical magnetic modeling approaches were developed for the implementation of the 3-dof electromagnetic actuation. A robust adaptive switching learning PD control algorithm is developed to achieve a high-precision trajectory tracking performance.

6.1 Summary of articles

Article I

Article I reports preliminary study of the electromagnetic driven spherical motion generator, which is equivalent to the multi-dof actuation in one unit, namely, a single-layer design. The new integrated design which is the major contribution is proposed. The new developed spherical motion generator makes the structure more light-weight and compact. The inverse kinematics and dynamics of the SMG are studied. The singularity and workspace is analyzed through the Jacobian matrix. In addition, the analytical magnetic field model and torque model are introduced, which allows us for more comprehensive design analysis and motion control development. The input currents are optimized on the basis of the energy minimization principle. A dynamic control algorithm, computed torque method, is used for the trajectory tracking in task space. A systematic simulation is designed to validate all the developed models by a co-simulation platform consisting of the analytical models implemented in Matlab/Simulink and a virtual prototype developed in ADAMS.

It can be found that the kinematic and dynamic models are verified effectively by comparing with the simulated results from the ADAMS model. The analytical magnetic field model is validated by the numerical models developed in Ansoft with acceptable error 5.62%. Compared with the permanent magnet spherical actuator, the newly designed SMG is improved with a higher torque output, which can obtain the maximum torque output 0.8 Nm with maximum current of 3 A.

Article II

Article II focused on the high-accuracy trajectory tracking control of the electromagnetic driven spherical motion generator. Based on the inverse dynamics developed in Article I, the dynamic model of the SMG is further established in task space by taking uncertainties and disturbances into considerations. To improve the position control performance, a robust adaptive switching learning PD control is proposed and demonstrated in convergence. Simulations verified that the proposed control algorithm can achieve a fast convergence with easy implementation and high precision.

The method improves the trajectory tracking performance of the spherical motion generator effectively. The simulation results show that the proposed control algorithm improves the trajectory tracking performance with the maximum position tracking error 0.0011 rad which is smaller than the maximum errors of the conventional PD and iterative learning control, 0.09 rad and 0.0072 rad, respectively.

Article III

Article III extends the work reported in Article I to analyze a different embodiment of the new spherical motion generator, namely, a multi-layer design. The multi-layer spherical motion generator is actuated by three layers' electromagnetic actuating units. Compared with the single-layer design in Article I, the multi-layer design decreases the number of stator coils which reduce the complexity of the current drive system, and the separate actuating principle simplifies the design of the controllers. For the developed SMG, an analytical model is formulated to study the magnetic field distribution of the permanent magnet rotor array based on the combination of the equivalent charge model and transformation method. Then, moment principle is applied to established the analytical torque model on the basis of the analytical magnetic field model, which greatly simplifies the calculation and improves the computing efficiency compared with analytical methods developed in Article I. Finally, the magnetic field and torque models of the spherical motion generator are verified effectively by developing corresponding experiments.

It shows from the simulation and experimental results that the analytical models can obtain reasonable accuracy. A normalized root-mean-square deviation (NRMSD) is applied to evaluate the analytical magnetic models. With the experimental data, the NRMSD values of the three components of the magnetic field distribution in cylindrical coordinate are 3.04%, 3.43% and 3.17%, respectively, which are all within 5%. The NRMSD values of the torques generated by one coil, two coils and four coils are 4.07%, 2.98% and 2.73%, respectively. Thus the analytical torque model is verified. Comparisons between the single-layer and multi-layer designs are further analyzed. The single-layer design of SMG is highly symmetric with light-weight and simple structure, which can be applied for areas with requirement of flexible spherical motion. Nevertheless, the multi-layer design is advantageous of straightforward actuating principle, which can realize 3-dof spherical motion with simple control systems. Simulations were carried out to evaluate the torque performance. With the same input current value of 3 A, the maximum torque output of the multi-layer SMG is 24.6256 mNM which is higher than that of the single-layer SMG with the value of 19.6211 mNM. By contrast, the multi-layer SMG can be used in applications that require large torque outputs.

6.2 Concluding remarks

A novel design of integrated electromagnetic driven spherical motion generator was proposed and theoretically investigated. The kinematic model of the spherical parallel manipulator with coaxial shafts is analyzed for evaluating the workspace and singularity. Analytical magnetic models including the 3D magnetic field distribution and torque modeling are formulated with reasonable accuracy, and validated by the numerical finite element methods and experiments, which are applied for actuating strategy of the spherical motion generator. A hybrid control algorithm that combines adaptive control, iterative learning control and robust control together is developed to improve the trajectory tracking performance of the spherical motion generator.

Within this PhD thesis, the following contributions are made to the development of novel electromagnetic driven spherical motion generators:

1. *Spherical motion generators integrated with multi-dof electromagnetic actuation is modeled and made into prototypes.* It is the first time that the spherical parallel manipulator and electromagnetic driven spherical actuators are integrated together in the spherical motion generator, which brings benefits of compact and light-weight structure, no backlash and rapid response.

2. *Analytical magnetic models of the spherical motion generators are formulated.*

The rotor structure of the spherical motion generator is constructed by permanent magnet arrays. Magnetic charge model is adopted to analyze the magnetic field distribution of the rotor array. A torque model is formulated using the moment principle based on the analytical results of the magnetic field in 3D coordinate system. Both models are verified by a numerical finite element software Ansoft and experiments. The analytical models are then used for the driving implementation of the spherical motion generator.

3. *A robust switching leaning PD algorithm is proposed for the trajectory tracking control.* The nonlinear dynamics of the newly designed spherical motion generator is formulated with modeling uncertainties and external disturbances. Compared with conventional PD control algorithm, the robust switching learning PD control can obtain better trajectory tracking performance, which has been validated by the co-simulation model established in Matlab/Simulink and ADAMS.

6.3 Future work

The work presented in this thesis was primarily concerned with the integrated design, analytical modeling and dynamic control of the spherical motion generator in the early stage. No consideration was given to the structure optimization, integrated control algorithm for the electromagnetic driven spherical motion generator. Whereas, they are crucial issues for its applications. Some future works are recommended:

- For the developed spherical motion generators with multi-dof actuation, the stator of actuation is constructed by numerous stator coils, which increases difficulty of current control. In order to simply the the current control system and the electric hardware design, the stator coils could be designed as the sliding units, and the permanent magnet array could be designed as the stators.

- Control algorithm depends on effective position detecting methods. High-precision and real-time position detecting systems are required.

- Analytical magnetic modeling for the spherical motion generator has been developed with reasonable accuracy. These analytical models could be further applied for the structure optimization to improve the torque output performance of spherical motion generators, and they can be combined with position control algorithms to obtain an integrated control strategy to enhance the overall performance of the system.

- Several controllers have been designed to improve the trajectory tracking performance of the spherical motion generator, and the control algorithms were validated by the co-simulation platform. Experiments could be developed to verify the algorithm based on the current prototype with multi-layer actuation.

Bibliography

[1] B. van Ninhuijs, B. L. J. Gysen, J. W. Jansen, and E. A. Lomonova, "Multi-degree-of-freedom spherical permanent magnet gravity compensator for mobile arm support systems," in *2013 International Electric Machines Drives Conference*, May 2013, pp. 1443 – 1449.

[2] T. Li and S. Payandeh, "Design of spherical parallel mechanisms for application to laparoscopic surgery," *Robotica*, vol. 20, no. 2, pp. 133 – 138, 2002.

[3] D. Kang and J. Lee, "Analysis of electric machine charateristics for robot eyes using analytical electromagnetic field computation method," *IEEE Transactions on Magnetics*, vol. 50, no. 2, pp. 785 – 788, Feb 2014.

[4] C. M. Gosselin and J. F. Hamel, "The agile eye: a high-performance three-degree-of-freedom camera-orienting device," in *Proceedings of the 1994 IEEE International Conference on Robotics and Automation*, vol. 1, May 1994, pp. 781 – 786.

[5] E. Cavallo and R. Michelini, "A robotic equipment for the guidance of a vectored thrustor auv," *35th International Symposium on Robotics (ISR 2004)*, Jan 2004.

[6] S. Bhattacharya and S. K. Agrawal, "Spherical rolling robot: a design and motion planning studies," *IEEE Transactions on Robotics and Automation*, vol. 16, no. 6, pp. 835 – 839, Dec 2000.

[7] A. Morinaga, M. Svinin, and M. Yamamoto, "A motion planning strategy for a spherical rolling robot driven by two internal rotors," *IEEE Transactions on Robotics*, vol. 30, no. 4, pp. 993 – 1002, Aug 2014.

[8] S. Bai, X. Li, and J. Angeles, "A review of spherical motion generation using either spherical parallel manipulators or spherical motors," *Mechanism and Machine Theory*, vol. 140, pp. 377 – 388, 2019.

[9] D. Ruth and J. McCarthy, "The design of spherical 4r linkages for four specified orientations," *Mechanism and Machine Theory*, vol. 34, no. 5, pp. 677 – 692, 1999.

[10] J. J. Cervantes-Sánchez, H. I. Medellín-Castillo, J. M. Rico-Martínez, and E. J. González-Galván, "Some improvements on the exact kinematic synthesis of spherical 4r function generators," *Mechanism and Machine Theory*, vol. 44, no. 1, pp. 103 – 121, 2009.

[11] B. B. Bederson, R. S. Wallace, and E. L. Schwartz, "A miniature pan-tilt actuator: the spherical pointing motor," *IEEE Transactions on Robotics and Automation*, vol. 10, no. 3, pp. 298 – 308, June 1994.

[12] S. Bai and J. Angeles, "The design of spherical multilobe-cam mechanisms," *Proceedings of the Institution of Mechanical Engineers, Part C: Journal of Mechanical Engineering Science*, vol. 223, no. 2, pp. 473 – 482, 2009.

[13] K. Gupta, "Rotatability considerations for spherical four-bar linkages with applications to robot wrist design," *Journal of Mechanisms, Transmissions, and Automation in Design*, vol. 108, no. 3, pp. 387 – 391, 1986.

[14] M. González-Palacios, C. Ortega-Alvarez, J. Sandoval-Castillo, S. Cuevas-Ledesma, and F. Mendoza-Patiño, "The generalized architecture of the spherical serial manipulator," *Advances in Robotics & Automation*, vol. 5, no. 2, pp. 1 000 148: 1 – 8, 2016.

[15] M. Sailaja, M. R. Roy, and S. P. Kumar, "Position control of stanford manipulator using artificial neural networks," *International Journal of Applied Science and Engineering Research*, vol. 4, no. 4, pp. 443 – 454, 2015.

[16] D. Stewart, "A platform with six degrees of freedom," *Proceedings of the institution of mechanical engineers*, vol. 180, no. 1, pp. 371 – 386, 1965.

[17] R. Bostelman, J. Albus, N. Dagalakis, A. Jacoff, and J. Gross, "Applications of the nist robocrane," in *Proceedings of the 5th International Symposium on Robotics and Manufacturing*, 1994, pp. 14 – 18.

[18] F. Pierrot, C. Reynaud, and A. Fournier, "Delta: a simple and efficient parallel robot," *Robotica*, vol. 8, no. 2, pp. 105 – 109, 1990.

[19] J. Madamesila, P. McGeachy, J. E. V. Barajas, and R. Khan, "Characterizing 3d printing in the fabrication of variable density phantoms for quality assurance of radiotherapy," *Physica Medica*, vol. 32, no. 1, pp. 242 – 247, 2016.

[20] G. Wu, S. Bai, J. A. Kepler, and S. Caro, "Error modeling and experimental validation of a planar 3-ppr parallel manipulator with joint clearances," *Journal of Mechanisms and Robotics*, vol. 4, no. 4, pp. 041 008: 1 – 12, 2012.

[21] M. A. Ardestani and M. Asgari, "Modeling and analysis of a novel 3-dof spatial parallel robot," in *2012 19th International Conference on Mechatronics and Machine Vision in Practice (M2VIP)*, Nov 2012, pp. 162 – 167.

[22] A. Chaker, A. Mlika, M. Laribi, L. Romdhane, and S. Zeghloul, "Accuracy analysis of non-overconstrained spherical parallel manipulators," *European Journal of Mechanics - A/Solids*, vol. 47, pp. 362 – 372, 2014.

[23] H. Asada and J. Granito, "Kinematic and static characterization of wrist joints and their optimal design," in *Proceedings of 1985 IEEE International Conference on Robotics and Automation*, vol. 2, March 1985, pp. 244 – 250.

[24] C. M. Gosselin, E. St. Pierre, and M. Gagne, "On the development of the agile eye," *IEEE Robotics Automation Magazine*, vol. 3, no. 4, pp. 29 – 37, Dec 1996.

[25] K. Al-Widyan, X. Q. Ma, and J. Angeles, "The robust design of parallel spherical robots," *Mechanism and Machine Theory*, vol. 46, no. 3, pp. 335 – 343, 2011.

[26] J. Luo, Q. M. Guo, H. Y. Li, C. J. Huang, and S. R. Xie, "Kinematic and modal simulation analysis of the bionic eye based on spherical parallel mechanism (spm)," in *Applied Mechanics and Materials*, vol. 128, 2012, pp. 1151 – 1156.

[27] B. Cui and Z. Jin, "Accuracy analysis of a novel humanoid robot shoulder joint," in *2009 ASME/IFToMM International Conference on Reconfigurable Mechanisms and Robots*, June 2009, pp. 423 – 427.

[28] S. Bai, "Optimum design of spherical parallel manipulators for a prescribed workspace," *Mechanism and Machine Theory*, vol. 45, no. 2, pp. 200 – 211, 2010.

[29] G. Wu, S. Caro, S. Bai, and J. Kepler, "Dynamic modeling and design optimization of a 3-dof spherical parallel manipulator," *Robotics and Autonomous Systems*, vol. 62, no. 10, pp. 1377 – 1386, 2014.

[30] G. Wu, "Stiffness Analysis and Optimization of a Co-axial Spherical Parallel Manipulator," *Modeling, Identification and Control*, vol. 35, no. 1, pp. 21 – 30, 2014.

[31] Q. Li, Q. Chen, C. Wu, and X. Hu, "Two novel spherical 3-dof parallel manipulators with circular prismatic pairs," in *ASME 2006 International Design Engineering Technical Conferences and Computers and Information in Engineering Conference*. American Society of Mechanical Engineers, 2006, pp. 325 – 328.

[32] B. Sudki, M. Lauria, and F. Noca, "Marine propulsor based on a three-degree-of-freedom actuated spherical joint," in *Proceedings of the 3rd International Symposium on Marine Propulsors*, May 2013, pp. 481 – 485.

[33] I. Tursynbek, "Mechanical design and kinematic analysis of a spherical parallel manipulator with coaxial input shafts," Ph.D. dissertation, Department of of Robotics and Mechatronics, School of Science and Technology, Nazarbayev University, 2017.

[34] J. Enferadi and A. Shahi, "On the position analysis of a new spherical parallel robot with orientation applications," *Robotics and Computer-Integrated Manufacturing*, vol. 37, pp. 151 – 161, 2016.

[35] F. C. Williams, E. R. Laithwaite, and J. F. Eastham, "Development and design of spherical induction motors," *Proceedings of the IEE - Part A: Power Engineering*, vol. 106, no. 30, pp. 471 – 484, December 1959.

[36] K. Davey, G. Vachtsevanos, and R. Powers, "The analysis of fields and torques in spherical induction motors," *IEEE Transactions on Magnetics*, vol. 23, no. 1, pp. 273 – 282, January 1987.

[37] L. Yan, I. Chen, C. K. Lim, G. Yang, W. Lin, and K.-M. Lee, "Design and analysis of a permanent magnet spherical actuator," *IEEE/ASME Transactions on Mechatronics*, vol. 13, no. 2, pp. 239 – 248, April 2008.

[38] D. Kang, W. Kim, S. Go, C. Jin, S. Won, D. Koo, and J. Lee, "Method of current compensation for reducing error of holding torque of permanent-magnet spherical wheel motor," *IEEE Transactions on Magnetics*, vol. 45, no. 6, pp. 2819 – 2822, June 2009.

[39] Q. Wang, Z. Li, Y. Ni, and W. Jiang, "Magnetic field computation of a pm spherical stepper motor using integral equation method," *IEEE Transactions on Magnetics*, vol. 42, no. 4, pp. 731 – 734, April 2006.

[40] A. Bhatia, M. Kumagai, and R. Hollis, "Six-stator spherical induction motor for balancing mobile robots," in *2015 IEEE International Conference on Robotics and Automation (ICRA)*, May 2015, pp. 226 – 231.

[41] G. S. Chirikjian and D. Stein, "Kinematic design and commutation of a spherical stepper motor," *IEEE/ASME Transactions on Mechatronics*, vol. 4, no. 4, pp. 342 – 353, Dec 1999.

[42] D. Stein, G. S. Chirikjian, and E. R. Scheinerman, "Theory, design, and implementation of a spherical encoder," in *Proceedings of IEEE International Conference on Robotics and Automation (ICRA)*, vol. 2, May 2001, pp. 1773 – 1779.

[43] D. Stein, E. R. Scheinerman, and G. S. Chirikjian, "Mathematical models of binary spherical-motion encoders," *IEEE/ASME transactions on mechatronics*, vol. 8, no. 2, pp. 234 – 244, 2003.

[44] J. Wang, W. Wang, G. W. Jewell, and D. Howe, "A novel spherical permanent magnet actuator with three degrees-of-freedom," *IEEE Transactions on Magnetics*, vol. 34, no. 4, pp. 2078 – 2080, July 1998.

[45] J. Wang, K. Mitchell, G. W. Jewell, and D. Howe, "Multi-degree-of-freedom spherical permanent magnet motors," in *Proceedings of IEEE International Conference on Robotics and Automation (ICRA)*, vol. 2, May 2001, pp. 1798 – 1805.

[46] W. Wang, J. Wang, G. W. Jewell, and D. Howe, "Design and control of a novel spherical permanent magnet actuator with three degrees of freedom," *IEEE/ASME Transactions on Mechatronics*, vol. 8, no. 4, pp. 457 – 468, Dec 2003.

[47] Z. Zhou and K.-M. Lee, "Real-time motion control of a multi-degree-of-freedom variable reluctance spherical motor," in *Proceedings of IEEE International Conference on Robotics and Automation (ICRA)*, vol. 3, April 1996, pp. 2859 – 2864.

[48] K.-M. Lee, R. A. Sosseh, and Z. Wei, "Effects of the torque model on the control of a vr spherical motor," *Control Engineering Practice*, vol. 12, no. 11, pp. 1437 – 1449, 2004, mechatronic Systems.

[49] K.-M. Lee, R. B. Roth, and Z. Zhou, "Dynamic modeling and control of a ball-joint-like variable-reluctance spherical motor," *Journal of dynamic systems, measurement, and control*, vol. 118, no. 1, pp. 29 – 40, 1996.

[50] H. Son and K.-M. Lee, "Open-loop controller design and dynamic characteristics of a spherical wheel motor," *IEEE Transactions on Industrial Electronics*, vol. 57, no. 10, pp. 3475 – 3482, Oct 2010.

[51] K.-M. Lee and H. Son, "Distributed multipole model for design of permanent-magnet-based actuators," *IEEE Transactions on Magnetics*, vol. 43, no. 10, pp. 3904 – 3913, Oct 2007.

[52] H. Son and K.-M. Lee, "Two-DOF magnetic orientation sensor using distributed multipole models for spherical wheel motor," *Mechatronics*, vol. 21, no. 1, pp. 156 – 165, 2011.

[53] K. Bai and K.-M. Lee, "Direct field-feedback control of a ball-joint-like permanent-magnet spherical motor," *IEEE/ASME Transactions on Mechatronics*, vol. 19, no. 3, pp. 975 – 986, June 2014.

[54] K. Bai, R. Xu, K.-M. Lee, W. Dai, and Y. Huang, "Design and development of a spherical motor for conformal printing of curved electronics," *IEEE Transactions on Industrial Electronics*, vol. 65, no. 11, pp. 9190 – 9200, Nov 2018.

[55] S. Toyama and A. Kobayashi, "Development of spherical ultrasonic motor," *CIRP Annals*, vol. 45, no. 1, pp. 27 – 30, 1996.

[56] T. Mashimo, K. Awaga, and S. Toyama, "Development of a spherical ultrasonic motor with an attitude sensing system using optical fibers," in *Proceedings of 2007 IEEE International Conference on Robotics and Automation (ICRA)*, April 2007, pp. 4466 – 4471.

[57] T. Mashimo, S. Toyama, and H. Ishida, "Design and implementation of spherical ultrasonic motor," *IEEE Transactions on Ultrasonics, Ferroelectrics, and Frequency Control*, vol. 56, no. 11, pp. 2514 – 2521, November 2009.

[58] L. Yan, F. Liang, Z. Jiao, and T. Wang, "Magnetic field analysis of novel spherical actuators with three-dimensional pole arrays," *Review of Scientific Instruments*, vol. 87, no. 6, pp. 065 006: 1 – 9, 2016.

[59] C. Xia, J. Xin, H. Li, and T. Shi, "Design and analysis of a variable arc permanent magnet array for spherical motor," *IEEE Transactions on Magnetics*, vol. 49, no. 4, pp. 1470 – 1478, April 2013.

[60] W. H. Chen, L. Zhang, F. H. Guo, and J. M. Liu, "Design and modeling of a spherical actuator with three dimensional orientation measurement system," in *Advanced Materials Research*, vol. 317. Trans Tech Publ, 2011, pp. 1088 – 1097.

[61] L. Zhang, W. Chen, J. Liu, and C. Wen, "A robust adaptive iterative learning control for trajectory tracking of permanent-magnet spherical actuator," *IEEE Transactions on Industrial Electronics*, vol. 63, no. 1, pp. 291 – 301, Jan 2016.

[62] J. Liu, H. Deng, W. Chen, and S. Bai, "Robust dynamic decoupling control for permanent magnet spherical actuators based on extended state observer," *IET Control Theory Applications*, vol. 11, no. 5, pp. 619 – 631, 2017.

[63] W. Chen, L. Zhang, L. Yan, and J. Liu, "Design and control of a three degree-of-freedom permanent magnet spherical actuator," *Sensors and Actuators A: Physical*, vol. 180, pp. 75 – 86, 2012.

[64] X. Li, J. Liu, W. Chen, and S. Bai, "Integrated design, modeling and analysis of a novel spherical motion generator driven by electromagnetic principle," *Robotics and Autonomous Systems*, vol. 106, pp. 69 – 81, 2018.

[65] R. I. Alizade, N. R. Tagiyev, and J. Duffy, "A forward and reverse displacement analysis of an in-parallel spherical manipulator," *Mechanism and Machine Theory*, vol. 29, no. 1, pp. 125 – 137, 1994.

[66] L.-W. Tsai and S. Joshi, "Kinematics and optimization of a spatial 3-upu parallel manipulator," *Journal of Mechanical Design*, vol. 122, no. 4, pp. 439 – 446, 2000.

[67] R. Di Gregorio, "The 3-rrs wrist: a new, simple and non-overconstrained spherical parallel manipulator," *Journal of Mechanical Design*, vol. 126, no. 5, pp. 850 – 855, 2004.

[68] G. Alici and B. Shirinzadeh, "Topology optimisation and singularity analysis of a 3-sps parallel manipulator with a passive constraining spherical joint," *Mechanism and Machine Theory*, vol. 39, no. 2, pp. 215 – 235, 2004.

[69] C. Gosselin and E. Lavoie, "On the kinematic design of spherical three-degree-of- freedom parallel manipulators," *The International Journal of Robotics Research*, vol. 12, pp. 394 – 402, 1993.

[70] X. Kong and C. M. Gosselin, "Type synthesis of 3t1r 4-dof parallel manipulators based on screw theory," *IEEE Transactions on Robotics and Automation*, vol. 20, no. 2, pp. 181 – 190, April 2004.

[71] C. Gosselin and J. Angeles, "The optimum kinematic design of a spherical three-degree-of-freedom parallel manipulator," *Journal of mechanisms, transmissions, and automation in design*, vol. 111, no. 2, pp. 202 – 207, 1989.

[72] S. Bai, M. R. Hansen, and J. Angeles, "A robust forward-displacement analysis of spherical parallel robots," *Mechanism and Machine Theory*, vol. 44, no. 12, pp. 2204 – 2216, 2009.

[73] S. Bai and J. Angeles, "A unified input–output analysis of four-bar linkages," *Mechanism and Machine Theory*, vol. 43, no. 2, pp. 240 – 251, 2008.

[74] R. Di Gregorio, "Kinematics of a new spherical parallel manipulator with three equal legs: The 3-urc wrist," *Journal of Robotic Systems*, vol. 18, no. 5, pp. 213 – 219, 2001.

[75] I. A. Bonev and C. M. Gosselin, "Analytical determination of the workspace of symmetrical spherical parallel mechanisms," *IEEE Transactions on Robotics*, vol. 22, no. 5, pp. 1011 – 1017, Oct 2006.

[76] O. Mahdizadeh, A. Z. Meymand, M. Mollahossein, and S. A. A. Moosavian, "Kinematics and dynamics modeling of spherical parallel manipulator," in *2018 6th RSI International Conference on Robotics and Mechatronics (IcRoM)*, Oct 2018, pp. 406 – 412.

[77] B. Dasgupta and T. Mruthyunjaya, "A newton-euler formulation for the inverse dynamics of the stewart platform manipulator," *Mechanism and Machine Theory*, vol. 33, no. 8, pp. 1135 – 1152, 1998.

[78] S. Staicu, "Recursive modelling in dynamics of agile wrist spherical parallel robot," *Robotics and Computer-Integrated Manufacturing*, vol. 25, no. 2, pp. 409 – 416, 2009.

[79] E. Abedloo, A. Molaei, and H. D. Taghirad, "Closed-form dynamic formulation of spherical parallel manipulators by gibbs-appell method," in *2014 Second RSI/ISM International Conference on Robotics and Mechatronics (ICRoM)*, Oct 2014, pp. 576 – 581.

[80] H. Elgolli, A. Houidi, A. Mlika, and L. Romdhane, "Analytical analysis of the dynamic of a spherical parallel manipulator," *The International Journal of Advanced Manufacturing Technology*, vol. 101, no. 1-4, pp. 859 – 871, 2019.

[81] L. Yan, I.-M. Chen, C. K. Lim, G. Yang, W. Lin, and K.-M. Lee, "Hybrid torque modeling of spherical actuators with cylindrical-shaped magnet poles," *Mechatronics*, vol. 21, no. 1, pp. 85 – 91, 2011.

[82] Q. Wang, Z. Qian, and G. Li, "Vision based orientation detection method and control of a spherical motor," in *2010 53rd IEEE International Midwest Symposium on Circuits and Systems*, Aug 2010, pp. 1145 – 1148.

[83] L. Yan, I.-M. Chen, G. Yang, and K.-M. Lee, "Analytical and experimental investigation on the magnetic field and torque of a permanent magnet spherical actuator," *IEEE/ASME Transactions on Mechatronics*, vol. 11, no. 4, pp. 409 – 419, Aug 2006.

[84] Z. Li, L. Zhang, W. He, Y. Zhang, and Q. Wang, "Magnetic field analysis of hybrid driven permanent magnet multi-dof motor," *2017 20th International Conference on Electrical Machines and Systems (ICEMS)*, pp. 1 – 6, 2017.

[85] B. Li, G. D. Li, and H. F. Li, "Magnetic field analysis of 3-DOF permanent magnetic spherical motor using magnetic equivalent circuit method," *IEEE Transactions on Magnetics*, vol. 47, no. 8, pp. 2127 – 2133, 2011.

[86] H. Kim, H. Kim, and D. Gweon, "Magnetic field analysis of a vcm spherical actuator," *Sensors and Actuators A: Physical*, vol. 195, pp. 38 – 49, 2013.

[87] T. Taniguchi, "An analytical computation of magnetic field generated from a cylinder ferromagnet," *Journal of Magnetism and Magnetic Materials*, vol. 452, pp. 464 – 472, 2018.

[88] A. Caciagli, R. J. Baars, A. P. Philipse, and B. W. Kuipers, "Exact expression for the magnetic field of a finite cylinder with arbitrary uniform magnetization," *Journal of Magnetism and Magnetic Materials*, vol. 456, pp. 423 – 432, 2018.

[89] Z. Qian, Q. Wang, G. Li, X. Guo, C. Hu, and H. Yan, "Design and analysis of permanent magnetic spherical motor with cylindrical poles," in *2013 International Conference on Electrical Machines and Systems (ICEMS)*, Oct 2013, pp. 644 – 649.

[90] C. I. Yang and Y. S. Baek, "Design and control of the 3 D.O.F. actuators by controlling the electromagnetic force," *IEEE Transactions on Magnetics*, vol. 35, no. 5, pp. 3607 – 3609, 1999.

[91] K.-M. Lee and C.-K. Kwan, "Design concept development of a spherical stepper for robotic applications," *IEEE Transactions on Robotics and Automation*, vol. 7, no. 1, pp. 175 – 181, Feb 1991.

[92] A. Benhama, A. C. Williamson, and A. B. J. Reece, "Virtual work approach to the computation of magnetic force distribution from finite element field solutions," *IEE Proceedings - Electric Power Applications*, vol. 147, no. 6, pp. 437 – 442, Nov 2000.

[93] A. Carpentier, N. Galopin, O. Chadebec, G. Meunier, and C. Guérin, "Application of the virtual work principle to compute magnetic forces with a volume integral method," *International Journal of Numerical Modelling: Electronic Networks, Devices and Fields*, vol. 27, no. 3, pp. 418 – 432, 2014.

[94] C. K. Lim, I. Chen, L. Yan, G. Yang, and K.-M. Lee, "Electromechanical modeling of a permanent-magnet spherical actuator based on magnetic-dipole-moment principle," *IEEE Transactions on Industrial Electronics*, vol. 56, no. 5, pp. 1640 – 1648, May 2009.

[95] C. K. Lim, I. Chen, L. Yan, G. Yang, W. Lin, and K.-M. Lee, "Torque modeling of a permanent magnet spherical actuator based on magnetic dipole moment principle," in *2008 IEEE/ASME International Conference on Advanced Intelligent Mechatronics*, July 2008, pp. 445 – 450.

[96] Q. Chen, H. Chen, Y. Wang, and P.-Y. Woo, "Global stability analysis for some trajectory-tracking control schemes of robotic manipulators," *Journal of Robotic Systems*, vol. 18, no. 2, pp. 69 – 75, 2001.

[97] X. Wang and B. Hou, "Trajectory tracking control of a 2-dof manipulator using computed torque control combined with an implicit lyapunov function method," *Journal of Mechanical Science and Technology*, vol. 32, no. 6, pp. 2803 – 2816, Jun 2018.

[98] M. I. Ullah, S. A. Ajwad, R. U. Islam, U. Iqbal, and J. Iqbal, "Modeling and computed torque control of a 6 degree of freedom robotic arm," in *2014 International Conference on Robotics and Emerging Allied Technologies in Engineering (iCREATE)*, April 2014, pp. 133 – 138.

[99] M. Asgari and M. A. Ardestani, "Dynamics and improved computed torque control of a novel medical parallel manipulator: applied to chest compressions to assist in cardiopulmonary resuscitation," *Journal of Mechanics in Medicine and Biology*, vol. 15, no. 04, pp. 1 550 051: 1 – 23, 2015.

[100] J. Alvarez-Ramirez, I. Cervantes, and R. Kelly, "PID regulation of robot manipulators: stability and performance," *Systems & Control Letters*, vol. 41, no. 2, pp. 73 – 83, 2000.

[101] Q. Li and F. Wu, "Control performance improvement of a parallel robot via the design for control approach," *Mechatronics*, vol. 14, no. 8, pp. 947 – 964, 2004.

[102] Y. Jia, "Robust control with decoupling performance for steering and traction of 4WS vehicles under velocity-varying motion," *IEEE Transactions on Control Systems Technology*, vol. 8, no. 3, pp. 554 – 569, May 2000.

[103] X. Yin and L. Pan, "Enhancing trajectory tracking accuracy for industrial robot with robust adaptive control," *Robotics and Computer-Integrated Manufacturing*, vol. 51, pp. 97 – 102, 2018.

[104] C. Xia, C. Guo, and T. Shi, "A neural-network-identifier and fuzzy-controller-based algorithm for dynamic decoupling control of permanent-magnet spherical motor," *IEEE Transactions on industrial electronics*, vol. 57, no. 8, pp. 2868 – 2878, 2010.

[105] J. Cazalilla, M. Vallés, V. Mata, M. Díaz-Rodríguez, and A. Valera, "Adaptive control of a 3-DOF parallel manipulator considering payload handling and relevant parameter models," *Robotics and Computer-Integrated Manufacturing*, vol. 30, no. 5, pp. 468 – 477, 2014.

[106] X. Wang, D. Hairong, and W. Qiong, "Research of manipulator trajectory tracking based on adaptive robust iterative learning control," *Cluster Computing*, Mar 2018.

[107] T. O. Andersen, H. C. Pedersen, and M. R. Hansen, "Discrete learning control with application to hydraulic actuators," *Modeling, Identification and Control*, vol. 36, no. 4, pp. 215 – 224, 2015.

[108] T. Ngo, M. H. Nguyen, Y. Wang, J. Ge, S. Wei, and T. L. Mai, "An adaptive iterative learning control for robot manipulator in task space," *International Journal of Computers Communications & Control*, vol. 7, no. 3, pp. 518 – 529, 2012.

[109] C.-J. Chien, "A combined adaptive law for fuzzy iterative learning control of nonlinear systems with varying control tasks," *IEEE Transactions on Fuzzy Systems*, vol. 16, no. 1, pp. 40 – 51, 2008.

[110] P. R. Ouyang, W. J. Zhang, and M. M. Gupta, "An adaptive switching learning control method for trajectory tracking of robot manipulators," *Mechatronics*, vol. 16, no. 1, pp. 51 – 61, 2006.

[111] P. Flores, "Euler angles, bryant angles and euler parameters," in *Concepts and Formulations for Spatial Multibody Dynamics*. Springer, 2015, pp. 15 – 22.

[112] J. G. De Jalon and E. Bayo, *Kinematic and dynamic simulation of multibody systems: the real-time challenge*. Springer Science & Business Media, 2012.

[113] C. Gosselin, J. Sefrioui, and M. J. Richard, "On the direct kinematics of spherical three-degree-of-freedom parallel manipulators of general architecture," *Journal of Mechanical Design*, vol. 116, no. 2, pp. 594 – 598, 1994.

[114] R. T. Rockafellar, "Lagrange multipliers and optimality," *SIAM review*, vol. 35, no. 2, pp. 183 – 238, 1993.

[115] J. C. Maxwell, *A dynamical theory of the electromagnetic field*. The Society, 1856.

[116] B. S. Guru and H. R. Hiziroglu, *Electromagnetic field theory fundamentals*. Cambridge university press, 2009.

[117] E. P. Furlani, *Permanent magnet and electromechanical devices: materials, analysis, and applications*. Academic press, 2001.

[118] J. Liu, X. Li, W. Chen, L. Liu, and S. Bai, "Magnetic field modeling and validation for a spherical actuator with cylindrical permanent magnets," *Simulation Modelling Practice and Theory*, vol. 98, pp. 101 954: 1 – 18, 2020.

[119] X. Li, J. Liu, W. Chen, and S. Bai, "Analytical magnetics and torque modeling of a multi-layer electromagnetic driven spherical motion generator," *Journal of Magnetism and Magnetic Materials*, vol. 493, pp. 165 707: 1 – 11, 2020.

ISSN (online): 2446-1636
ISBN (online): 978-87-7210-499-7

AALBORG UNIVERSITY PRESS